Neutral Kaon Production from One-prong Tau Decays

by

Ian Timothy Lawson

B.Sc., University of New Brunswick, 1993
M.Sc., University of Victoria, 1996

A Dissertation Submitted in Partial Fulfillment of the
Requirements for the Degree of

DOCTOR OF PHILOSOPHY

in the Department of Physics and Astronomy.

We accept this dissertation as conforming
to the required standard.

Dr. R. Sobie, Co-supervisor (Department of Physics and Astronomy)

Dr. R.K. Keeler, Co-supervisor (Department of Physics and Astronomy)

Dr. G. Beer, Departmental Member (Department of Physics and Astronomy)

Dr. P. Wan, Outside Member (Department of Chemistry)

Dr. C.J. Oram, External Examiner (TRIUMF Laboratory)

Supervisors: Dr. R. Sobie and Dr. R.K. Keeler

ABSTRACT

The branching ratio for the decay of the tau lepton into at least one neutral kaon meson was measured from a sample of 201850 tau decays recorded by the OPAL detector from 1991 to 1995. The selection yielded 305 $\tau^- \rightarrow X^- \mathrm{K}^0_\mathrm{L} \nu_\tau$ candidates (the charge conjugate is implied for all reactions), where X^- is any charged hadron possibly accompanied by a neutral particle, giving a branching ratio of

$$B(\tau^- \rightarrow X^- \mathrm{K}^0_\mathrm{L} \nu_\tau) = (10.01 \pm 0.79 \pm 0.64) \times 10^{-3},$$

where the first error is statistical and the second is systematic. From the sample of $\tau^- \rightarrow X^- \mathrm{K}^0_\mathrm{L} \nu_\tau$ decays, three exclusive decay modes were identified and their branching ratios were measured to be

$$\begin{aligned} B(\tau^- \rightarrow \pi^- \overline{\mathrm{K}}^0 \nu_\tau) &= (9.1 \pm 0.9 \pm 0.6) \times 10^{-3}, \\ B(\tau^- \rightarrow \pi^- \overline{\mathrm{K}}^0 \geq 1\pi^0 \nu_\tau) &= (3.6 \pm 1.3 \pm 1.0) \times 10^{-3}, \\ B(\tau^- \rightarrow \mathrm{K}^- \mathrm{K}^0 \geq 0\pi^0 \nu_\tau) &= (3.3 \pm 0.9 \pm 0.7) \times 10^{-3}, \end{aligned}$$

where the first error is statistical and the second is systematic. The $\tau^- \rightarrow \mathrm{K}^*(892)^- \nu_\tau$ branching ratio was determined to be 0.0140 ± 0.0013 using the $\tau^- \rightarrow \pi^- \overline{\mathrm{K}}^0 \nu_\tau$ branching ratio and assuming isospin conservation. Finally, the ratio of the non-strange decay constant f_ρ to the strange decay constant f_{K^*} was measured to be 0.93 ± 0.05.

Examiners:

Dr. R. Sobie, Co-supervisor (Department of Physics and Astronomy)

Dr. R.K. Keeler, Co-supervisor (Department of Physics and Astronomy)

Dr. G. Beer, Departmental Member (Department of Physics and Astronomy)

Dr. P. Wan, Outside Member (Department of Chemistry)

Dr. C.J. Oram, External Examiner (TRIUMF Laboratory)

Contents

List of Tables

List of Figures

Chapter 1

Introduction

This dissertation presents the first measurement of the branching ratio of the decay of the tau (τ) lepton into a final state containing at least one K^0_L meson by the OPAL[1] collaboration. The analysis was done using data collected between 1991 and 1995 using the OPAL detector, a multipurpose experiment located at the LEP[2] collider at the European Centre for Particle Physics Research (CERN) located near Geneva, Switzerland.

The field of particle physics began just over one hundred years ago with the discovery of the electron in 1897 by Thomson. Advancements in accelerator and detector technology have rapidly occurred leading to the discoveries of new particles and a better understanding of particles and their interactions. In 1975, the third generation τ lepton was discovered by M. Perl *et al.* [1] at the SPEAR $\mathrm{e}^+\mathrm{e}^-$ storage ring. Subsequently, the τ itself became the subject of intense investigation as one can use τ production and decays to explore several features of particle physics, including the electromagnetic, weak and strong forces. One can test the validity of the many features of the Standard Model of particle physics [2] and search for new physics beyond the Standard Model.

---

[1] Omni-Purpose Apparatus for LEP

[2] Large Electron Positron

The τ is a sequential third generation charged lepton. Specifically, this means that the τ is a point-like spin 1/2 particle with properties and couplings which are believed to be identical, except in mass, to those of the electron and muon. The mass of the τ, 1777.1 MeV[3] [3, p. 286], is more than three thousand times greater than the electron ($m_{\mathrm{e}} = 0.511$ MeV). The τ decays via the charged weak interaction with a lifetime of 290.0 fs [3, p. 286]. The sample of τ lepton pairs used in this analysis was created through electron-positron collisions ($\mathrm{e}^+\mathrm{e}^- \rightarrow \tau^+\tau^-$) close to a centre-of-mass energy of 91.2 GeV, the mass of the Z^0 boson.

The large mass of the τ allows it to decay into both leptonic and hadronic final states. Leptonic tau decays have final states containing either an electron (e) and an electron neutrino (ν_{e}) or a muon (μ) and a muon neutrino (ν_μ) accompanied by a τ neutrino (ν_τ) (see Figure 1.1(a)). Hadronic τ decays are assumed to have final states consisting of a single charged meson, h^- (a quark-antiquark or $\mathrm{q}\overline{\mathrm{q}}$ pair) accompanied by a ν_τ (see Figure 1.1(b)). Final states with two or more mesons are assumed to be the result of the decay of an initial heavier meson. The charged meson pairs are composed of up (u) and down (d) type quarks such as $\pi^-(\mathrm{u}_\uparrow\overline{\mathrm{d}}_\downarrow)$ and $\rho(770)^-(\mathrm{u}_\uparrow\overline{\mathrm{d}}_\uparrow)$, where the arrow represents the spin of the quark. Although these two mesons have the same quark content they have different masses due to their different spin configurations. The spins of the two quarks in the π^- are antiparallel giving total spin zero. The spins of the two quarks forming the $\rho(770)^-$ are parallel giving total spin one. Table 1.1 shows several mesons described in this work; their quark content and spin alignment are shown. Note that the spins of each pair of quarks may be reversed since the magnitude of the total spin remains the same. For completeness, the orbital angular momentum, the total angular momentum and the parity of each meson is shown in the table.

---

[3] Natural units ($\hbar = c = 1$) are used throughout this work unless otherwise specified.

Net Spin	Orbital ang. mom.	J^P	Strangeness = 0		Strangeness = −1	
			Quark Content & Spin	Observed Meson	Quark Content & Spin	Observed Meson
$s = 0$	$l = 0$	0^-	$\mathrm{u}_\uparrow\overline{\mathrm{d}}_\downarrow$	$\pi(140)^-$	$\mathrm{u}_\uparrow\overline{\mathrm{s}}_\downarrow$	$\mathrm{K}(494)^-$
	$l = 0$	0^-	$\left(\mathrm{u}_\uparrow\overline{\mathrm{u}}_\downarrow - \mathrm{d}_\uparrow\overline{\mathrm{d}}_\downarrow\right)/\sqrt{2}$	$\pi(135)^0$	$\mathrm{d}_\uparrow\overline{\mathrm{s}}_\downarrow$	$\mathrm{K}(498)^0$
$s = 1$	$l = 0$	1^-	$\mathrm{u}_\uparrow\overline{\mathrm{d}}_\uparrow$	$\rho(770)^-$	$\mathrm{u}_\uparrow\overline{\mathrm{s}}_\uparrow$	$\mathrm{K}^*(892)^-$
	$l = 1$	1^+	$\mathrm{u}_\uparrow\overline{\mathrm{d}}_\uparrow$	$\mathrm{a}_1(1260)^-$	$\mathrm{u}_\uparrow\overline{\mathrm{s}}_\uparrow$	$\mathrm{K}_1(1400)^-$

Table 1.1: The quark content and spin is shown for several different mesons. The mesons are grouped into non-strange (Strangeness = 0) and strange (Strangeness = −1) mesons. The net spin (s), orbital angular momentum (l), total angular momentum (J) and the parity (P) of the $\mathrm{q}\overline{\mathrm{q}}$ pairs are shown. The mass of each meson is shown in the parentheses in units of MeV followed by a superscript indicating the electric charge.

In the hadronic τ decay shown in Figure 1.1(b), the W^- can only decay into a $\mathrm{u}\overline{\mathrm{d}}'$ state due to energy conservation, where the u-quark and d′-quark are the weak quark eigenstates [4]. In 1963, Cabibbo proposed an hypothesis exclusive to the quark sector which states that weak quark eigenstates may be mixtures of the quark mass eigenstates [5]. This phenomenon as defined affects only the d′-type quarks, such that the weak d′-quark eigenstate is an admixture of the d-quark and the s-quark mass eigenstates, whereas the weak u-quark eigenstate is equal to the u-quark mass eigenstate. The definition is purely conventional and one could accomplish the same purpose by introducing a u′-type quark eigenstate in lieu of the d′-type quark eigenstate. This phenomenon allows for additional possible final state mesons containing $\mathrm{u}\overline{\mathrm{s}}$ quarks for τ decays. The s quark mesons analogous to the π^- and $\rho(770)^-$ mesons are the $\mathrm{K}^-(\mathrm{u}_\uparrow\overline{\mathrm{s}}_\downarrow)$ and $\mathrm{K}^*(892)^-(\mathrm{u}_\uparrow\overline{\mathrm{s}}_\uparrow)$. These *strange* mesons have similar properties, except for mass, as the non-strange mesons. Due to the amount of quark mixing, strange mesons are produced at a much lower rate than non-strange mesons. For example, the branching ratio of the $\tau^- \to \pi^-\nu_\tau$ decay is $(11.08 \pm 0.13)\%$ while the branching ratio of the $\tau^- \to \mathrm{K}^-\nu_\tau$ decay is only $(0.71 \pm 0.05)\%$ [3, p. 286].

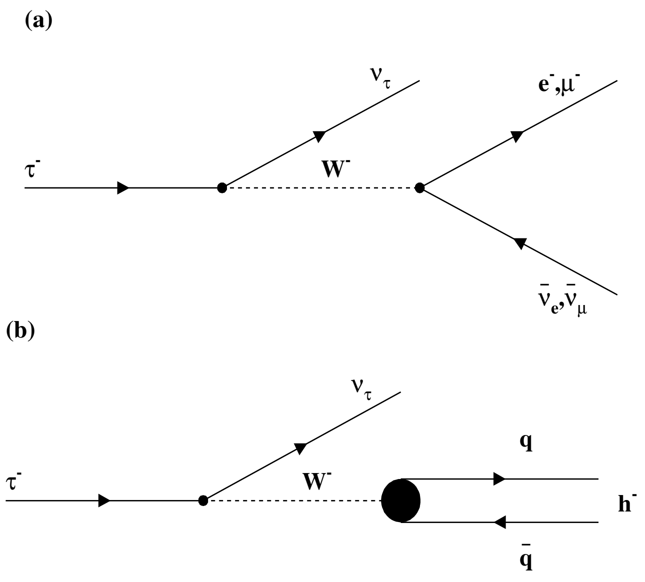

Figure 1.1: Feynman diagrams of the τ decay. (a) shows the τ leptonic decays and (b) shows the τ hadronic decays, where the blob at the vertex indicates the unknown hadronic interactions that yield a meson h^-.

Many of the current studies of τ decays concentrate on understanding the τ lepton's dominant decay modes in which the final state contains leptons or non-strange mesons. These final decay states account for approximately 97% of the τ decay products. Most of the remaining suppressed decays include kaons, i.e., mesons that contain one strange quark. Consequently, their decay fractions are small and the decays are more difficult to identify than the leptonic or pionic decay modes. Therefore the first step in understanding more about the τ decays into strange mesons is to identify them and then to measure their branching ratios.

The decay of the τ^- into a $\mathrm{u}\overline{\mathrm{s}}$ pair can result in a K^- or an excited K meson in the final state. The excited K mesons then usually decay into final states involving K^- and also $\overline{\mathrm{K}}^0$ mesons (or K^+ and K^0 for τ^+ decays) because hadronic decays preserve the quark flavours. The two neutral kaons, K^0 and $\overline{\mathrm{K}}^0$, are not directly observed in nature, instead one observes the physical particles known as $\mathrm{K^0_S}$ and $\mathrm{K^0_L}$.[4] The mass eigenstates of these physical particles are admixtures of the $\mathrm{K^0}$ and $\mathrm{\overline{K}^0}$ eigenstates,

$$|\mathrm{K^0_S}\rangle = \frac{(1+\epsilon)|\mathrm{K^0}\rangle + (1-\epsilon)|\mathrm{\overline{K}^0}\rangle}{\sqrt{2\,(1+\epsilon^2)}} \tag{1.1}$$

$$|\mathrm{K^0_L}\rangle = \frac{(1+\epsilon)|\mathrm{K^0}\rangle - (1-\epsilon)|\mathrm{\overline{K}^0}\rangle}{\sqrt{2\,(1+\epsilon^2)}}, \tag{1.2}$$

where $\epsilon \simeq 2.3 \times 10^{-3}$ [3, p. 107]. The mass eigenstates would be exact even and odd eigenstates of the CP operator[5] except for the very small CP violation introduced by ϵ. The CP even state, the $\mathrm{K^0_S}$, decays into two pions, a combination which is also CP even, whereas the CP odd state, the $\mathrm{K^0_L}$, decays into a CP odd combination of three pions. Consequently, any given sample of $\mathrm{K^0}$ or $\mathrm{\overline{K}^0}$ mesons is composed of approximately 50% $\mathrm{K^0_L}$ and 50% $\mathrm{K^0_S}$ mesons.

The discovery of the first type of neutral kaon took place in 1947 by Rochester and Butler [6] as it decayed into two pions. The second type of neutral kaon was discovered in 1956 by Lederman *et al.* [7] at Brookhaven as it decayed into three pions. The charged kaon, $\mathrm{K^-}$, was discovered by Powell *et al.* [8] in 1949 as it decayed into a muon antimuon neutrino pair. It has been observed that the $\mathrm{K^0_S}$ decay into two pions is much faster than the $\mathrm{K^0_L}$ decay into three pions due to phase space limitations. The experimental lifetimes of the kaons are [3, p. 439]:

$$\begin{aligned} T_{\mathrm{K^0_S}} &= 8.9 \times 10^{-11}\ \mathrm{s} \\ T_{\mathrm{K^0_L}} &= 5.2 \times 10^{-8}\ \mathrm{s} \\ T_{\mathrm{K^\pm}} &= 1.2 \times 10^{-8}\ \mathrm{s}. \end{aligned}$$

---

[4] The S and L subscripts delineate short and long, referring to the short and long decay lengths of the two particles, respectively.

[5] The CP operator is a space reflection through the origin followed by a charge conjugation, changing the sign of all the quantum numbers.

Thus a relativistic $\mathrm{K_S^0}$ meson will travel only a few centimeters while the $\mathrm{K_L^0}$ meson can travel many meters. For example, if the kaon had an energy of 10 GeV, then the $\mathrm{K_S^0}$ meson would travel on average 55 cm before decaying into two pions while the $\mathrm{K_L^0}$ meson would travel on average 325 m and the $\mathrm{K^\pm}$ mesons would travel on average 75 m before decaying.

In the detectors currently used to study τ decays, various methods have been devised to identify the strange decay modes. Charged kaons have been identified through measurements of their energy loss as they traverse a gas. The different lifetimes of the neutral kaons allows one to distinguish a $\mathrm{K_S^0}$ from a $\mathrm{K_L^0}$ using their decay lengths. Consequently, the short-lived $\mathrm{K_S^0}$ mesons have been studied by searching for evidence of the $\mathrm{K_S^0}$ decaying into a $\pi^-\pi^+$ final state that is visible in a tracking chamber, while long-lived $\mathrm{K_L^0}$ mesons have been identified through their interactions with electromagnetic and hadronic calorimeters that contain the $\mathrm{K_L^0}$ meson's energy.

Using the latter method, this analysis looked for decays containing a charged track and at least one $\mathrm{K_L^0}$ meson. Using τ decays that have this topology, the $\tau^- \to X^-\mathrm{K_L^0}\nu_\tau$ branching ratio[6] is measured where X^- is either a π^- or a $\mathrm{K^-}$ which may be accompanied by any number of neutral particles. This is the first OPAL analysis to identify a $\mathrm{K_L^0}$ meson. The $\tau^- \to X^-\mathrm{K_L^0}\nu_\tau$ decays are then examined to determine the identity of the X^-. The charged hadron is identified using the energy loss of the particle as it passes through the OPAL jet chamber and π^0 mesons are identified primarily by observing an excess of energy in the electromagnetic calorimeter. Following these additional selections, the branching ratios of three exclusive decay modes are measured: $\tau^- \to \pi^-\overline{\mathrm{K}}^0\nu_\tau$, $\tau^- \to \pi^-\overline{\mathrm{K}}^0 \geq 1\pi^0\nu_\tau$ and $\tau^- \to \mathrm{K^-K^0} \geq 0\pi^0\nu_\tau$. These decay modes

---

[6] Charge conjugation is assumed throughout this work. When quoted decay modes list only the negative charged state, the corresponding positive charge state is implied.

include both $\mathrm{K_L^0}$ and $\mathrm{K_S^0}$ mesons, by convention they are collectively labelled as $\mathrm{K^0}$ (or $\overline{\mathrm{K}}^0$). These branching ratio results will be shown to be in very good agreement with recent results from the ALEPH and L3 collaborations in which the τ decays into a final state containing a $\mathrm{K_L^0}$ meson. In addition, the new measurements presented here are compared to results from the CLEO and ALEPH collaborations in which the final state contains a $\mathrm{K_S^0}$ meson. The corresponding branching ratios are expected to be equal, as previously discussed.

As described above, the τ^- can decay into a $\mathrm{u\overline{s}}$ pair giving a $\mathrm{K^-}$ final state or an excited K meson final state, such as the $\mathrm{K^*(892)^-}$ or $\mathrm{K_1(1400)^-}$ mesons. The excited K mesons decay very rapidly through the strong interaction with lifetimes of order 10^{-23} s. The lowest mass K meson, aside from the $\mathrm{K^-}$, is the $\mathrm{K^*(892)^-}$. It is a vector ($J = 1$) meson and decays into a $(\pi\overline{\mathrm{K}})^-$ final state (either $\pi^-\overline{\mathrm{K}}^0$ or $\mathrm{K^-}\pi^0$). Therefore, one can use the branching ratio of the $\tau^- \to \pi^-\overline{\mathrm{K}}^0\nu_\tau$ decay mode and isospin conservation of the $\mathrm{K^*(892)^-}$ meson with respect to its decay products to make a measurement on the branching ratio of the $\tau^- \to \mathrm{K^*(892)^-}\nu_\tau$ decay mode. The concept of isospin conservation will be discussed further in Chapter 2. This branching ratio can then be compared to various theoretical predictions and other experimental results, including the analogous OPAL result using the $\pi^-\mathrm{K_S^0}$ final state. More information on the various possible resonances of the three exclusive decay modes will be discussed in Chapters 2 and 4.

In addition, existing experiments have not observed individual quarks. Currently, physicists only have observed the final state hadron and not the processes that occur in its creation. Consequently, one does not know how the charged weak current couples the quarks to form hadrons. Figure 1.2 uses a blob at the vertex to show this unknown coupling for the $\tau^- \to \mathrm{K^*(892)^-}\nu_\tau$ decay; the unknown coupling strength is denoted

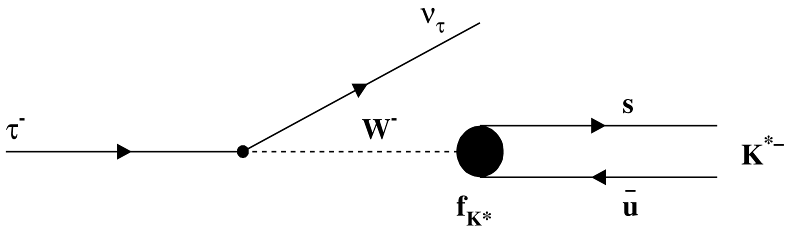

Figure 1.2: A Feynman diagram of the $\tau^- \rightarrow \mathrm{K}^*(892)^- \nu_\tau$ decay.

by the form factor (decay constant) f_{K^*}. A measurement of the $\tau^- \rightarrow \mathrm{K}^*(892)^- \nu_\tau$ branching ratio can be used to calculate f_{K^*}.

A more detailed description of the Standard Model is presented in Chapter 2; this chapter will also describe the properties of the τ and give a description on how the decay rates of tau hadronic decays can be predicted. Chapter 3 gives a description of the LEP collider and the OPAL detector data processing scheme and its subdetectors. Chapter 4 presents a detailed description of the interaction of particles with matter. Chapter 5 describes the selection of the sample of τ leptons used in this work created through electron-positron collisions close to the centre-of-mass energy of 91.2 GeV, the mass of the Z^0 boson. Chapter 5 also gives a description of the simulated events that were used to describe the data. Chapter 6 describes the selection of the $\tau^- \rightarrow X^- \mathrm{K}^0_{\mathrm{L}} \nu_\tau$ decays and determines the composition of X^-. Chapter 7 presents the branching ratio results and the systematic errors are described. In Chapter 8, the branching ratios are compared to other experimental results and theoretical predictions. Finally, Chapter 9 summarises the results and presents the conclusions.

Chapter 2

Theory

This chapter will describe the Standard Model and the physics of tau hadronic decays. The first section will give a brief review of the Standard Model. The second section will describe how quark mixing occurs within the Standard Model. The third section will outline the concept of isospin conservation. Finally, the fourth section will discuss tau hadronic decays with an emphasis on the neutral kaon decays that are being studied in this dissertation.

2.1 Standard Model

The Standard Model [2] is a highly successful description of the interactions of elementary particles. In this theory, matter is composed of point-like spin 1/2 fermions, which interact via the strong, weak and electromagnetic forces through the exchange of gauge bosons. Some properties of these gauge bosons and fermions are shown in Table 2.1 [3, p. 223–348].

Fermions can be categorised as either leptons or quarks. Leptons consist of three charged particles: the electron (e), muon (μ) and tau (τ); and three neutral particles: the electron neutrino (ν_e), muon neutrino (ν_μ) and tau neutrino (ν_τ). These particles possess integer electric charge (0 or -1) and do not interact with the strong force. There are six quarks (u,d,c,s,t and b) which have a fractional electric charge and interact via the strong force as well as the weak and electromagnetic forces. For *everyday* matter, essentially all physics can be described using only four fermions: two leptons (ν_{e} and e) and two quarks (u and d). These fermions are grouped together to form the first generation of matter. Each fermion is also associated to an antiparticle with opposite electric charge and opposite quantum numbers.

The remaining, more exotic, fundamental particles are grouped into two additional families which are identical to the first generation in all respects except for their masses. The three rows in the top part of Table 2.1 correspond to the three families. Each family consists of a charged lepton and a neutrino as well as a pair of quarks with charges +2/3 and -1/3. The weak force is able to couple members of each weak isospin doublet to one another by charged current interactions.

The gauge bosons mediating the strong, weak and electromagnetic forces arise due to the invariance of the Standard Model Lagrangian under a $SU(3)_c \times SU(2)_L \times U(1)_Y$ local gauge transformation.[1] The $SU(3)_c$ group determines the couplings between strongly interacting particles by the exchange of colour carrying gauge bosons called gluons. The $SU(2)_L \times U(1)_Y$ gauge group describes the unified electroweak interaction described by Glashow, Salam and Weinberg [2]. The subscript L on $SU(2)_L$ is due to the experimental observation that the charged currents in weak interactions couple only to the left-handed chiral states of particles forming doublets of weak isospin [4]. Right-handed particles are classified as singlets. As a consequence, leptons remain unmixed within the minimal Standard Model. The final group, $U(1)_Y$, relates the weak hypercharge Y to the electric field Q and the third component of the weak isospin T_3 by $Q = T_3 + Y/2$.

---

[1] The term *gauge transformation* denotes a transformation of a physical system that obeys the symmetry of the mathematical group and leaves the physical state of the system unchanged.

Fermions (spin = 1/2)

Leptons				Quarks			
Name	Mass (GeV)	Charge (Q)	Isospin (T_3)	Name	Mass (GeV)	Charge (Q)	Isospin (T_3)
ν_e	$< 5.1 \times 10^{-9}$	0	+1/2	u	0.0033 ± 0.0018	+2/3	+1/2
e	5.1×10^{-4}	−1	−1/2	d	0.0060 ± 0.0030	−1/3	−1/2
ν_μ	$< 2.7 \times 10^{-4}$	0	+1/2	c	1.250 ± 0.150	+2/3	+1/2
μ	0.106	−1	−1/2	s	0.115 ± 0.055	−1/3	−1/2
ν_τ	< 0.031	0	+1/2	t	173.8 ± 5.2	+2/3	+1/2
τ	1.777	−1	−1/2	b	4.3 ± 0.2	−1/3	−1/2

Gauge Bosons (spin = 1)

Name	Mass (GeV)	Charge
photon (γ)	0	0
W^-	80.22	−1
W^+	80.22	+1
Z^0	91.19	0
gluon (g)	0	0

Table 2.1: Boson and fermion properties. The mass, charge and weak isospin are shown for each fermion while the mass and charge are shown for each boson. The particle masses are taken from reference [3, p. 223–348].

The masses of the gauge bosons and fermions are the result of couplings between the gauge or fermion fields and a scalar field called a Higgs field. The Higgs interaction is one way to generate particle masses in a gauge invariant, Lorentz invariant and renormalisable way. The Higgs field spontaneously breaks the local $SU(2)_L \times U(1)_Y$ gauge symmetry to produce the separate electromagnetic and weak forces. The resulting massive gauge bosons, $W^\pm$ and Z^0, are associated with the weak interaction. However the photon (γ), which is associated with the residual remaining unbroken $U(1)_Q$ symmetry, remains massless. The gauge bosons and their properties are given in Table 2.1. Feynman diagrams for the electromagnetic, strong, charged and neutral

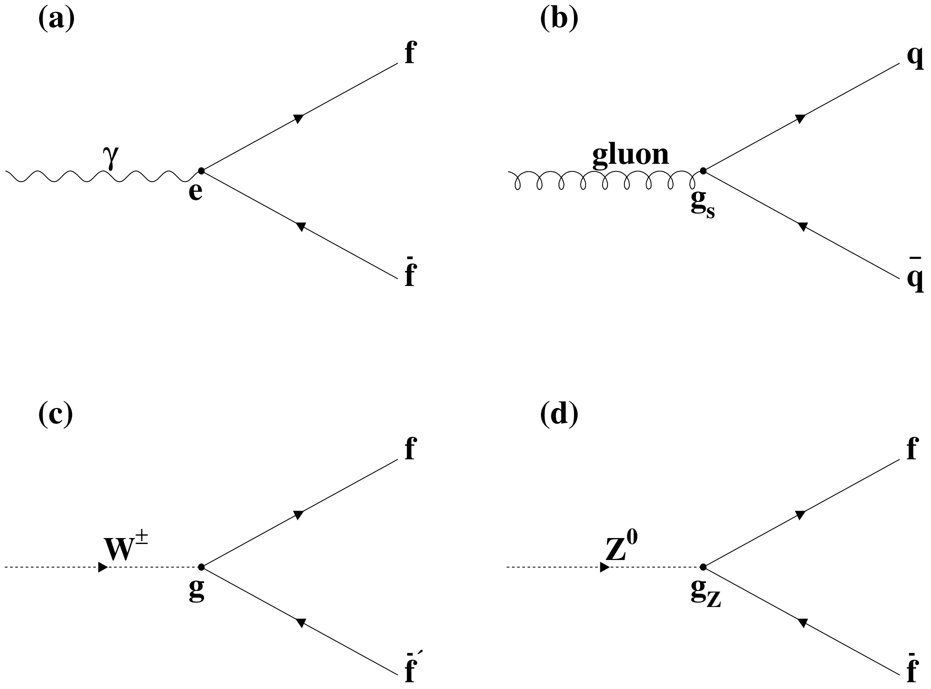

Figure 2.1: The couplings of the electromagnetic, strong, charged and neutral weak interactions that are permitted in the Standard Model: (a) the coupling of a photon (γ) to a fermion (f) with the coupling constant e giving the electromagnetic force; (b) the coupling of a gluon to a quark (q) giving the strong force; (c) the weak charge current coupling of a $\mathrm{W}^\pm$ to fermions of a weak isospin doublet and (d) the weak neutral current coupling of a fermion (f) to a Z^0.

weak couplings are shown in Figure 2.1. The fourth force, gravity, is sufficiently weak at the length and mass scales accessible to particle physicists that its effects are negligible. The coupling constants of the forces are shown on the diagrams. The electric charge, e, couples photons to charged fermions creating the electromagnetic force. The strong coupling constant, g_s, couples gluons to quarks giving the strong force. The neutral weak coupling constant, g_{Z}, couples the Z^0 boson to fermion-antifermion ($f\overline{f}$) pairs and the charged weak coupling constant, g, couples the $\mathrm{W}^\pm$ bosons to leptons and neutrinos or to quark-antiquark ($\mathrm{q}\overline{\mathrm{q}'}$) pairs.

2.2 Quark Mixing

The W^- couples to the fermions of a weak isospin doublet, i.e. leptons or quarks of the same family or generation. For example, the following interactions are possible: $\mathrm{e}^- \rightarrow \nu_\mathrm{e} + \mathrm{W}^-$ and $\mathrm{d} \rightarrow \mathrm{u} + \mathrm{W}^-$. In the case of the leptons, the coupling of the $\mathrm{W}^\pm$ takes place strictly within a particular generation and no cross-generational coupling is observed (*eg.* the $\mathrm{e}^- \rightarrow \nu_\mu + \mathrm{W}^-$ interaction does not occur). This observation has been enshrined in the laws of conservation of electron, muon and tau lepton number. With respect to quarks, the weak interaction does not strictly respect only inter-family transitions, such that the cross-generational interactions $\mathrm{s} \rightarrow \mathrm{u} + \mathrm{W}^-$ occur in addition to the $\mathrm{d} \rightarrow \mathrm{u} + \mathrm{W}^-$ interactions.

In 1963, Cabibbo suggested a solution to this paradox of the W^- decaying into two different quark-antiquark pairs which have one quark in common [5]. Cabibbo proposed that the quark weak eigenstates were actually mixtures of the quark mass eigenstates. Specifically the weak u-quark eigenstate is equal to the mass u-quark eigenstate whereas the d′-quark eigenstate is an admixture of the d-quark and the s-quark mass eigenstates. This definition is purely conventional and one could accomplish the same purpose by introducing a u′-type quark eigenstate in lieu of the d′-quark eigenstate.

To accommodate the mixing of the different quark families,[2] Cabibbo proposed a modification to the quark doublets involving a quark mixing angle θ_c (now known as the Cabibbo angle), such that [5]

$$\begin{aligned} \mathrm{d}' &= \mathrm{d}\,\cos\theta_c + \mathrm{s}\,\sin\theta_c \\ \mathrm{s}' &= -\mathrm{d}\,\sin\theta_c + \mathrm{s}\,\cos\theta_c . \end{aligned}$$

---

[2] At the time only the u,d and s quarks were known to exist.

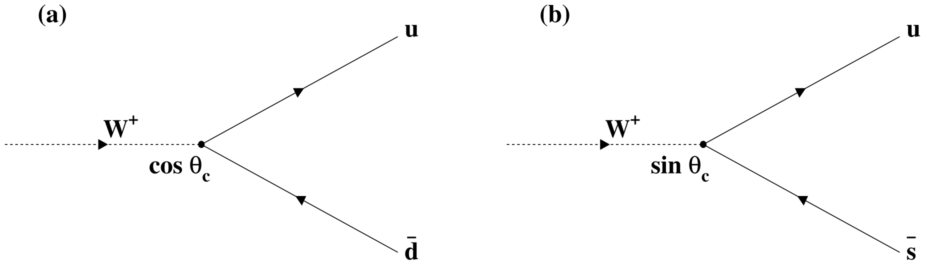

Figure 2.2: Cabibbo favoured and suppressed interactions. (a) shows the Cabibbo favoured transitions while (b) shows the Cabibbo suppressed transitions.

The strangeness-changing processes $s \rightarrow u + W^-$ are observed to be much weaker than the strangeness-conserving processes $d \rightarrow u + W^-$ consequently the Cabibbo angle is small (13.1° [3, p. 103]). Figure 2.2 shows the interactions allowed under the above scheme; diagram (a) shows the Cabibbo favoured interactions while (b) shows the Cabibbo suppressed transitions.

Cabibbo's theory was very successful in describing decays based on the uds quarks. However, this theory allowed the K^0 to decay into a $\mu^+\mu^-$ pair at a calculated decay rate in strong disagreement with the allowed experimental limit. To explain this discrepancy, Glashow, Iliopoulos and Maiani (GIM) [9] proposed the existence of a fourth quark to complete the second generation quark family in analogy to the second generation lepton family

$$\begin{pmatrix} u \\ d' \end{pmatrix}, \quad \begin{pmatrix} c \\ s' \end{pmatrix}.$$

As a consequence of the two generations, additional Feynman diagrams are possible in which the c quark replaces the u quark. Consequently, the Feynman diagrams with a u quark are cancelled by the corresponding diagrams containing a c quark, thus accounting for the absence of decays such as $K^0 \rightarrow \mu^+\mu^-$ and $K^- \rightarrow \pi^- e^+ e^-$.

Later, in 1973, before the fourth quark was even discovered, Kobayashi and Maskawa generalised the 4 quark scheme to handle three generations of quarks in an effort to explain CP violation [10]:

$$\begin{pmatrix} \mathrm{d}' \\ \mathrm{s}' \\ \mathrm{b}' \end{pmatrix} = \begin{pmatrix} V_{\mathrm{ud}} & V_{\mathrm{us}} & V_{\mathrm{ub}} \\ V_{\mathrm{cd}} & V_{\mathrm{cs}} & V_{\mathrm{cb}} \\ V_{\mathrm{td}} & V_{\mathrm{ts}} & V_{\mathrm{tb}} \end{pmatrix} \begin{pmatrix} \mathrm{d} \\ \mathrm{s} \\ \mathrm{b} \end{pmatrix}, \tag{2.1}$$

where d, s and b are the physical quarks and d$'$, s$'$ and b$'$ are the weak eigenstates. Note that the first element, $|V_{\mathrm{ud}}|$, is the Cabibbo angle $\cos\theta_c$. By convention the three quarks with charge $+\frac{2}{3}e$ are unmixed while mixing takes place between the $-\frac{1}{3}e$ charged quarks. The magnitude of the matrix elements have been experimentally measured [3, p. 103]:

$$\begin{pmatrix} 0.975 & 0.221 & 0.003 \\ 0.221 & 0.975 & 0.039 \\ 0.009 & 0.039 & 0.999 \end{pmatrix}. \tag{2.2}$$

The elements of the Cabibbo-Kobayashi-Maskawa (CKM) matrix enter as a factor into the calculation of the Feynman diagrams in determining the strength of the coupling between the $W^{\pm}$ boson and the quarks. Consequently, as will be shown in Section 2.4, the partial width depends quadratically on the CKM-matrix elements. Using these elements and neglecting phase space contributions, one can estimate the ratio of the probability of the u quark interacting with an s quark compared to the probability of the u quark interacting with a d quark to be $V_{\mathrm{us}}^2/V_{\mathrm{ud}}^2 \sim 5\%$. Consequently, the interaction of the u quark with an s quark is said to be Cabibbo suppressed.

2.3 Isospin Conservation

The concept of isospin was introduced by Heisenberg [11] in 1932 to account for the charge independence of the strong force. For example, the strong force cannot distinguish between the proton and neutron or the three different states of the pion meson. The members of an isospin multiplet are in essence the same particle appearing with different orientations in isospin space or with different charges ($Q = T_3 + Y/2$). Using Noether's Theorem [12], Heisenberg asserted that the strong force is invariant under a rotation in isospin space implying that isospin is conserved in all strong interactions.

An important application of isospin conservation arises from the strong interactions between non-identical particles. It is used in this analysis to determine the branching ratio of the $\tau^- \to \mathrm{K}^*(892)^- \nu_\tau$ decay mode from the branching ratio of the $\tau^- \to \pi^- \overline{\mathrm{K}}^0 \nu_\tau$ decay mode measured in this work. The $\mathrm{K}^*(892)^-$ meson decays into two final states: $\pi^- \overline{\mathrm{K}}^0$ and $\mathrm{K}^- \pi^0$. The relationship between the $\mathrm{K}^*(892)^-$ meson and these decay products is described below.

The isospin of a particle is commonly displayed as a Dirac ket $|T\ T_3\rangle$, where T is the eigenvalue for the isospin operator and T_3 is the eigenvalue for the projection operator along the third direction of T. For the particles in this example, the Dirac kets are:

$$|\mathrm{K}^{*-}\rangle = |\tfrac{1}{2}\ -\tfrac{1}{2}\rangle, \quad |\mathrm{K}^-\rangle = |\tfrac{1}{2}\ -\tfrac{1}{2}\rangle, \quad |\overline{\mathrm{K}}^0\rangle = |\tfrac{1}{2}\ \tfrac{1}{2}\rangle \quad \text{and} \quad |\pi^0\rangle = |1\ 0\rangle. \tag{2.3}$$

The isospin states of the possible decay products of the $\mathrm{K}^*(892)^-$ meson can be calculated using Clebsch-Gordon coefficients [3, p. 183] to be

$$\begin{aligned} |\pi^- \overline{\mathrm{K}}^0\rangle &= \sqrt{1/3}|\tfrac{3}{2}\ -\tfrac{1}{2}\rangle - \sqrt{2/3}|\tfrac{1}{2}\ -\tfrac{1}{2}\rangle \text{ and} \\ |\mathrm{K}^- \pi^0\rangle &= \sqrt{2/3}|\tfrac{3}{2}\ -\tfrac{1}{2}\rangle + \sqrt{1/3}|\tfrac{1}{2}\ -\tfrac{1}{2}\rangle. \end{aligned} \tag{2.4}$$

Requiring isospin invariance, the $|\tfrac{3}{2}\ -\tfrac{1}{2}\rangle$ terms are eliminated giving

$$|\mathrm{K}^{*-}\rangle = \sqrt{1/3}|\mathrm{K}^- \pi^0\rangle - \sqrt{2/3}|\overline{\mathrm{K}}^0 \pi^-\rangle. \tag{2.5}$$

Note that the charge conjugate state gives the same conservation relation with all the signs reversed. As described in the next section, the decay width is proportional to the square of the amplitudes (Dirac ket coefficients), subsequently the branching ratio of the $\tau^- \to \mathrm{K}^*(892)^- \nu_\tau$ branching ratio is equal to 1.5 times the $\tau^- \to \pi^- \overline{\mathrm{K}}^0 \nu_\tau$ branching ratio. The branching ratio of the $\tau^- \to \mathrm{K}^*(892)^- \nu_\tau$ decay mode will be calculated in Chapter 8.

2.4 Tau Hadronic Decays

Of the three charged leptons — the electron, muon and tau — only the latter is massive enough to have hadronic decay modes. Thus an entirely new regime of study is opened up, since the tau can decay into both strange and non-strange mesons. The total width of the tau (Γ_τ) is given by the sum of the widths of each tau decay (Γ_i) and is inversely proportional to the τ^- lifetime (τ_τ). The branching ratio of the tau lepton to any given final state is defined as the ratio of the partial decay width to the total decay width for example

$$B(\tau^- \to h^- \nu_\tau) = \frac{\Gamma(\tau^- \to h^- \nu_\tau)}{\Gamma_\tau}, \tag{2.6}$$

where h^- represents any hadronic final state. Table 2.2 shows the average branching ratios of the τ divided into categories based on the topologies of the final states.

The differential decay width for a particle of mass m can be written as [2],

$$\mathrm{d}\Gamma = \frac{1}{2m} |\mathcal{M}|^2 \, \mathrm{dPS}, \tag{2.7}$$

where dPS is the Lorentz invariant phase space factor and $\mathcal{M}$ is the invariant amplitude for semi-leptonic decays and contains the dynamical information about the decay which can be evaluated from a Feynman diagram. For any τ^- two-body decay

Decay mode	Branching ratio (%)
$\tau^- \to \mathrm{e}^- \overline{\nu}_\mathrm{e} \nu_\tau$	17.81 ± 0.07
$\tau^- \to \mu^- \overline{\nu}_\mu \nu_\tau$	17.37 ± 0.09
$\tau^- \to h^- \nu_\tau$	12.32 ± 0.12
$\tau^- \to h^- \pi^0 \nu_\tau$	25.84 ± 0.14
$\tau^- \to h^- \geq 2\pi^0 \nu_\tau$	10.79 ± 0.16
$\tau^- \to (\mathrm{3prong})^- \nu_\tau$	15.18 ± 0.13
$\tau^- \to (\mathrm{5prong})^- \nu_\tau$	0.097 ± 0.007

Table 2.2: The major decay modes of the τ. For this table, the h denotes both charged π and K mesons. Decays with 3- and 5-prongs include those decays with 3 and 5 charged hadrons, respectively.

into a meson P and a neutrino, one gets

$$\mathrm{dPS} = \frac{1}{8\pi^2}\left(1 - \frac{m_P^2}{m_\tau^2}\right) \mathrm{d}\Omega, \tag{2.8}$$

where $\mathrm{d}\Omega$ is the solid angle element, m_τ is the mass of the τ^- lepton and m_P is the mass of the meson. The Lorentz invariant phase space factor contains the kinematic information of the decay. The matrix element can be written in the form of a current-current interaction, such that

$$\mathcal{M}(\tau^- \to h^- \nu_\tau) = \frac{G_F}{\sqrt{2}} |V_{\mathrm{CKM}}| L_\mu J^\mu, \tag{2.9}$$

where $|V_{\mathrm{CKM}}|$ is the magnitude of the CKM matrix element and G_F is the Fermi coupling constant. This factor includes all the numerical factors involved in coupling the fermions to the gauge bosons. L_μ describes the leptonic tau current, and is given by

$$L_\mu = \overline{u}_{\nu_\tau} \gamma_\mu (1 - \gamma_5) u_\tau, \tag{2.10}$$

where u and $\overline{u}$ are Dirac spinors and γ_μ and γ_5 are Dirac matrices. The hadronic transition current J_μ describes how the hadronic system h^- is formed from the vacuum by the weak current. If one is restricted to a V-A structure, J_μ can be written as

$$J_\mu = \langle h | V_\mu(0) - A_\mu(0) | 0 \rangle, \tag{2.11}$$

where $V_\mu(0)$ and $A_\mu(0)$ are the vector and axial-vector quark currents, respectively, operating on the vacuum. The vector part of the hadronic current leads to final states with even G-parity, or an even number of pions, while the axial-vector part couples to odd G-parity states, or an odd number of pions.

Finally, the Lorentz invariant amplitude for the decay $\tau^- \to h^- \nu_\tau$ is expressed as

$$\mathrm{d}\Gamma = \frac{G_F^2}{4m_\tau^2} |V_{\mathrm{CKM}}|^2 L_{\mu\nu} J^{\mu\nu}\, \mathrm{dPS}. \tag{2.12}$$

In the rest frame of the h^- system, the tensor product simplifies to a sum over various structure functions and kinematic factors. For simple τ decays into only one hadron, the hadronic current is easily determined using knowledge of the four vectors of the decay products. If the final state contains two or more hadrons, the hadronic transition current becomes much more complicated. For a complete explanation of the hadronic structure functions for final states containing strange mesons see references [13, 14].

The calculation of the τ decay rate requires knowledge of the hadronic current J_μ. The simplest, most general, form of the hadronic current is $iV_{\mathrm{CKM}} f_P\, p_\mu^P$ for a pseudoscalar meson (*eg.* π^-, K^-) and $iV_{\mathrm{CKM}} f_V\, \epsilon_\mu^V$ for a vector meson (*eg.* ρ^-, $\mathrm{K}^*(892)^-$), where V_{CKM} is the CKM matrix element for the corresponding meson. The f_P and f_V are the decay constants representing the unknown coupling between the W^- boson and the quarks, while p_μ^P is the momentum four vector for the pseudoscalar mesons and ϵ_μ^V is the polarization four vector for the vector mesons. The decay constants of the pseudoscalar mesons can be determined experimentally from the leptonic decay of the meson. This is not practical for the vector mesons, consequently a ratio of the decay widths of two different decays is used to give an indirect measurement.

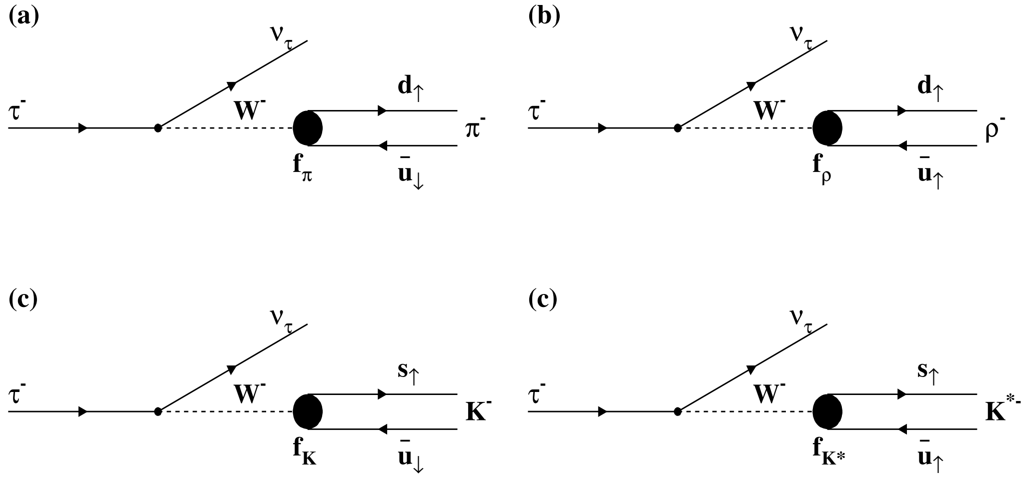

Figure 2.3: Feynman diagrams of of τ^- decays into pseudoscalar and vector mesons. The pseudoscalar final states are on the right while the vector final states are on the left. The coupling constant for each decay is indicated on the diagrams. Note that the spins of each quark-antiquark pair may be reversed giving the same magnitude of the total spin of the meson.

Figure 2.3 shows the Feynman diagrams for four different final states of the τ^-. The lefthand plots show the pseudoscalar meson final states while the righthand plots show the vector meson final states for non-strange and strange decays, respectively. The decay rate for any of these diagrams is evaluated by integrating equation 2.12 and averaging over the initial spin of the τ^- and summing over the final state spins. The decay rate for a τ^- to decay into a pseudoscalar meson is

$$\Gamma(\tau^- \to P^-\nu_\tau) = \frac{G_F^2 V_{\text{CKM}}^2 f_P^2 m_\tau^3}{16\pi}\left(1 - \frac{m_P^2}{m_\tau^2}\right)^2, \tag{2.13}$$

where V_{CKM} is the CKM matrix element, m_P is the mass of the pseudoscalar meson and f_P represents the coupling of the W$^-$ to the pseudoscalar meson. The decay rate for the $\tau^- \to \pi^-\nu_\tau$ decay mode is obtained by replacing f_P with f_π and using $V_{\text{CKM}} = \cos\theta_c$. Similarly, the decay width for the $\tau^- \to \text{K}^-\nu_\tau$ decay mode is obtained by replacing f_P with f_{K} and using $V_{\text{CKM}} = \sin\theta_c$. The decay constants f_π and f_{K}

have the values 130.7 ± 0.4 MeV and 159.8 ± 1.5 MeV [3, p. 353], respectively.

The decay rate for a τ^- to decay into a vector meson, V, can be approximated if one assumes the narrow-width approximation for V and ignores radiative corrections. The narrow-width approximation assumes that the lifetime of the vector meson is infinite and subsequently that it does not decay. The radiative corrections can be neglected in this work because they will cancel when the ratio of the $\tau^- \to \rho^-\nu_\tau$ and $\tau^- \to \mathrm{K}^*(892)^-\nu_\tau$ decay rates is calculated. However, the widths of the two mesons are not negligible. Therefore, there is a small unknown theoretical uncertainty in the calculated ratio of the decay rates. The $\tau^- \to V^-\nu_\tau$ decay rate is [15]

$$\Gamma(\tau^- \to V^-\nu_\tau) = \frac{G_F^2 V_{\mathrm{CKM}}^2 f_V^2 m_\tau^3}{64\pi^2}\left(1 - \frac{m_V^2}{m_\tau^2}\right)^2\left(1 + \frac{2m_V^2}{m_\tau^2}\right), \tag{2.14}$$

where f_V represents the coupling of the W^- to the vector meson and m_V is the mass of the vector meson. For the decays $\tau^- \to \mathrm{K}^*(892)^-\nu_\tau$ and $\tau^- \to \rho^-\nu_\tau$, equation 2.14 can be modified by replacing m_V and f_V with the corresponding masses ($m_{\mathrm{K}*}$ and m_ρ) and couplings ($f_{\mathrm{K}*}$ and f_ρ). In addition, the CKM matrix element V_{CKM} is $\sin\theta_c$ for the $\tau^- \to \mathrm{K}^*(892)^-\nu_\tau$ decay and $\cos\theta_c$ for the $\tau^- \to \rho^-\nu_\tau$ decay.

The calculation of the decay rate for the τ^- to decay into a final state with two or three mesons is more complicated and is not shown here; for complete details see [13, 14]. The $\tau^- \to (\pi\mathrm{K})^-\nu_\tau$ decay mode, shown in Figure 2.4, proceeds through the weak hadronic vector current. If one assumes that nearly all of the $\tau^-\to(\pi\mathrm{K})^-\nu_\tau$ decays pass through the $\mathrm{K}^*(892)$ resonance, equation 2.14 can approximate the $\tau^-\to(\pi\mathrm{K})^-\nu_\tau$ decay width and subsequently the decay's branching ratio. The $\tau^-\to(\pi\pi)^-\nu_\tau$ branching ratio can be similarly estimated using the $\tau^- \to \rho^-\nu_\tau$ branching ratio. If one imposes isospin conservation on the two possible decay modes of the $\mathrm{K}^*(892)$ meson, then predictions of the $\tau^- \to \pi^-\overline{\mathrm{K}}^0\nu_\tau$ and $\tau^- \to \mathrm{K}^-\pi^0\nu_\tau$ branching ratios are possible.

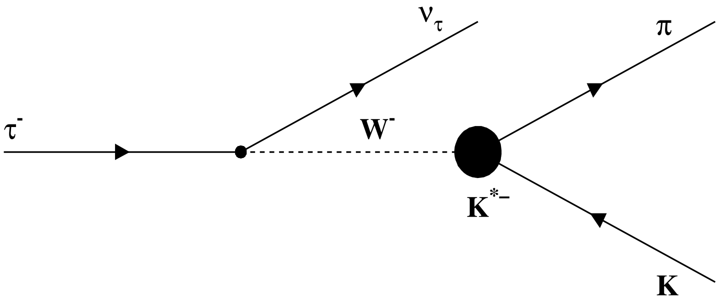

Figure 2.4: A Feynman diagram of the $\tau^- \to (\pi\mathrm{K})^-\nu_\tau$ decay.

Once the branching ratios are measured, the decay constants for various vector mesons can be approximated using equation 2.14,

$$f_V = \frac{8\pi}{G_F V_{\mathrm{CKM}} m_\tau^{3/2}} \left(1 - \frac{m_V^2}{m_\tau^2}\right)^{-1} \left(1 + \frac{2m_V^2}{m_\tau^2}\right)^{-1/2} \sqrt{\frac{B(\tau^- \to V^-\nu_\tau)}{T_\tau}}, \qquad (2.15)$$

where $G_F = 1.16639 \times 10^{-5}$ GeV^{-2} [3, p. 69]. Using the particle masses from reference [3, p. 286 and 364] and the current world average branching ratio for the $\tau^- \to \rho^-\nu_\tau$ decay mode, $B(\tau^- \to \rho^-\nu_\tau) = 0.2532 \pm 0.0015$ [3, p. 286], one approximates f_ρ to be 742.4±0.8±2.2 MeV, where the first error comes the uncertainty in V_{ud} and the second from the uncertainty in the branching ratio. Similarly, the decay constant $f_{\mathrm{K}*}$ can be approximated using the $\tau^- \to \mathrm{K}^*(892)^-\nu_\tau$ branching ratio, $B(\tau^- \to \mathrm{K}^*(892)^-\nu_\tau) = 0.0128 \pm 0.0008$ [3, p. 286], giving $f_{\mathrm{K}*} = 764.8 \pm 13.6 \pm 24.3$ MeV, where the first error comes from the uncertainty in V_{us} and the second from the uncertainty in the branching ratio. A new estimate of the decay constant $f_{\mathrm{K}*}$, using the branching ratio of the $\tau^- \to \mathrm{K}^*(892)^-\nu_\tau$ decay mode calculated in this work, is presented in Chapter 8.

For the last 30 years, several authors have been studying the properties of the decay constants of various mesons. One such study, presented by Oneda [16] shows the calculation of several different decay constant relations using a set of sum rules originally derived by Das, Mathur and Okubo (DMO) [17]. Oneda predicts that in the flavour-$SU_f(3)$ symmetry limit ($m_{\mathrm{u}} = m_{\mathrm{d}} = m_{\mathrm{s}}$), the decay constants are expected to be equal, $f_\rho = f_{\mathrm{K}^*}$ [16]. Oneda makes a second prediction based on asymptotic flavour-$SU_f(3)$ symmetry at high energies resulting in

$$\frac{f_\rho}{m_\rho} = \frac{f_{\mathrm{K}^*}}{m_{\mathrm{K}^*}}. \tag{2.16}$$

Under the narrow width assumption, this work uses the ratio of the $\tau^- \to \rho^- \nu_\tau$ decay width with respect to the $\tau^- \to \mathrm{K}^*(892)^- \nu_\tau$ decay width to give an independent check on the decay constants:

$$\frac{f_\rho}{f_{\mathrm{K}^*}} = \tan\theta_c \sqrt{\frac{B(\tau^- \to \rho^- \nu_\tau)}{B(\tau^- \to \mathrm{K}^*(892)^- \nu_\tau)}} \left(\frac{m_\tau^2 - m_{\mathrm{K}^*}^2}{m_\tau^2 - m_\rho^2}\right) \sqrt{\frac{m_\tau^2 + 2m_{\mathrm{K}^*}^2}{m_\tau^2 + 2m_\rho^2}}. \tag{2.17}$$

This ratio uses only the branching ratios, masses and the Cabibbo angle and is independent of of the Fermi coupling constant, tau lifetime and any radiative corrections, assuming that the two decays have the same radiative corrections. The ratio f_ρ/f_{K^*} is calculated using the $\tau^- \to \mathrm{K}^*(892)^- \nu_\tau$ branching ratio calculated in this work in Chapter 8 and is compared to other recent measurements and theoretical expectations.

The decay widths of the remaining decay modes studied in this work can be estimated in a manner similar to that described above. The branching ratio predictions are compared to the measurements from this work in Chapter 8.

Chapter 3

LEP and the OPAL Detector

This chapter will describe the experimental facility used to collect the data for this analysis. The first section will describe the Large Electron Positron (LEP) [18] collider facility at CERN just outside Geneva, Switzerland. The second section describes the OPAL detector and the performance of the detector since 1991.

3.1 The LEP Collider

The LEP collider facility consists of several different particle accelerators that are used to create high energy electrons and positrons and bring them into collision. From 1989 to 1995 the injector chain produced and accelerated electrons and positrons to 20 GeV, while the main ring accelerated the particles to approximately 45 GeV, providing the centre-of-mass energy of 90 GeV required for Z^0 physics. Recent improvements to the LEP collider now allow electrons and positrons to reach energies close to 100 GeV.

Figure 3.1 shows a schematic diagram of the LEP injector chain. Positrons are produced by directing electrons from a 200 MeV linac onto a converter target. The electrons and positrons are then accelerated in a 600 MeV linac and collected in the Electron-Positron Accumulator (EPA). After accumulation in the EPA, the electrons and positrons are injected into the Proton Synchrotron (PS) where they are accelerated to 3.5 GeV and then transferred to the Super Proton Synchrotron (SPS) which accelerates the particles to 20 GeV. The SPS was made famous in the 1980's for the discovery of the Z^0 and $W^{\pm}$ bosons [19,20]. The final acceleration to 45 GeV is done in the LEP ring.

The LEP ring is 26.66 km in circumference and is buried between 100 m and 150 m underground (see figure 3.1). The LEP ring consists of a repeating set of horizontally deflecting dipole magnets and alternating focusing and defocusing quadrapole magnets. This forms a strong focusing lattice that keeps the beams circulating in opposite directions on closed stable orbits around the ring. Radio frequency (RF) cavities provide the accelerating force on each beam. Once the beams reach their operating energy, set by the bending field of the dipole magnets, the RF cavities compensate for synchrotron radiation losses. The collider successfully reached the design peak luminosity of $1.6 \times 10^{31}\mathrm{cm}^{-2}\mathrm{s}^{-1}$ at an average beam current of 3 mA, corresponding to the production of a Z^0 boson approximately every second. LEP has been operated in four and eight bunch mode. In four bunch mode there are four equally spaced bunches each of electrons and positrons which are made to collide at four intersection points which are instrumented with large detectors. After 1992, LEP operated in eight bunch mode, with eight circulating bunches per beam.

3.2 The OPAL Detector

OPAL is one of four large detectors whose purpose is to detect all types of interactions occurring in e^+e^- collisions at a centre of mass energy up to 200 GeV. A full description of the detector can be found in reference [21] and a schematic of the OPAL detector is shown in Figure 3.2. The detector has a cylindrical geometry and

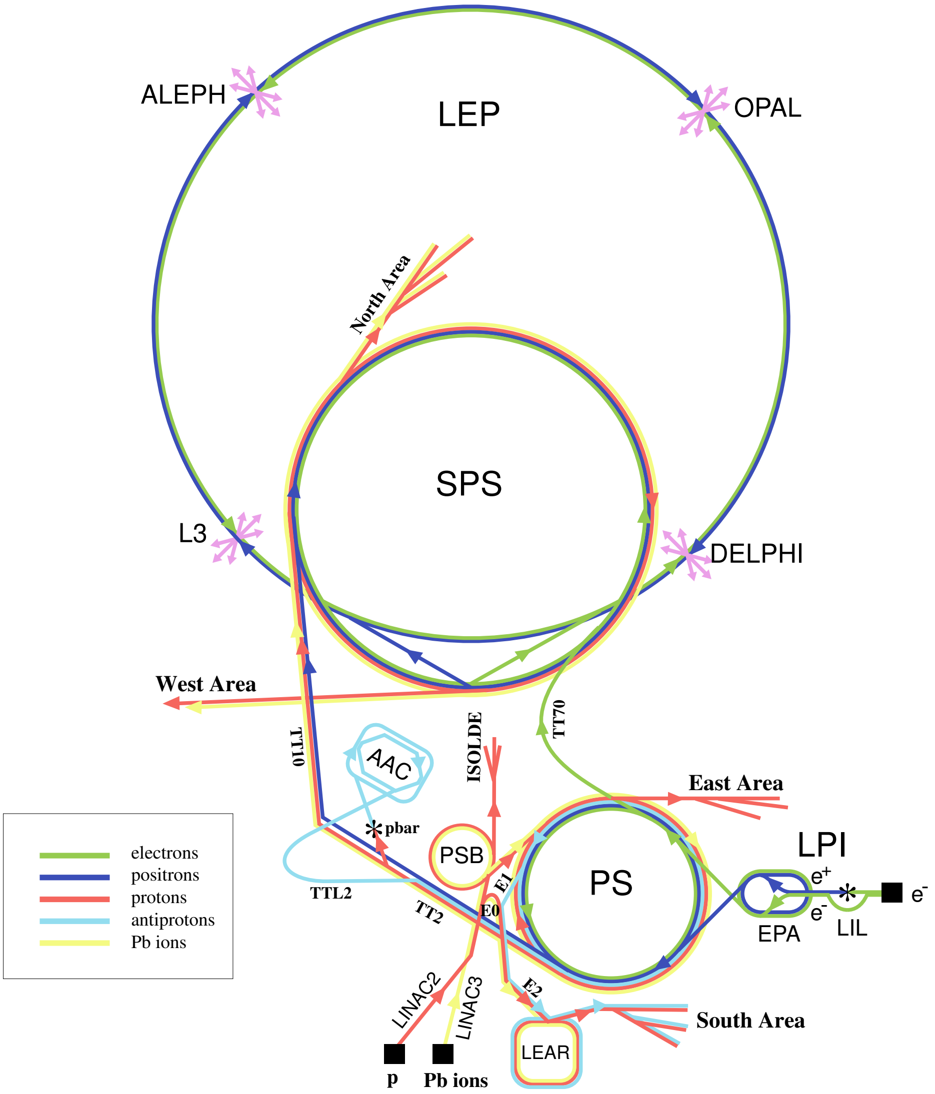

LEP: Large Electron Positron collider
SPS: Super Proton Synchrotron
AAC: Antiproton Accumulator Complex
ISOLDE: Isotope Separator OnLine DEvice
PSB: Proton Synchrotron Booster
PS: Proton Synchrotron

LPI: Lep Pre-Injector
EPA: Electron Positron Accumulator
LIL: Lep Injector Linac
LINAC: LINear ACcelerator
LEAR: Low Energy Antiproton Ring

Rudolf LEY, PS Division, CERN, 02.09.96

Figure 3.1: Schematic diagram of the CERN accelerator complex. The LEP injection chain and the accelerators used for proton/antiproton physics and heavy ion physics are shown.

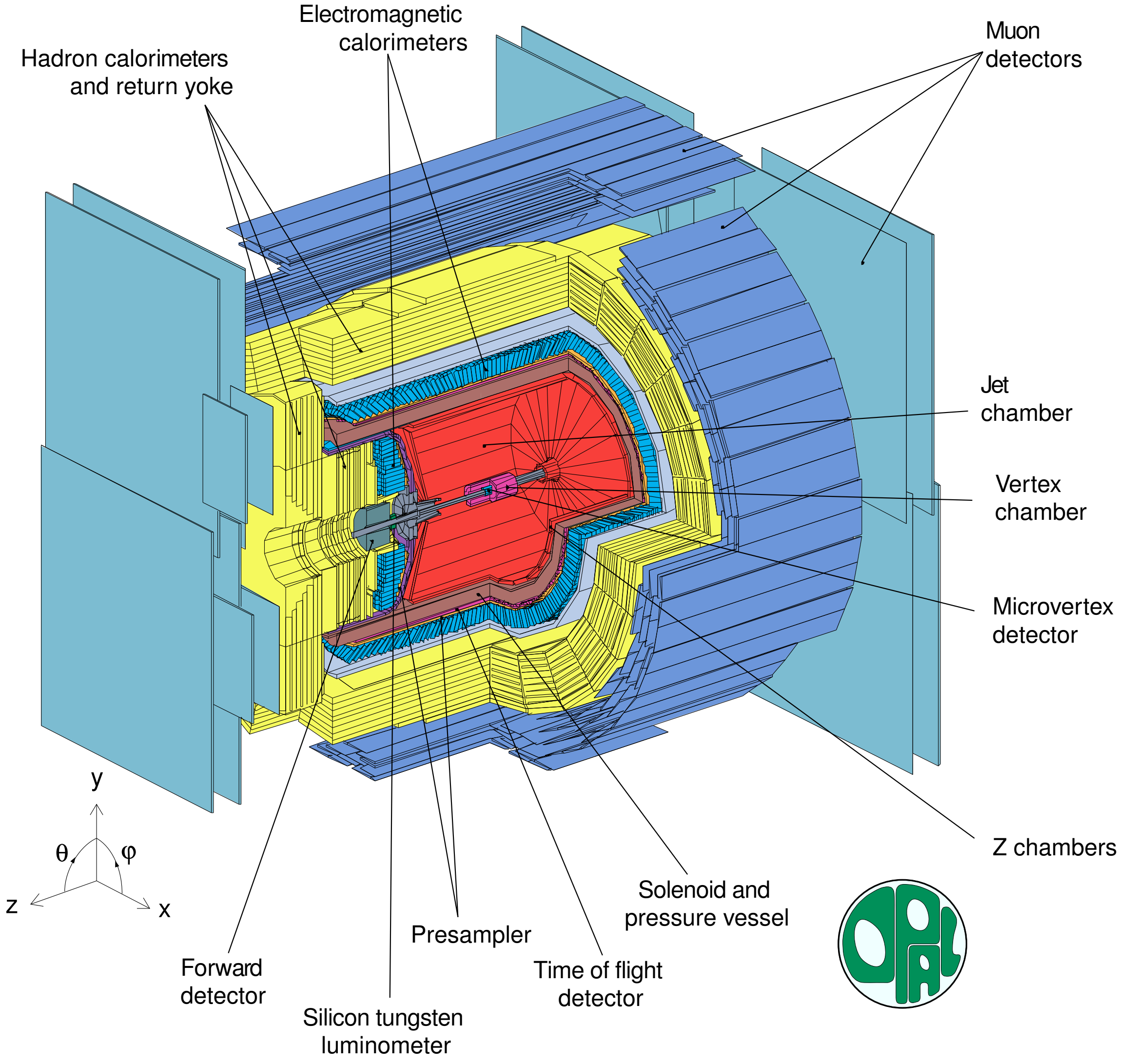

Figure 3.2: Cut-away view of the OPAL detector showing the various subdetector components, the components used in this analysis are described in the text. The OPAL coordinate system is indicated; the electron (positron) beam enters the detector from the right (left); and the detector dimensions are approximately (12 × 12 × 12) m^{2}.

is coaxial with the LEP beam pipe.

The coordinate system used by OPAL is illustrated in Figure 3.2; the x-axis is horizontal and points toward the centre of LEP, the y axis is vertical, and the z-axis is in the e^- beam direction. The origin of the coordinate system is at the nominal interaction point at the centre of the detector. The polar angle, θ, is measured from the z-axis about the x-axis, and the azimuthal angle, ϕ, is measured from the x-axis about the z-axis.

The e^+e^- interactions take place in a 10.7 cm diameter evacuated beryllium beam pipe surrounded by the inner tracking detectors (see Figure 3.3) that measure the direction, momentum and energy loss (dE/dx) of charged particles. A solenoidal magnet, located outside the inner tracking detectors, provides a magnetic field of 0.435 T in the direction of the electron beam. The momenta of charged particles is determined from their curvature in the magnetic field. Outside the inner detectors are calorimeters that measure the total energy of all particles, except neutrinos and muons. A set of detectors for detecting muons surrounds the calorimeters. The following sections describe the OPAL detector components used in this analysis in order of increasing radius from the beam.

3.2.1 The Central Tracking System

The central tracking system consists of a silicon microvertex detector and three drift chamber devices: the vertex chamber, the jet chamber and the z-chamber. The three drift chambers operate at a pressure of 4 bar with a gas mixture of 88.2% argon, 9.8% methane and 2.0% isobutane inside a pressure vessel whose cylindrical structure provides mechanical support to the solenoidal magnet mounted around it. Only the vertex chamber and the jet chamber are used in this analysis. They are described below.

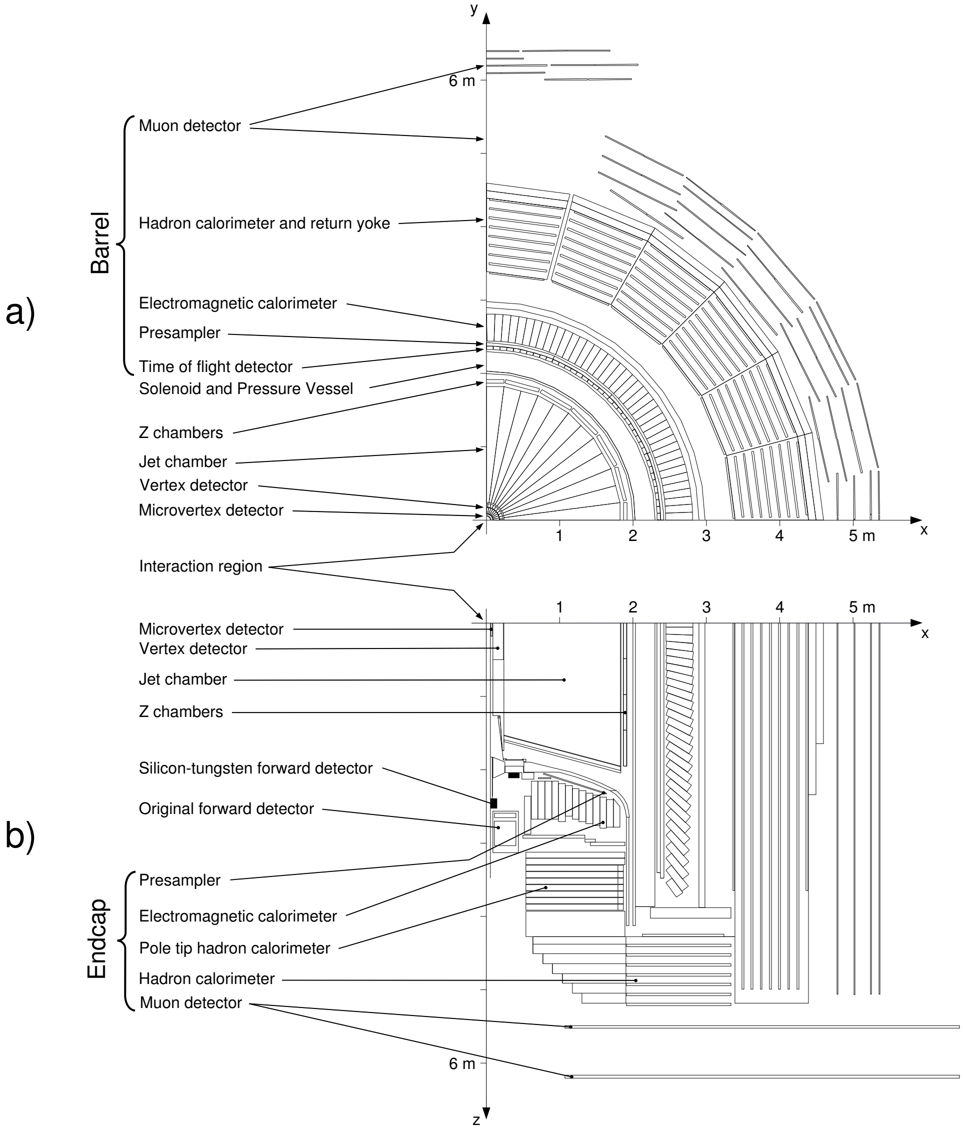

Figure 3.3: Cut-away of two quarters of the OPAL detector showing the front view of the barrel (a) and top views (b) for both the barrel and endcap regions.

The Central Vertex chamber (CV) is a high resolution cylindrical drift chamber which extends radially from 88 mm to 235 mm from the interaction point. The detector is composed of an inner layer of thirty-six axial wire cells, each composed of twelve anode sense wires, and an outer layer of thirty six *stereo* cells inclined at 4°, each with six anode wires. The drift time to the axially placed sense wires can be measured precisely enough so that the position of a track in the $r-\phi$ plane is calculated with a resolution of 55 μm. The time difference between signals at either end of the sense wires gives a relatively coarse z coordinate measurement (4 cm) which is used by the OPAL track triggering and in pattern recognition. The combination of the stereo layer and axially placed sense wires provides an accurate z measurement for charged particles close to the interaction region with a resolution of 700 μm.

The Central Jet chamber (CJ) is a large cylindrical drift chamber with a length of approximately 4 m, surrounding the beam pipe and vertex chamber. The outer diameter is 3.7 m, the inner diameter is 0.5 m. It is divided into 24 identical sectors in ϕ each containing a sense wire plane with 159 anode wires and two cathode wire planes that form the boundaries between adjacent sectors. The anode wires are located between radii of 255 mm and 1835 mm, equally spaced by 10 mm and alternating with potential wires. To resolve left-right ambiguities, the anode wires are staggered by ± 100 μm alternately to the left and right side of the plane defined by the potential wires. Similar to the vertex chamber, a measurement of the drift time determines the coordinates of wire hits of a track in the $r-\phi$ plane with a resolution of 135 μm. The ratio of the charges between the signals at either end of the wires gives a measure of the z-position with a resolution of 6 cm. The ionization energy loss of the charged particles, $\mathrm{dE}/\mathrm{d}x$, is measured by integrating the charge received at each end of a wire, allowing identification of particles by determining the velocity and momentum simultaneously. This technique will be discussed in more detail in Section 4.1.

The momentum of the particle is obtained by measuring the curvature of the particle track in the axial magnetic field. The momentum resolution for the jet chamber is given by

$$\frac{\sigma_p}{p} = \frac{\sigma_{p_T}}{p_T} = \sqrt{(0.0004 + (0.0015 \times p_T)^2)},$$

where p_T in GeV$/c$ is the momentum component transverse to the beam direction [22]. The momentum dependent term is calculated from the momentum resolution of $Z^0 \to \mu^+\mu^-$ events while the constant term is due to multiple scattering at low energies. Note that both the momentum resolution, and the transverse momentum resolution are identical in the barrel region of the OPAL detector, since the curvature error (error in the x-y plane) dominates; the error of the dip angle[1] λ can be neglected.

3.2.2 Time-of-Flight System

Surrounding the tracking detectors and magnet is the time-of-flight (TOF) system. The TOF system covers the barrel region (TB), $|\cos\theta| < 0.82$, of the OPAL detector. It is comprised of 160 scintillation counters, at an average radius of 2.36 m. The TOF provides a timing resolution of 460 ps for muons and a z-resolution of 5.5 cm. The z-position is measured by comparing the time difference between the signals at the ends of the scintillators. The timing resolution allows the TOF detector to be used for cosmic ray rejection and as a trigger veto for events which are not synchronous with LEP bunch crossings.

---

[1] The maximum angle in the vertical plane with respect to the x-y plane, defined as $\tan\lambda = \cot\theta$.

3.2.3 Electromagnetic Calorimeter

The electromagnetic calorimeter (ECAL) of OPAL is outside both the pressure vessel of the tracking system and the coil of the magnet. It consists of a pre-shower counter (pre-sampler) and a lead glass calorimeter. The electromagnetic calorimeter is designed to contain and measure the energy and position of electrons, positrons, and photons.

The electromagnetic pre-sampler is located immediately in front of the electromagnetic calorimeter. It consists of two concentric cylinders of limited streamer tubes with wires parallel to the beam axis and cathode strips oriented at $\pm 45^\circ$ with respect to the wires. The pre-sampler samples the energy of a particle after it passes through the magnetic coil, enabling one to make a correction if the shower has started in the coil.

The barrel region (EB) of the electromagnetic calorimeter covers $|\cos\theta| < 0.82$ and the endcap region (EE) covers $|\cos\theta|$ from 0.81 to 0.95. For this analysis, only those events fully contained in the barrel region are used. The barrel electromagnetic calorimeter consists of two half-ring sections that form a cylindrical array of 9440 SF57 [23] lead-glass blocks with 59 blocks in the z-direction and 160 blocks in the ϕ direction. Each block is $24.6X_0$ thick (where $X_0 = 1.5$ cm for the lead-glass)[2] with an area of approximately $10\,\mathrm{cm} \times 10\,\mathrm{cm}$. Located 2455 mm from the beam, this corresponds to an angular coverage of approximately $40\,\mathrm{mr} \times 40\,\mathrm{mr}$. The blocks are oriented so that they point back toward the interaction region with a slight offset to minimise the possibility that a particle will pass through a crack between the blocks. Čerenkov light produced by relativistic charged particles in the blocks is detected by

---

[2] X_0 is referred to as the radiation length and is defined as the mean distance over which a high energy electron loses all but $1/e$ of its energy by bremsstrahlung.

phototubes at the base of each block.

The effective energy resolution of the electromagnetic calorimeter is $\sigma_E/E = (1.8\% + 23\%/\sqrt{E})$, where E is measured in GeV [24]. Lead-glass was chosen for the electromagnetic calorimeter because of its excellent intrinsic energy resolution ($\sigma_E/E \sim 5\%/\sqrt{E}$), linearity, spatial resolution ($\sim$ 1 cm), granularity, electron-hadron discrimination, hermiticity and gain stability. However, the resolution is degraded by the approximately $2X_0$ of material located in front of the calorimeter, the solenoid, central detector and pressure vessel, which usually initiate early showering.

3.2.4 Hadron Calorimeter

Outside the electromagnetic calorimeter is the iron return yoke of the magnet, which is instrumented using streamer tubes with pads and strips to form a hadron calorimeter (HCAL). The HCAL measures the energy of hadrons emerging from the ECAL and can assist in the identification of muons. The HCAL is divided into three parts: the barrel (HB) covering $|\cos\theta| < 0.81$, the endcap (HE) covering $0.815 < |\cos\theta| < 0.91$, and the pole tip (HT) covering $0.91 < |\cos\theta| < 0.99$.

The barrel hadron calorimeter (see Figure 3.4(a)) consists of 9 layers of chambers, alternated with 8 iron slabs spanning radii from 3.4 to 4.4 m. In addition, another iron slab is located beyond the last active detector layer. The slabs are 100 mm thick and are separated by 25 mm gaps giving over four nuclear interaction lengths (λ) of absorber material.[3] Note that there is a further 2.2λ of material located in front of the HCAL. The active material, i.e. the detectors, of the calorimeter consists of nine 25 mm thick plastic streamer tubes, usually called HCAL layers (see Figure 3.4(b)). Each streamer tube layer consists of a series of chambers, with each chamber containing

---

[3] The interaction length, λ, is defined as the mean free path of a particle before undergoing a nuclear collision.

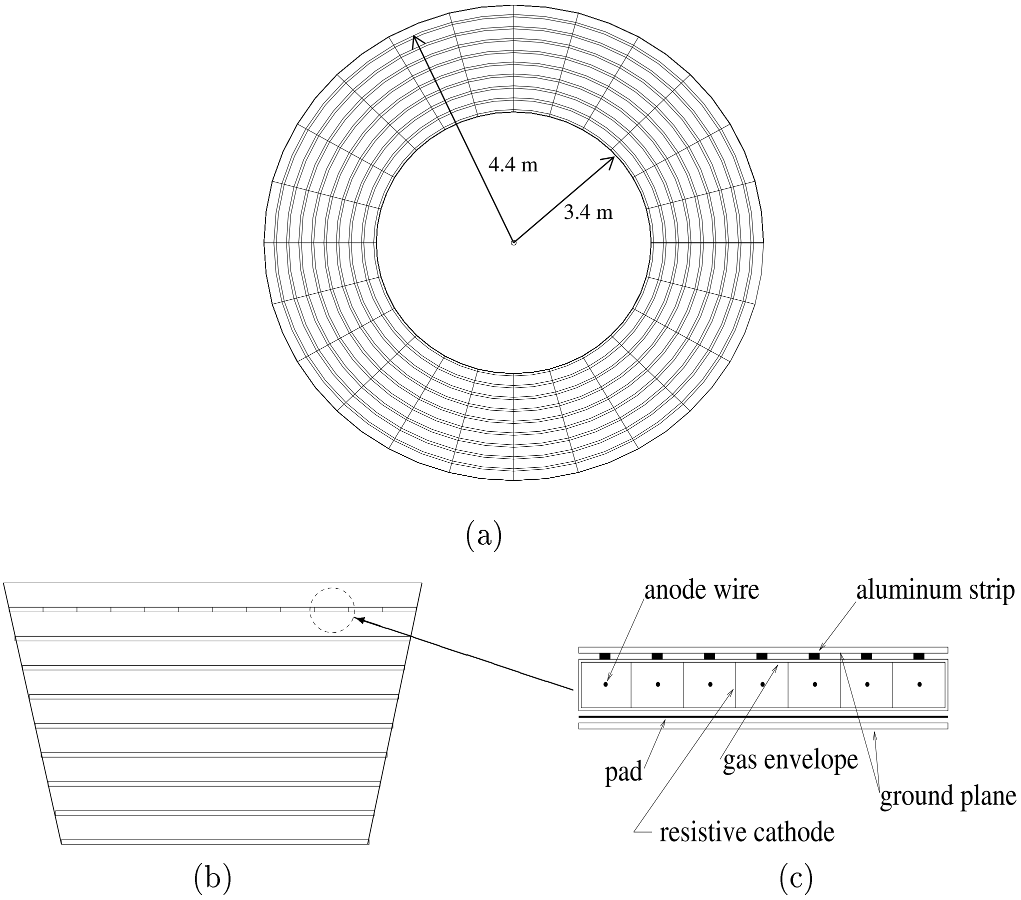

Figure 3.4: The barrel hadron calorimeter. Figure (a) shows an endview of the HCAL barrel; Figure (b) shows the cross-section of one of the barrel wedges and Figure (c) shows the cross-section of one of the chambers in a layer.

seven or eight cells to optimise coverage depending upon the width of that layer (see Figure 3.4(c)). Each chamber is contained within a gas envelope which is filled with a mixture of 75% isobutane and 25% argon. Each cell has three cathode walls and an anode wire in the centre. The signals are read out on both the upper and lower faces of the chambers. The detected pulses are induced through the grounded cathode and the gas envelope to the pads under the chambers and to the 4 mm aluminum strips above the anode wires in each cell, respectively.

The HCAL Strips (HS) are read out at either end of the gas envelope providing

57,000 individual signals. These signals can provide precise single particle tracking and can provide the profile of the shape of a hadronic shower.

The pads are grouped together to form HCAL Towers (HT), which divide the solid angle into 976 equal elements radiating out from the interaction region. There are 48 bins in ϕ and 21 bins in θ. Unit gain analogue summing amplifiers sum the signals from the pads in each tower to provide an estimate of the energy of the hadronic showers.

The effective energy resolution is calculated (see Appendix A.2) using minimum ionising pions from τ^- decays giving $\sigma_{HB}/E = (0.165 \pm 0.024) + (0.847 \pm 0.100)/\sqrt{E}$, where E is in GeV. This measurement takes into account the probability of hadronic interactions being initiated in the 2.2 interaction lengths of material in front of the hadron calorimeter.

3.2.5 Muon Chambers

Most electrons, hadrons and photons are stopped by the calorimeters but muons above a threshold energy penetrate beyond the calorimeters. Therefore, outside the hadron calorimeter are four layers of drift chambers to identify muons. The chambers measure the position and direction of all charged particles leaving the hadron calorimeter. Ninety-three percent of the solid angle is covered by at least one layer of the muon chamber, with some gaps in the acceptance due to the beam pipe, the supporting legs and the cables. Each layer is constructed of 110 large-area drift chambers, 1.2 m wide and 90 mm deep. The barrel region (MB) covers $|\cos\theta| < 0.68$ while the endcap region (ME) covers $0.67 < |\cos\theta| < 0.98$.

3.2.6 Trigger

The primary event selection is performed by the trigger system which uses a high level of redundancy to provide good acceptance for studies of Z^0 decays. Each subdetector component provides independent signals which are examined after each beam collision to see if an interesting interaction or event has occurred. Two types of signals are used by the central trigger processor to make a decision on whether the event represents a potentially interesting physics process.

Each subdetector provides *direct* trigger signals that are estimates of quantities such as the total energy or track counts. The information from each subdetector is combined, allowing spatial coincidences between the subdetectors to be identified. The central logic processor also uses signals from the vertex chamber, the jet chamber, the time-of-flight detector, the electromagnetic calorimeter, the hadron calorimeter and the muon chambers. For this analysis, trigger signals were required from both the jet chamber and electromagnetic calorimeter to accept an event.

The jet chamber trigger provides the central trigger processor with information on the number of hits in three regions of the detector (two rings of 12 adjacent wires near the inner radius and one ring near the outer radius), as well as the number of tracks that could be identified in the detector. A track is recognized in the $r-z$ plane if it originates from the interaction region within an adjustable range in z.

The electromagnetic calorimeter trigger is based on comparing analogue sums of energy in defined regions of the calorimeter against a *low* and a *high* energy threshold. The latter threshold is used for direct or *stand-alone* signals while the lower threshold logic allows for spatial coincidences between the electromagnetic calorimeter and the other subdetectors. The thresholds for the total energy in the barrel detector are 4

GeV and 7 GeV, respectively. The trigger operated with nearly 100% efficiency at a rate from the barrel trigger of about 0.1 Hz for the high threshold events and about 12 Hz for the low threshold events.

3.2.7 Online Data Processing

Once the trigger logic has identified an event with potentially interesting physics, the data are read out from each of the subdetectors and transferred to an *event builder* where the full event record is assembled. The event is then passed to a filter processor which performs a fast analysis to provide preliminary event type classification ($q\overline{q}$ pair, lepton pair, etc.). The filter processor is also used to reject events which have been identified as background events (those events which are not physically interesting), which account for approximately 90% of the data selected by the trigger logic. The filter processor writes out the events into 20 Megabyte files which are then released to the online data reconstruction system (ROPE).

The events are processed immediately by the online reconstruction system. The data reconstruction program consists of several subprocessors, one for each subdetector plus others to perform matching between the subdetectors. The quantities measured in the detector are converted into calibrated energies and vector momenta.

3.2.8 Detector Performance

The OPAL detector collected data at LEP phase 1 (at or near the Z^0 pole) from August 1989 to October 1995. Phase 2 began in October 1995 and is still ongoing. During phase 1, 5.1 million Z^0 decays to detectable particles were observed at the OPAL interaction point for a total integrated luminosity of 163 pb^{-1}. The integrated luminosity collected as a function of time at OPAL since 1991 is in shown in Fig-

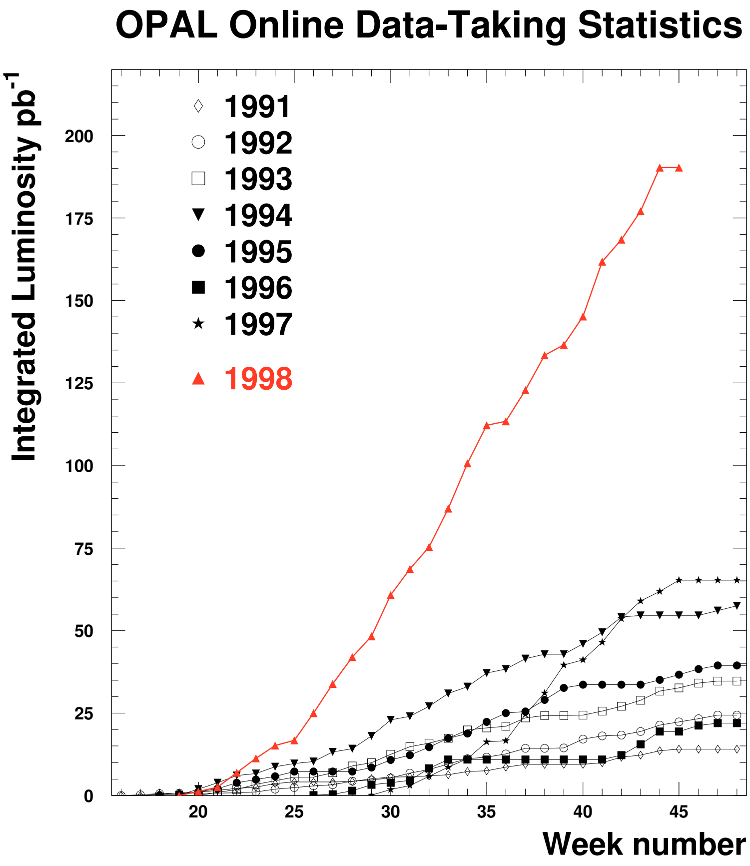

Figure 3.5: The integrated luminosity collected by the OPAL detector as a function of time. The weak number is referenced to the LEP start date each year.

ure 3.5. The analysis reported here studies the $e^+e^- \to \tau^+\tau^-$ events collected at OPAL between 1991 and 1995.

Chapter 4

Particle Identification

This chapter will describe the key aspects of how various particles interact and are identified using the OPAL detector. The first section describes how particles can be identified using the OPAL drift chamber through ionization energy loss. The second section describes the electromagnetic interactions of particles with matter and the properties of electromagnetic showers. Finally, the third section describes the hadronic interactions of particles with matter and presents a study of the hadronic shower profile of various tau decays.

4.1 Ionization Energy Loss

As a charged particle travels through a gas it will lose energy as it interacts with the atomic electrons of the gas. The atomic electrons then undergo one of two processes: excitation or ionization. Excitation occurs when the atomic electron is lifted to a higher energy level while ionization occurs when the atomic electron is ejected from the atom. The total energy loss of the charged particle is given by the Bethe-Bloch formula which approximates the average energy deposition per unit length ($\mathrm{d}E/\mathrm{d}x$) in terms of the particle energy [27, 28]:

$$-\frac{\mathrm{d}E}{\mathrm{d}x} = \frac{4\pi n Z^2 e^4}{m_\mathrm{e} v^2}\left[\ln\left(\frac{2m_\mathrm{e}v^2}{\mathrm{I}(1-\beta^2)}\right) - \beta^2 - \frac{\delta}{2}\right], \tag{4.1}$$

where m_e is the electron mass, Z and v are the charge and the velocity of the particle, $\beta = v/c$, n is the number of electrons per cm^3 in the medium, E is the energy of the particle in MeV, x is the path length measured in g cm^{-2}, I is the mean excitation energy which is approximately $10Z$ eV for absorber materials with $Z > 8$ and δ is the density correction factor.

The energy loss of a particle is measured as it travels through the gas mixture composed of argon (88.2%), methane (9.8%) and isobutane (2.0%) in the Central Jet chamber (CJ). As described in section 3.2.1, the CV, CJ and CZ detectors are all contained in a pressure vessel maintained at a pressure of 4 bar optimised to provide the best combination of dE/dx resolution for particle separation and position and momentum resolution. The choice of this pressure is a compromise between high pressure which maximises the dE/dx particle identification ability and low pressure which minimises multiple scattering.

The charge deposited on each wire is proportional to the energy loss of the particle as it travels through the OPAL jet chamber. These independent energy loss measurements are distributed according to a Landau distribution from which the mean energy loss for each particle can be measured. The resolution of the dE/dx measurement for the OPAL jet chamber has been determined to be [29]

$$\frac{\sigma(\mathrm{d}E/\mathrm{d}x)}{(\mathrm{d}E/\mathrm{d}x)} = \sigma_{159}\left(\frac{159}{\mathrm{N}_{\mathrm{sample}}}\right)^{0.43}, \tag{4.2}$$

where $\mathrm{N}_{\mathrm{sample}}$ is the number of wires in the CJ detector that are used to measure dE/dx and σ_{159} is the resolution obtained when all 159 dE/dx samples are used in the energy loss measurements. Typically the dE/dx resolution is from 3-4%. Note that most tracks do not have 159 dE/dx samples due to the application of quality criteria. Figure 4.1 shows the dependence of dE/dx on momentum for tracks originating from

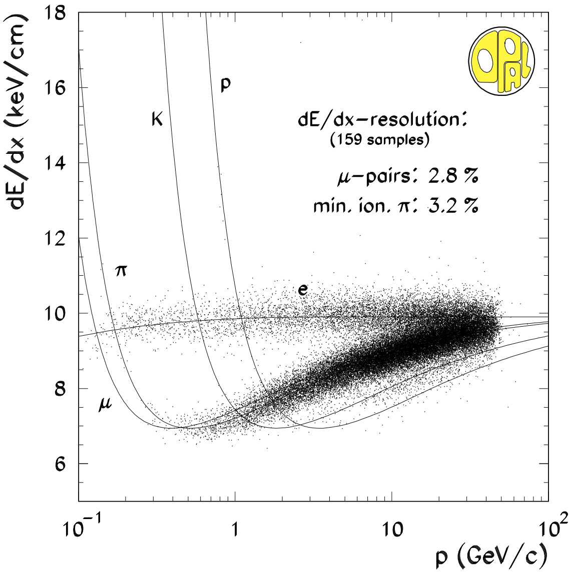

Figure 4.1: The ionization energy loss (dE/dx) as a function of momentum for tracks from τ decays, superimposed on the plot are the theoretical prediction curves for various particle species in the OPAL jet chamber.

various final states of the τ lepton. The points are from the data and the solid lines are predictions based on the energy loss parameterisation.

The energy loss drops rapidly with increasing velocity of the particle, until an ionization minimum occurs at about $\beta = 0.95$. It starts to increase slowly after the minimum because of relativistic effects (*relativistic rise*). At high momenta, the energy loss saturates at what is known as the *Fermi Plateau.*

The particle separation power $S(\sigma)$ versus momentum is shown in Figure 4.2 for pairs of various particle species i and j, such that

$$S(\sigma) = \frac{(\mathrm{d}E/\mathrm{d}x)_i - (\mathrm{d}E/\mathrm{d}x)_j}{\sigma}, \tag{4.3}$$

where σ is the quadratic sum of the uncertainties on the energy loss of the two particle species in question. From Figure 4.2, it is observed that the OPAL jet chamber yields, for example, a pion/kaon separation of at least 2σ for particles with a momentum

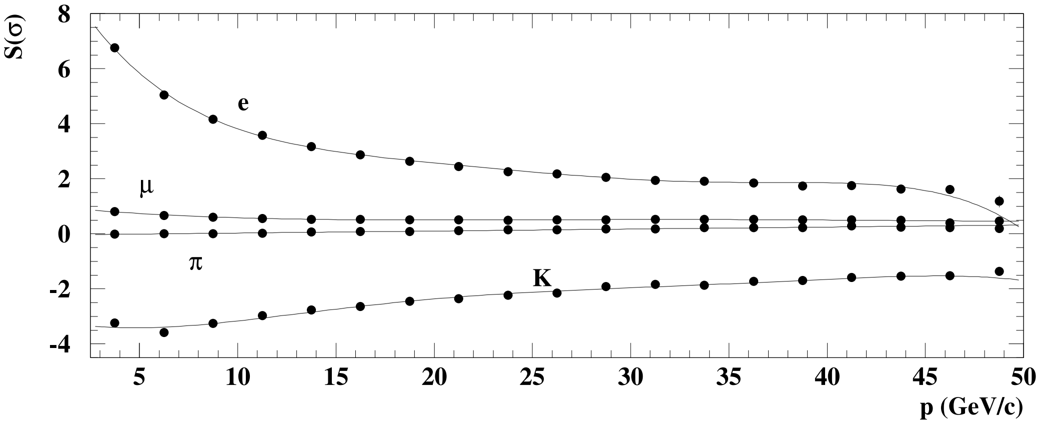

Figure 4.2: The separation from pions in standard deviations for different particle types as a function of momentum.

between approximately 2 and 30 GeV.

The $\mathrm{d}E/\mathrm{d}x$ for a particle species can be converted into two other forms for easy particle identification. First, the $\mathrm{d}E/\mathrm{d}x$ can be normalised such that it has a mean of zero and a width of one. The normalised $\mathrm{d}E/\mathrm{d}x$ ($N(\mathrm{d}E/\mathrm{d}x)$) is defined as

$$N(\mathrm{d}E/\mathrm{d}x) = \frac{\mathrm{d}E/\mathrm{d}x_{\mathrm{measured}} - \mathrm{d}E/\mathrm{d}x_{\mathrm{expected}}}{\sigma_{\mathrm{d}E/\mathrm{d}x}}, \tag{4.4}$$

where $\mathrm{d}E/\mathrm{d}x_{\mathrm{measured}}$ is the measured $\mathrm{d}E/\mathrm{d}x$, $\mathrm{d}E/\mathrm{d}x_{\mathrm{expected}}$ is the expected $\mathrm{d}E/\mathrm{d}x$ for the particle of interest at a known momentum and $\sigma_{\mathrm{d}E/\mathrm{d}x}$ is the $\mathrm{d}E/\mathrm{d}x$ resolution. The normalised $\mathrm{d}E/\mathrm{d}x$ was studied in Appendix B using one-prong tau hadronic decays; corrections were applied where necessary to the ensure that the Monte Carlo modelled the data. Figure 4.3 shows the normalised $\mathrm{d}E/\mathrm{d}x$ for tracks using the hypothesis that the track was a pion. This plot shows the various particle species within the one-prong tau sample. Reasonable separation power is observed between the charged pion and kaon mesons allowing the charged pions and kaons to be separated on a statistical basis.

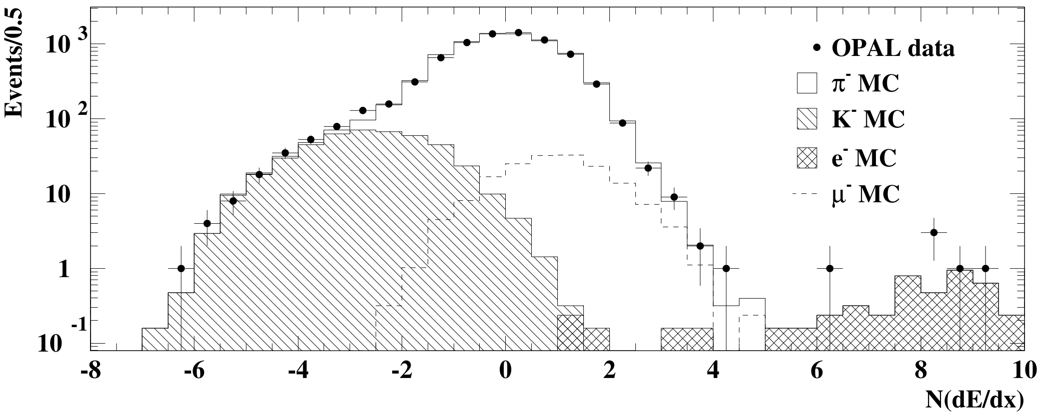

Figure 4.3: The normalized dE/dx (N(dE/dx)) for tau decays into one-prong hadrons with various components indicated on the plot.

The second identification variable is created when the normalised dE/dx for a particle species P is converted into a probability weight, W_P. The weights for a particular particle species are flat between -1 and 1. This analysis uses the dE/dx weights to identify charged particles. The dE/dx weight, W_P, is defined to be the χ^2 probability for one degree of freedom of a track being consistent with a particular particle species and is defined as [30]

$$W_P(X) = \frac{1}{\sqrt{2\pi}} \int_X^{\infty} \mathrm{e}^{-\frac{1}{2}t} dt, \tag{4.5}$$

where $X = (N(\mathrm{d}E/\mathrm{d}x))^2$. The sign of the weight is extracted from the difference $\mathrm{dE/d}x_{\mathrm{measured}} - \mathrm{dE/d}x_{\mathrm{expected}}$, where $\mathrm{dE/d}x_{\mathrm{expected}}$ is the expected value of dE/dx according to the measured momentum of the assumed particle species. Figure 4.4 shows the dE/dx weight W_π assuming that the track comes from a pion for the one-prong tau decays. The hatched part of the plot shows the pion contribution from the Monte Carlo and as expected a pure pion sample has a flat distribution. For more information about the dE/dx calibration, see Appendix B. Note that most of the charged kaons are identified as having a very small probability of being a pion.

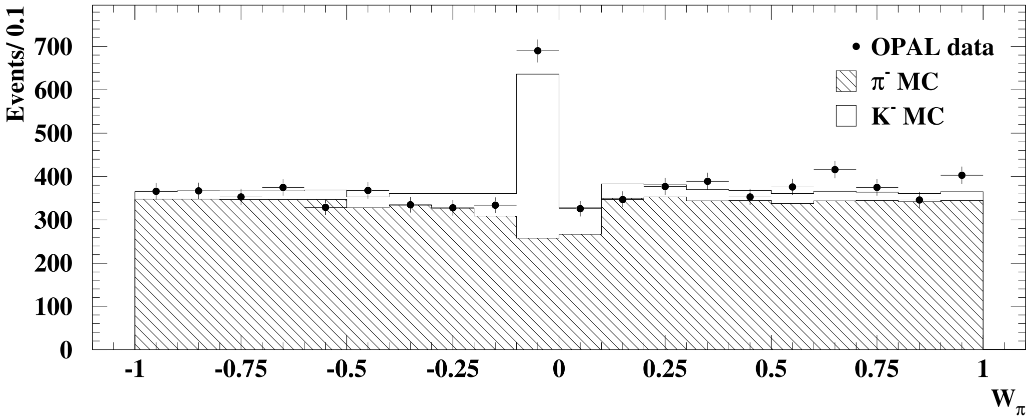

Figure 4.4: The dE/dx weight, W_π, of one-prong tau decays assuming that the track is a pion.

4.2 Electromagnetic Showers

Particles lose energy through both electromagnetic and hadronic interactions with matter. The electromagnetic component of a hadronic shower can be significant if the particle interacts with the detector material creating photons or if the hadronic shower contains π^0 mesons which decay into photons; the resulting photons then initiate an electromagnetic shower. These showers begin at energies above approximately $550/Z$ MeV when electrons lose the majority of their energy by radiating photons via bremsstrahlung, where Z is the atomic number of the medium. If a photon has sufficient energy it may interact with the detector material producing electron-positron pairs. The newly formed electrons and positrons also lose energy by bremsstrahlung, producing photons which continue to undergo further pair production. Therefore while the electromagnetic shower is developing, the number of particles is increasing. Consequently, the average energy of the particles in the shower decreases until it falls below the *critical energy* E_c ($E_c \sim 550/Z$ MeV [31]). At this point the particle multiplication stops because the loss of energy by ionization becomes larger than by bremsstrahlung. At energies below the critical energy, photons interact mainly through Compton scattering and the photoelectric effect.

The lateral spread of an electromagnetic shower is mainly due to the multiple scattering of the electrons that do not radiate but have a large enough energy to travel significant distances from the initial shower axis. The multiple scattering process increasingly influences the lateral spread with decreasing energy of the shower particles causing a gradual widening of the shower. The shower radius is characterised using the natural transverse unit of a shower — the lateral spread of an electron beam of critical energy E_c after traversing a material thickness X_0 [32],

$$R = 2R_m = 2\frac{E_s}{E_c}X_0 \quad \text{and} \quad E_s = 21 \text{ MeV}, \tag{4.6}$$

where R_m is the Molière radius, E_s is the constant appearing in multiple scattering theory [28] and X_0 is the radiation length. A good approximation for the radiation length [31] is given by

$$X_0 \simeq 180\frac{A}{Z^2} \text{ g cm}^{-2}. \tag{4.7}$$

Inserting X_0 and E_c into equation 4.6 gives

$$R_m \simeq 14\frac{A}{Z} \text{ g/cm}^2, \tag{4.8}$$

where the ratio A/Z can be estimated from the composition of the material in question. For the OPAL detector this ratio gives, $A/Z \simeq 2.34$, consequently, R_m is about 32.8 g/cm^2 or 6.0 cm, given that the density of the OPAL lead glass blocks is 5.5 g/cm^3.

The energy loss of the electromagnetic shower in any detector can be parameterised in a material-independent way using the radiation length. The energy loss ΔE *by* *radiation* in length Δx is written as [32],

$$\frac{\Delta E}{\Delta x} = -\frac{E}{X_0} \tag{4.9}$$

where E is in units of GeV and must be greater than 1 GeV. While the high energy part of the electromagnetic shower is governed by equation 4.9, the low energy part of the shower is characterised by the critical energy of the medium. It is defined as the energy loss *by collision* of the electrons (or positrons) of energy E_c in the medium in one radiation length, i.e [31].

$$\frac{\mathrm{d}E}{\mathrm{d}x} = -\frac{E_c}{X_0} \simeq 3\frac{Z}{A}\ \mathrm{MeVcm^2/g}. \tag{4.10}$$

For the OPAL electromagnetic calorimeter, the energy loss by collision is 7.02 MeV cm^2/g or 38.6 MeV/cm.

The depth at which a shower penetrates the medium is also characterised using the critical energy. The median depth of the shower is given by the expression [32],

$$t_{med} = \log\left(\frac{E}{E_c}\right) + a, \quad \text{where } a = \left\{ \begin{array}{ll} 0.4 & \text{for electrons} \\ 1.2 & \text{for photons} \end{array} \right. . \tag{4.11}$$

The median depth is related to the maximum of the shower such that $t_{max} \simeq t_{med} - 1.5$. The longitudinal distribution of the shower allows one to estimate the calorimeter depth needed to contain a fixed fraction of the incident energy, i.e. $L(98\%) \simeq 3t_{med}$. For example, if a 50 GeV electron (photon) is incident on the OPAL electromagnetic calorimeter, then the 98% containment level will be reached if the calorimeter has a depth of $21.4X_0$ ($23.8X_0$). Recall that the OPAL electromagnetic calorimeter is $24.6X_0$ thick with an additional $2X_0$ of material in front of the calorimeter.

To study the energy leakage of electromagnetic showers out of the back of the OPAL electromagnetic calorimeter, two samples of electrons from tau decays with different energy ranges were studied. First, electrons with an incident energy less than 10 GeV were studied and it was observed that approximately 1% of them escaped the electromagnetic calorimeter. The remaining higher energy (10–40 GeV) electrons showed a leakage rate of approximately 3%. This suggests that most electromagnetic showers will be contained within the OPAL electromagnetic calorimeter.

The resolution of the energy measurement of the electromagnetic shower is determined by the fluctuations in the shower propagation. The intrinsic component of the resolution is caused by the fluctuations in the total charged track length. This represents the lower bound on the resolution. Additional components that affect the resolution include the incomplete containment of the showers (energy leakage) and to a lesser extent the transverse leakage, as well as non-uniformity in the signal collection and imperfections in the material.

4.3 Hadronic Showers

Hadronic interactions between a particle and matter are more complex than electromagnetic interactions because there are many more possible reactions involved. An energetic hadron loses its energy in matter through elastic and inelastic scattering with the nuclei of the medium. In an elastic scattering process, the energy of the incident particle changes due to the recoil of the scattering nuclei in the medium, but the nuclear state of the particle remains the same. The fraction f of the incident particle energy transferred to the medium is given by [34],

$$f = \frac{1}{A+1}, \tag{4.12}$$

where A is the nuclear mass of the medium. Consequently, if the nuclei in the material are light, the recoil energy becomes an important factor.

In an inelastic scattering processes, the nuclei and/or incident particle may become excited, break up, or produce additional particles. These may in turn lose their kinetic energy by ionization or initiate new reactions, continuing the process of hadronic shower development. Therefore hadronic showers are characterised by multiparticle production and particle emission by spallation from nuclei.

Spallation proceeds via two processes [33]:

1: Intranuclear cascade: This process occurs when an incoming particle interacts with a nucleon inside the nucleus; the particle may transfer enough energy to the nucleon to cause it to interact with other nucleons. Pions or other mesons are often produced from these interactions, and some of the faster nucleons (p, n) can be emitted with enough energy to cause further intranuclear cascades.

2: Evaporation: The highly excited nucleus remaining from each intranuclear cascade then decays by liberating neutrons, photons and possibly other nucleons, until the excitation energy is smaller than the binding energy (a few MeV per nucleon) of the nucleons. Subsequently, the nucleus decays by emitting γ-rays.

Neutral pions are often produced as secondary mesons in inelastic collisions and charge exchange interactions by charged pions; they decay into two photons with a branching ratio of about 99%. These photons initiate electromagnetic showers. Therefore, hadronic showers contain an electromagnetic component that is generated at the particle level. The effect causes a large variation in the response of calorimeters to hadrons depending on how much of the incident hadron energy is converted into energy observed as an electromagnetic shower.

The typical hadronic shower dimension scales with the nuclear absorption (or interaction) length λ; the mean free path length of a particle before undergoing inelastic nuclear scattering. It is often approximated by [31]

$$\lambda \simeq 35A^{1/3}\mathrm{g\,cm}^{-2}. \tag{4.13}$$

Hadronic showers differ from electromagnetic showers by their longer longitudinal dimension. This effect can be seen by comparing the nuclear absorption length λ, which is proportional to $A^{1/3}$, with the radiation length X_0, which is proportional to A/Z^2. The interaction length of pions and kaons in the OPAL hadronic calorimeter is estimated to be approximately 18 cm. About half the energy in a hadronic shower deposited through ionization is due to fast secondaries. The average transverse momentum of these secondary hadrons is about 350 MeV/c [34]. Thus, a hadronic shower is more spread out than an electromagnetic one. In addition, a hadronic shower can start much deeper in the medium than an electromagnetic shower.

The full incident energy of a hadronic shower may not be detected due to several processes. A sizable amount of the available energy is used to liberate slow neutrons from the nucleus during nuclear evaporation, this effect is known as *binding energy loss*. Some of this lost energy may be recovered when neutrons are captured by other nuclei.

Slow charged pions produced in the nuclear reactions may also contribute to the undetectable energy. The low-energy charged pions decay into muons and muon neutrinos via the weak interaction. The muon only ionizes minimally and nearly always escapes due to its long lifetime of 2.2 μs. The neutrino being a neutral lepton does not interact in the calorimeters. Finally, the ionization from the slow nucleon fragments is usually so dense that it can saturate the active medium or fail to leave the absorber material, and thus does not contribute efficiently to the energy measurement in the calorimeters.

4.3.1 Hadron Shower Profile

The longitudinal depth of a hadronic shower is very important in determining the size of a hadronic calorimeter and in determining if the calorimeter can contain the energy from the hadronic shower. The longitudinal depth profile of the OPAL hadron calorimeter is investigated using three τ decay channels and two single hadron Monte Carlo simulations. The three tau decays examined in this analysis included the $\tau^- \to \pi^- \nu_\tau$, $\tau^- \to \rho^- \nu_\tau$ and $\tau^- \to X^- \mathrm{K}^0_\mathrm{L} \nu_\tau$ decay modes. The two single hadron Monte Carlo samples are created in which charged pions and K^0_L mesons are simulated interacting with the OPAL detector.

The energy of the hadronic showers is determined by summing over the energy of the individual clusters in the hadronic calorimeter within a 35° cone around the direction of the τ. The longitudinal profile mapping (depth) is obtained by summing over the number of hits in each layer by counting the strip signals within the cone, until a prescribed level of containment is reached. Longitudinal energy deposition profiles are characterised by a sudden onset at the first interaction point followed by a more gradual development with a maximum at a depth [3, p. 159]

$$\frac{x}{\lambda} \simeq 0.2 \ln E + 0.7, \tag{4.14}$$

where E is the energy in the shower in GeV.

The depth profiles should be identical for any hadron at the same incident energy. To test this hypothesis, a Monte Carlo sample of single charged pions and single K^0_L mesons were generated at an incident energy of 10 GeV and passed through the OPAL detector simulation routines. Figure 4.5 shows the longitudinal depth at a containment level of 80 and 95% for this Monte Carlo. As expected, the shower profiles are very similar. Figure 4.6 shows the longitudinal hadronic shower development for

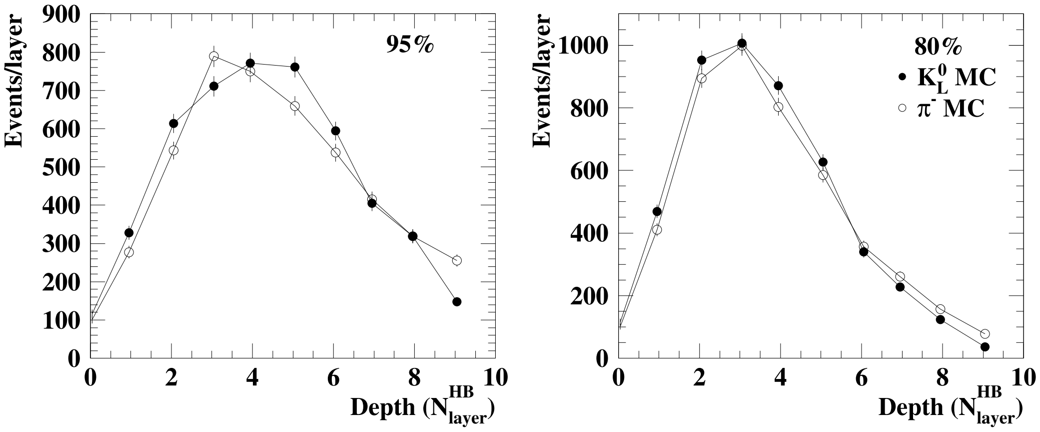

Figure 4.5: The longitudinal shower depth for the Monte Carlo sample of single charged pion mesons and $\mathrm{K_L^0}$ mesons at an incident energy of 10 GeV at the 95% and 80% shower containment levels.

tau decays into final states containing pion, rho and $X^-\mathrm{K_L^0}$ mesons. The showers are fully contained at the 80% containment level while some of the shower energy may be lost at the 95% containment level. Small differences in the shower shapes for the three final states are due to biases introduced by the different algorithms used to select the three different tau decays, for example, all $X^-\mathrm{K_L^0}$ final states must have a minimum energy in the hadron calorimeter of 7.5 GeV, while no such requirement is imposed on the other two final states.

On average, most tau hadronic showers are contained within the OPAL hadron calorimeter; the average shower penetrates about 3.2 interaction lengths ($\sim$ 60 cm). For very energetic particles in the hadron calorimeter, the longitudinal measurement may not be accurate because the OPAL hadron calorimeter depth is only 4.77 interaction lengths. Note that the combined electromagnetic and hadronic calorimeters have a depth of approximately 7 interaction lengths. It can be shown [3, p. 159] that for hadrons with an incident energy greater than 50 GeV, approximately 6 interaction

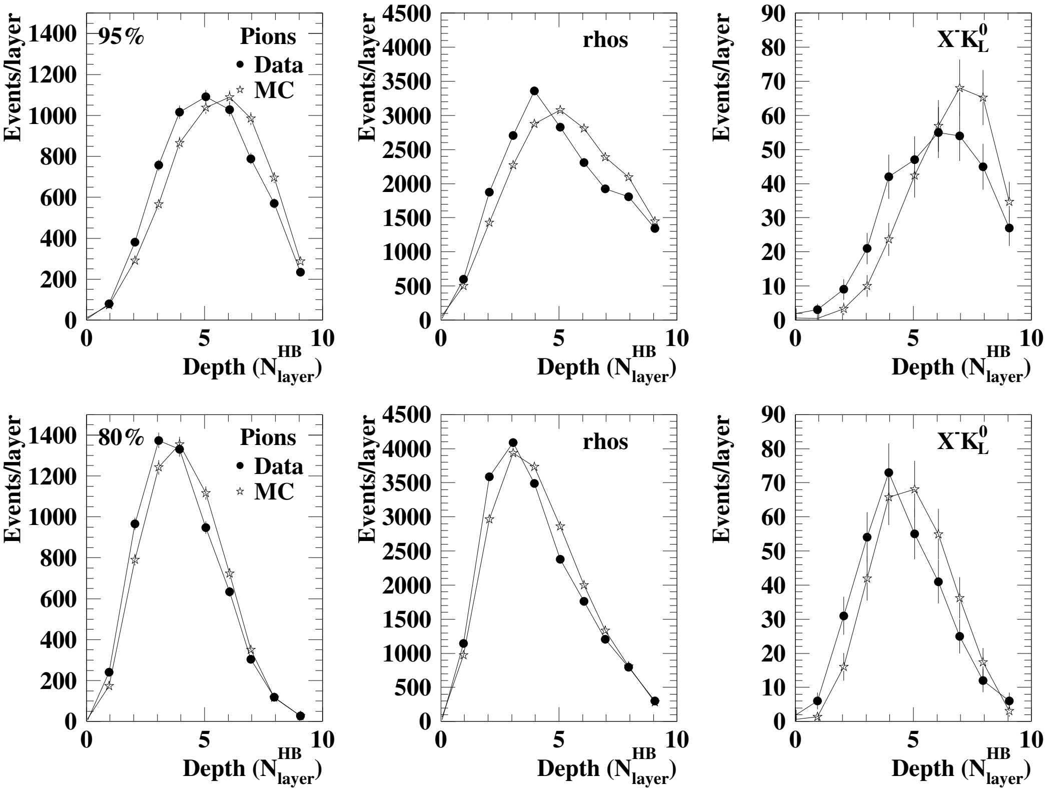

Figure 4.6: The layer in which the shower is stopped is plotted for the 95% (top plots) and 80% (bottom plots) containment levels. The shower profiles are different due to the biases introduced in the selection of the various τ decays. The data are the points and the stars are the MC.

lengths are required for 95% energy containment. It will be shown in Chapter 7 that this leakage of energy out of the back of the hadron calorimeter has no significant impact on the calibration of the hadronic energy.

Chapter 5

Tau-Pair Selection

This chapter will present the selection of the tau events used in this analysis. The first section describes the OPAL data as well as the Monte Carlo simulated data samples that were used to estimate efficiencies and backgrounds in the data sample. The second section discusses the selection of tau-pair decays of the Z^0 from the full data set.

5.1 Event Samples

5.1.1 OPAL Data Sample

The data used in this analysis were taken during the 1991-1995 running periods of LEP. The integrated luminosity per year is given in Table 5.1. Approximately 89.6% of the data was collected at the Z^0 peak centre-of-mass energy ($E_{\mathrm{CM}} = 91.2$ GeV), 4.4% are approximately 2 GeV below the Z^0 peak and the remaining 6.0% are approximately 2 GeV above the Z^0 peak. The OPAL detector information is recorded for each subdetector when the trigger identifies some activity that coincides with the beam crossing [21]. The raw data are processed in real time so that background from beam-gas interactions and cosmic rays are reduced. The data are then passed through ROPE [35] which converts the raw information (*eg.* drift times) to physical quantities (*eg.* tracks).

Year	Integrated Luminosity
1991	13 pb^{-1}
1992	24 pb^{-1}
1993	34 pb^{-1}
1994	59 pb^{-1}
1995	33 pb^{-1}
Total	163 pb^{-1}

Table 5.1: Integrated luminosity per year.

	CV	CJ	TB	PB	EB	EE	HS	HT	MB
detector	3	3	3	2	3	3	3	2	3
trigger	-	2	-	-	2	3	-	-	-

Table 5.2: Detector and Trigger Status Requirements.

It is important that only reliably measured quantities be used for the selection criteria. Therefore the subdetectors used to make the measurements are required to be in good running order during the data taking period. There are four status levels defined for each subdetector: 0 indicates that the subdetector status is unknown, 1 indicates that it is off, 2 means that the detector is partly on, and 3 indicates the detector is fully on. Table 5.2 shows the minimum levels required for each detector and trigger used in this analysis; if there is no status level indicated then no requirement was placed on that particular detector or trigger.

5.1.2 Monte Carlo Event Sample

Monte Carlo simulated data were used to estimate the selection efficiency and backgrounds in this analysis. The primary Monte Carlo event sample of four-vector quantities for the reaction $\mathrm{e}^+\mathrm{e}^- \to \tau^+\tau^-$ were generated using the KORALZ [36] simulation program. The Monte Carlo samples used for the $\mathrm{e}^+\mathrm{e}^-$ processes discussed in this

Interaction	MC run	Generator	Luminosity (pb^{-1})
$e^+e^- \to \tau^+\tau^-$	1520	KORALZ [36]	405.1
	1536	KORALZ	253.1
	1560	KORALZ	539.5
	1565	KORALZ	337.8
$e^+e^- \to \mu^+\mu^-$	1620	KORALZ	404.3
	1636	KORALZ	253.1
$e^+e^- \to e^+e^-$	1320	BABAMC [40]	151
	1335	BHWIDE [41]	72.2
$e^+e^- \to q\overline{q}$	2291-2292	JETSET [42]	60.8
	2790-2793	JETSET	121.6
$e^+e^- \to (e^+e^-)\mu^+\mu^-$	1716	VERMASEREN [43]	461.7
	1745	VERMASEREN	456.0
$e^+e^- \to (e^+e^-)e^+e^-$	1717	VERMASEREN	392.5
	1746	VERMASEREN	392.5
$e^+e^- \to (e^+e^-)\tau^+\tau^-$	1744	VERMASEREN	678

Table 5.3: The Monte Carlo samples used in this analysis to model τ decays and non-τ backgrounds in the τ event sample.

dissertation are shown in Table 5.3.

KORALZ simulates tau-pair production and decays at the Z^0 centre-of-mass energy, including higher order corrections. Decays of the taus produced by KORALZ were simulated using the Tauola [37] program. The branching ratios used in KORALZ were the world averages at the time that the Monte Carlo sample was created, however the selection method does not rely on their particular values.

The four vectors of the particles created by the various generators were processed by the OPAL detector simulation program, GOPAL [38], which uses the program GEANT [39] to track the particles through the volume of the OPAL detector. GOPAL produces output in an identical format (with the addition of the initial four vectors) as the data that are extracted from the OPAL detector. The Monte Carlo samples are then passed through the same reconstruction procedure as the real data. Comparisons between Monte Carlo and data of the distributions of physics quantities are used to ensure the accuracy of the Monte Carlo modeling, and corrections are applied to the Monte Carlo distributions where necessary. These corrections are discussed in the following chapters.

5.1.3 Monte Carlo Modelling

Experimental evidence suggests that when the τ decays into a hadronic final state it does so via a single particle or resonance ($\tau^- \to X^- \nu_\tau$). The particle X^- could be a long lived particle, such as a π^- or K^-, or it could be a short lived particle (resonance) such as the $\rho(770)^-$ or $\mathrm{K}^*(892)^-$. The Tauola generator uses this information when generating the τ decays. If such information is not known, the decays are generated using phase space distributions. New information on the decays into final states with kaons has recently become available and this section describes how this new information has been incorporated into Tauola. Table 5.4 shows the tau decay final states that are detected in this analysis. The production processes are also shown for each final state.

The $\tau^- \to \pi^- \overline{\mathrm{K}}^0 \nu_\tau$ decay has the largest branching ratio of the decay modes selected in this analysis. The $\pi^- \overline{\mathrm{K}}^0$ final state mesons are generated via the $\mathrm{K}^*(892)$ resonance by Tauola. This final state is well understood and no additional Monte Carlo was made. The $\tau^- \to \mathrm{K}^- \mathrm{K}^0 \nu_\tau$ decay mode was generated by Tauola using phase space only.

The $\tau^- \to \pi^- \overline{\mathrm{K}}^0 \pi^0 \nu_\tau$ decay mode was generated by Tauola through the $\mathrm{K}_1(1400)$

Final state	Production Process
$\tau^- \to \pi^- \overline{\mathrm{K}}^0 \nu_\tau$	K*(892)
$\tau^- \to \mathrm{K}^- \mathrm{K}^0 \nu_\tau$	phase space
$\tau^- \to \pi^- \overline{\mathrm{K}}^0 \pi^0 \nu_\tau$	$\mathrm{K}_1(1270)$
	$\mathrm{K}_1(1400)$
$\tau^- \to \mathrm{K}^- \mathrm{K}^0 \pi^0 \nu_\tau$	$\mathrm{a}_1(1260)$
	$\rho(1700)$
$\tau^- \to \pi^- \overline{\mathrm{K}}^0 \pi^0 \pi^0 \nu_\tau$	phase space
$\tau^- \to \mathrm{K}^- \mathrm{K}^0 \pi^0 \pi^0 \nu_\tau$	phase space

Table 5.4: The final states observed in this analysis are shown in the first column. The intermediate resonances that are used by the Monte Carlo to simulate these decays are shown in the second column. For some decays the final state is created using phase space only, because the intermediate structure of these decays is not well understood.

intermediate resonance using two decay chains:

$$\tau^- \to \mathrm{K}_1(1400)^- \nu_\tau \to (\mathrm{K}^*(892)\pi)^- \nu_\tau \to \pi^- \overline{\mathrm{K}}^0 \pi^0 \nu_\tau$$

$$\tau^- \to \mathrm{K}_1(1400)^- \nu_\tau \to (\rho(770)\mathrm{K})^- \nu_\tau \to \pi^- \overline{\mathrm{K}}^0 \pi^0 \nu_\tau.$$

Several recent analyses and theoretical studies have indicated that the $\tau^- \to \pi^- \overline{\mathrm{K}}^0 \pi^0 \nu_\tau$ decay can also proceed via the $\mathrm{K}_1(1270)$ resonance [13, 44, 45]. The $\mathrm{K}_1(1270)$ meson decays primarily to $\mathrm{K}^*(892)\pi$, $\mathrm{K}_0^*(1430)\pi$ and $\rho(770)\mathrm{K}$, which in turn decay some of the time to final states including neutral kaons. The $\mathrm{K}_1(1270)$ meson can decay into meson pairs heavier than itself, i.e $\rho(770)\mathrm{K}$, due to its broad width which is estimated to be between 50 and 200 MeV [3, p. 474]. The possible branching ratios of the $\mathrm{K}_1(1270)$ meson are also taken from [3, p. 474]. The various decay possibilities will give different momenta and energy spectra of the final decay products, consequently affecting the selection efficiency of the $\tau^- \to \pi^- \overline{\mathrm{K}}^0 \pi^0 \nu_\tau$ decay. To examine these differences, a modified version of Tauola created by S. Towers [44, 46] was used to generate the following decays that include the $\mathrm{K}_1(1270)$ resonance:

$$\begin{aligned}
\tau^- &\rightarrow \mathrm{K}_1(1270)^-\nu_\tau \rightarrow (\mathrm{K}^*(892)\pi)^-\nu_\tau \rightarrow \pi^-\overline{\mathrm{K}}^0\pi^0\nu_\tau \\
\tau^- &\rightarrow \mathrm{K}_1(1270)^-\nu_\tau \rightarrow (\mathrm{K}_0^*(1430)\pi)^-\nu_\tau \rightarrow \pi^-\overline{\mathrm{K}}^0\pi^0\nu_\tau \\
\tau^- &\rightarrow \mathrm{K}_1(1270)^-\nu_\tau \rightarrow (\rho(770)\mathrm{K})^-\nu_\tau \rightarrow \pi^-\overline{\mathrm{K}}^0\pi^0\nu_\tau.
\end{aligned}$$

Also, an additional sample of $\tau^- \rightarrow \pi^-\overline{\mathrm{K}}^0\pi^0\nu_\tau$ decays was generated in which the $\mathrm{K}_1(1400)$ resonance decays only to $\mathrm{K}^*(892)\pi$, since experimental evidence indicates that this decay dominates over the $\rho(770)\mathrm{K}$ and $\mathrm{K}_0^*(1430)\pi$ modes [13].

The $\tau^- \rightarrow \mathrm{K}^-\mathrm{K}^0\pi^0\nu_\tau$ decay is generated in Tauola through a mixture of the $\mathrm{a}_1(1260)$ and $\rho(1700)$ intermediate resonances:

$$\begin{aligned}
\tau^- &\rightarrow \mathrm{a}_1(1260)^-\nu_\tau \rightarrow (\mathrm{K}^*(892)\pi)^-\nu_\tau \rightarrow \mathrm{K}^-\mathrm{K}^0\pi^0\nu_\tau \\
\tau^- &\rightarrow \rho(1700)^-\nu_\tau \rightarrow (\mathrm{K}^*(892)\pi)^-\nu_\tau \rightarrow \mathrm{K}^-\mathrm{K}^0\pi^0\nu_\tau.
\end{aligned}$$

Special samples of Monte Carlo were generated separately for each of these decay modes [44, 46].

In addition, special Monte Carlo samples were generated for the $\overline{\mathrm{K}}^0\pi^-\pi^0\pi^0\nu_\tau$ and $\mathrm{K}^0\mathrm{K}^-\pi^0\pi^0\nu_\tau$ decays which were not included in Tauola [44, 46]. Since the intermediate structure of these decays is not well understood theoretically and experimental information is sparse, these decays were generated through phase space only.

5.2 Tau Selection

At LEP, electron and positron beams collide and form a Z^0 boson which in turn can decay into lepton-antilepton, neutrino-antineutrino or quark-antiquark pairs;[1] the quark pairs give rise to multihadronic events.[2] This section will describe the analysis

---

[1] Note that the Z^0 is too light to decay into $t\bar{t}$ pairs.

[2] Multihadronic events contain several hadrons which are created through hadronization of the quark-antiquark pair.

	Requirements	Variable Description
Track definition	$N_{CJ}^{hits} \geq 20$ hits	N_{CJ}^{hits}: number of hits in the jet chamber.
	$P_T \geq 0.1$ GeV	P_T: momentum transverse to the beam direction.
	$\lvert d_0 \rvert \leq 2$ cm	$\lvert d_0 \rvert$: point of closest approach of the track to the interaction point in the $x - y$ plane.
	$\lvert z_0 \rvert \leq 75$ cm	$\lvert z_0 \rvert$: point of closest approach of the track to the interaction point in the z-direction.
	$R_{min} \leq 75$ cm	R_{min}: radius of the first jet chamber hit.
ECAL cluster definition	$N_{blocks} \geq 1$	N_{blocks}: number of ECAL calorimeter blocks in the cluster.
	$E_{clusters} \geq 0.1$ GeV	$E_{clusters}$: total ECAL energy in the cluster.

Table 5.5: Good track and cluster definitions. Those tracks and clusters that satisfy the inequalities are accepted.

that is used to select the $e^+e^- \to Z^0 \to \tau^+\tau^-$ events from the total event sample. At LEP, the Z^0 boson decays at rest in the laboratory frame producing pairs of τ leptons that have equal and opposite momenta and hence appear to be back-to-back. The τ leptons are highly relativistic ($\beta = 0.9992$) and have a lifetime of only 290.0 ± 1.2 fs [3, p. 286], consequently only the τ decay products are seen and they are highly collimated in a narrow cone about the τ direction of motion.

The charged decay products produce tracks in the inner tracking detectors while both charged and neutral decay products can deposit energy in the electromagnetic and possibly the hadronic calorimeters. Figure 5.1 shows a typical tau decay. Tracks and clusters must pass several requirements to ensure that they are not from cosmic rays or beam-gas interactions. These criteria are shown in Table 5.5.

Complete details of the tau selection algorithm are described in references [47,48] and are outlined in Tables 5.6 and 5.7. Each $e^+e^- \to Z^0 \to \tau^+\tau^-$ event is subjected to a jet finding algorithm, where a *jet* is defined to be a collimated concentration of

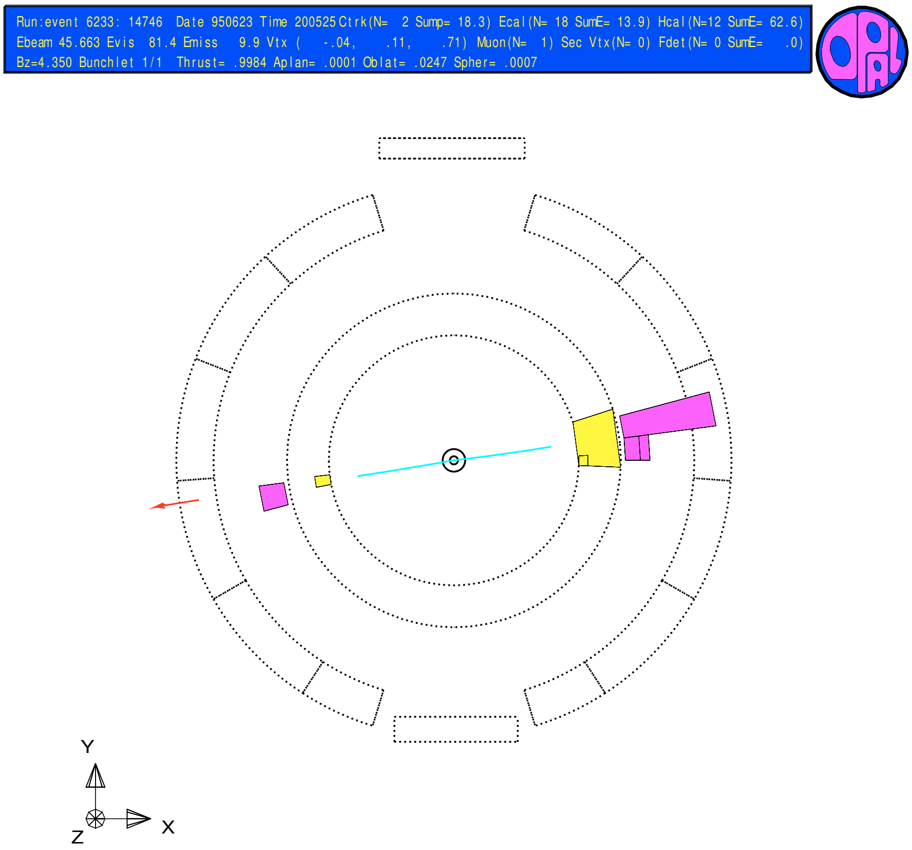

```
Run:event 6233: 14746  Date 950623 Time 200525 Ctrk(N=  2 Sump= 18.3) Ecal(N= 18 SumE= 13.9) Hcal(N=12 SumE= 62.6)
Ebeam 45.663 Evis  81.4 Emiss   9.9 Vtx (   -.04,     .11,     .71) Muon(N=  1) Sec Vtx(N= 0) Fdet(N= 0 SumE=   .0)
Bz=4.350 Bunchlet 1/1  Thrust= .9984 Aplan= .0001 Oblat= .0247 Spher= .0007
```

Figure 5.1: A typical OPAL event, showing two back-to-back τ jets. The view is along the beam direction, showing the transverse plane. The concentric rings correspond to the outer edges of the beam pipe, vertex chamber, jet chamber, electromagnetic calorimeter, hadron calorimeter and muon chambers. The lines in the vertex and jet chambers represent the tracks. The rectangles in the calorimeters represent energy deposits with the rectangle height being proportional to the amount of energy deposited, while the arrow indicates that muon chambers were hit.

activity in the detector caused by the passage of energetic particles. Typical $e^+e^- \to Z^0 \to \tau^+\tau^-$ events produce two jets, where the jets are the τ leptons. The jet direction is initially defined to be the highest energy good track or electromagnetic cluster. The next highest energy good track or cluster within a 35° cone is added to the first track, and the jet direction is redefined by the vector sum. The second step is repeated until there are no more tracks or clusters that fall within a 35° cone.

	Requirements	Variable Description
Good event	$\mathrm{N}_{\mathrm{jet}} = 2$	$\mathrm{N}_{\mathrm{jet}}$: number of jets satisfying the E_{jet} requirement.
	$\overline{\vert\cos\theta\vert} < 0.68$	$\overline{\vert\cos\theta\vert}$: average value of $\vert\cos\theta\vert$ for the 2 jets.
	$E_{\mathrm{jet}} \geq 0.01 E_{\mathrm{beam}}$	E_{jet}: total track and cluster energy in the jet. E_{beam}: the LEP beam energy.
$\mathrm{e}^+\mathrm{e}^- \to \mathrm{q}\overline{\mathrm{q}}$ rejection	$2 \leq \mathrm{N}_{\mathrm{track}} \leq 6$	$\mathrm{N}_{\mathrm{track}}$: number of good tracks in the τ-pair event.
	$\mathrm{N}_{\mathrm{clusters}} \leq 10$	$\mathrm{N}_{\mathrm{clusters}}$: number of good clusters in the τ-pair event.
$\mathrm{e}^+\mathrm{e}^- \to \mathrm{e}^+\mathrm{e}^-$ rejection	$\sum E_{\mathrm{cluster}} \leq 0.8 E_{\mathrm{CM}}$ or $\sum E_{\mathrm{cluster}} + 0.3 \sum E_{\mathrm{track}} \leq E_{\mathrm{CM}}$	E_{cluster}: energy of ECAL clusters in event. $E_{\mathrm{CM}} = 2E_{\mathrm{beam}}$ E_{track}: energy of charged tracks in event.
$\mathrm{e}^+\mathrm{e}^- \to \mu^+\mu^-$ rejection	$\sum_{\mathrm{jets}}(E^{\mathrm{total}}_{\mathrm{cluster}} + E_{\mathrm{track}}) \leq 0.6 E_{\mathrm{CM}}$ and both jets are muons.	
	A jet is a muon if one of the following is true:	
	$\mathrm{N}^{\mathrm{MUON}}_{\mathrm{layers}} \geq 2$	$\mathrm{N}^{\mathrm{MUON}}_{\mathrm{layers}}$: total layers hit in the barrel or endcap muon detector.
	$E^{\mathrm{charged}}_{\mathrm{cluster}} < 2$ GeV	$E^{\mathrm{charged}}_{\mathrm{cluster}}$: energy of the ECAL cluster associated to the track.
	$\mathrm{N}^{\mathrm{HB}}_{\mathrm{layers}} \geq 4$ $\mathrm{N}^{\mathrm{HCAL}}_{\mathrm{outer\,3\,layers}} \geq 1$ and $\mathrm{N}^{\mathrm{HCAL}}_{\mathrm{hits/layers}} < 2$	$\mathrm{N}^{\mathrm{HB}}_{\mathrm{layers}}$: number of HCAL layers with signals associated to the track. $\mathrm{N}^{\mathrm{HCAL}}_{\mathrm{outer\,3\,layers}}$: number of signals in the 3 outer HCAL layers. $\mathrm{N}^{\mathrm{HCAL}}_{\mathrm{hits/layers}}$: number of HCAL hits per layer for the jet.

Table 5.6: Tau-pair selection requirements. The events are accepted if they satisfy the listed conditions.

	Requirements	Variable Description
Two-photon rejection	$\theta_{\text{acol}} \leq 15^\circ$	θ_{acol}: the supplement of the angle between the 2 jets in the τ pair event.
	$E_{\text{vis}} \geq 0.03 E_{\text{CM}}$	$E_{\text{vis}} = \sum_{cone} \text{Max}(E_{\text{cluster}}, E_{\text{track}})$
	If $E_{\text{vis}} \leq 0.20 E_{\text{CM}}$ then	
	$\text{P}_\text{T}(\text{cluster}) > 2.0$ GeV or $\text{P}_\text{T}(\text{track}) > 2.0$ GeV	$\text{P}_\text{T}(\text{cluster})$: sum of ECAL energy in the event. $\text{P}_\text{T}(\text{track})$: scalar sum of track momenta in the event.
Cosmic ray rejection	$\lvert d_0 \rvert_{\text{min}} \leq 5$ mm	$\lvert d_0 \rvert_{\text{min}}$: minimum d_0 for all tracks in the event.
	$\lvert z_0 \rvert_{\text{min}} \leq 20$ cm	$\lvert z_0 \rvert_{\text{min}}$: minimum z_0 for all tracks in the event.
	$\lvert z_0 \rvert_{\text{ave}} \leq 20$ cm	$\lvert z_0 \rvert_{\text{ave}}$: average z_0 for all tracks in the event.
	$\lvert t_{\text{meas}} - t_{\text{exp}} \rvert \leq 10$ ns	t_{meas} and t_{exp}: measured and expected TOF assuming the event is created at the origin.
	If $\lvert \phi_i - \phi_j \rvert \geq 165^\circ$ then reject the event if $\lvert t_i - t_j \rvert \geq 10$ ns.	

Table 5.7: Tau-pair selection requirements (continued). The events are accepted if they satisfy the listed conditions.

The tau-pair selection begins, by selecting candidates that contain exactly two jets, each with at least one charged track and with a total track and cluster energy that exceeds 1% of the beam energy. The average value of $|\cos\theta|$ for the two charged jets must satisfy $\overline{|\cos\theta|} < 0.68$ to avoid the interface region between the barrel and endcap of the lead-glass calorimeter, thus restricting the selection to the barrel.

Background events from the Z^0 decays involving quark-antiquark ($q\overline{q}$), e^+e^- or $\mu^+\mu^-$ final states must be removed from the tau-pair sample. The requirements are:

- Multihadronic events, $\text{e}^+\text{e}^- \to q\overline{q}$ are reduced by limiting the number of tracks and clusters in the event. It is required that the number of good charged tracks in the event be between two and six and that the number of good ECAL clusters be no more than ten.

- Electron-pair final states, $e^+e^- \rightarrow e^+e^-$, can be identified by the presence of two high-momentum, back-to-back charged particles with the full centre-of-mass energy (E_{CM}) deposited in the electromagnetic calorimeter. This background can be reduced by requiring tau-pair candidates to satisfy either $\sum E_{\mathrm{cluster}} \leq 0.8 E_{\mathrm{CM}}$ or $\sum E_{\mathrm{cluster}} + 0.3 \sum E_{\mathrm{track}} \leq E_{\mathrm{CM}}$, where E_{cluster} is the total energy in the ECAL and E_{track} is the total energy of the charged tracks in the event.

- Muon-pair final states, $e^+e^- \rightarrow \mu^+\mu^-$, can be identified by the presence of two high-momentum, back-to-back charged particles but with very little energy deposited in the electromagnetic calorimeter. These events are removed by matching activity in the muon chambers or hadronic calorimeter with tracks in the jet chamber, and then requiring that the total momentum deposited in the jet chamber plus the total energy deposited in the ECAL is less than $0.6 E_{\mathrm{CM}}$.

In addition to the background from two fermion events, two-photon events, $e^+e^- \rightarrow (e^+e^-)X$, where $X = e^+e^-$, $\mu^+\mu^-$, $\tau^+\tau^-$, $q\overline{q}$, must also be removed. Two photon events contain a final state electron and positron that escape undetected at small angles. These backgrounds are not significant because they lack the enhancement to the cross-section from the Z^0 resonance and because the visible energy (the sum of the charged track and ECAL cluster energies) of the two-photon system is in general much smaller than that from a tau-pair event. In addition, the detected particles tend to have a large acollinearity[3] angle with respect to each other. These events are rejected by requiring the acollinearity to be less than 15°, and the visible energy E_{vis}

---

[3] The acollinearity angle is the supplement of the angle between the two jets.

Background	Contamination
$e^+e^- \rightarrow e^+e^-$	0.0041 ± 0.0007
$e^+e^- \rightarrow \mu^+\mu^-$	0.0072 ± 0.0005
$e^+e^- \rightarrow q\overline{q}$	0.0028 ± 0.0004
$e^+e^- \rightarrow (e^+e^-)e^+e^-$	0.0007 ± 0.0002
$e^+e^- \rightarrow (e^+e^-)\mu^+\mu^-$	0.0008 ± 0.0002
Total	0.0156 ± 0.0010

Table 5.8: The fraction of the non-tau background in the tau-pair sample [49].

to be less than 3% of the centre-of-mass energy. The visible energy is the maximum of either the jet energy measured in the ECAL, or the jet energy in the jet chamber. Finally, if $E_{vis} \leq 0.20 E_{CM}$, then the event must have energy greater than 2.0 GeV deposited in either the ECAL or the jet chamber for it to be rejected.

The final background contamination of the tau-pair sample that was considered comes from cosmic rays. These events are removed with simple requirements on the time-of-flight detector and on the location of the primary event vertex.

The tau-pair selection applied to all data between 1991 and 1995 yielded 201850 individual taus. To ensure consistent comparisons between the Monte Carlo and the data, the Monte Carlo was also passed through the same selection as for the data. Studies of this selection using the Monte Carlo give a tau-pair selection efficiency of $54.3 \pm 0.1\%$, which corresponds to an efficiency of 93% within the geometrical acceptance of the detector. The study of the background contamination in the tau-pair sample was made in another analysis [49] using the same tau selection as this work; the background fraction was estimated to be 0.0156 ± 0.0010. The results are summarised in Table 5.8.

Chapter 6

Neutral Kaon Selection

This chapter will describe the selection of the $\tau^- \to X^- \mathrm{K}^0_\mathrm{L} \nu_\tau$ decay. The first section will describe the selection of the $\tau^- \to X^- \mathrm{K}^0_\mathrm{L} \nu_\tau$ decays, where X^- includes a charged hadron possibly accompanied by any number of neutral hadrons (*eg.* π^0 or another K^0). The second section describes the exclusive selections. First, the identity of the charged hadron is determined and secondly, the decays that contain a charged pion are passed through an additional selection which separates out the decays that contain a π^0 meson.

6.1 Selection of $\tau^- \to X^- \mathrm{K}^0_\mathrm{L} \nu_\tau$ decays

The lifetime of the K^0_L is such that it will not decay in the OPAL detector, instead it will interact with the material in the electromagnetic and hadronic calorimeters. The momentum of the charged hadron present in the decay can be measured using the track curvature in the jet chamber while both the charged hadron combination, X^-, and the K^0_L will deposit energy in the hadron calorimeter. Consequently, the selection used in this analysis looks for a significant excess of energy in the hadron calorimeter compared to the momentum of the charged hadron determined from the curvature of the track.

The $\tau^- \to X^- \mathrm{K}^0_\mathrm{L} \nu_\tau$ selection requirements used in this analysis are listed below and a discussion of each requirement will follow:

- $\Rightarrow$ Only one charged track is allowed in the jet chamber.
- $\Rightarrow$ The momentum (p) of the charged track divided by the beam energy (E_beam) must be less than 0.5.
- $\Rightarrow$ No secondary vertices are allowed in the jet.
- $\Rightarrow$ The energy, E_HB, measured in the hadron calorimeter must be larger than 7.5 GeV.
- $\Rightarrow$ The significance factor S_HB must be greater than 2.0.

Each decay was required to have only one track pointing towards the primary vertex that satisfies the track requirements given in Section 5.2 and has a momentum divided by the beam energy (p/E_Beam) less than 0.5. This requirement removes high momentum pion decays from the data sample. Figure 6.1(a) shows p/E_Beam for the decays after all the other selection requirements (except S_HB) have been applied.

In addition, some jets may still contain tracks that have failed the good track requirements. These additional tracks may be from photon conversions or τ decays that have a K^0_S in the final state, where the K^0_S decays to a $\pi^+\pi^-$ pair. Photon conversions and $\tau^- \to X^- \mathrm{K}^0_\mathrm{S} \nu_\tau$ decays are identified if a pair of oppositely charged tracks form a secondary vertex in the $r - \phi$ plane of the jet chamber [50]. If a jet contains one of these secondary vertices, then it is rejected. Approximately 5% of the τ decays are removed by this requirement.

In order to ensure that the decay has a well-measured energy deposition in the hadron calorimeter and to reduce leptonic background, it was required that there be

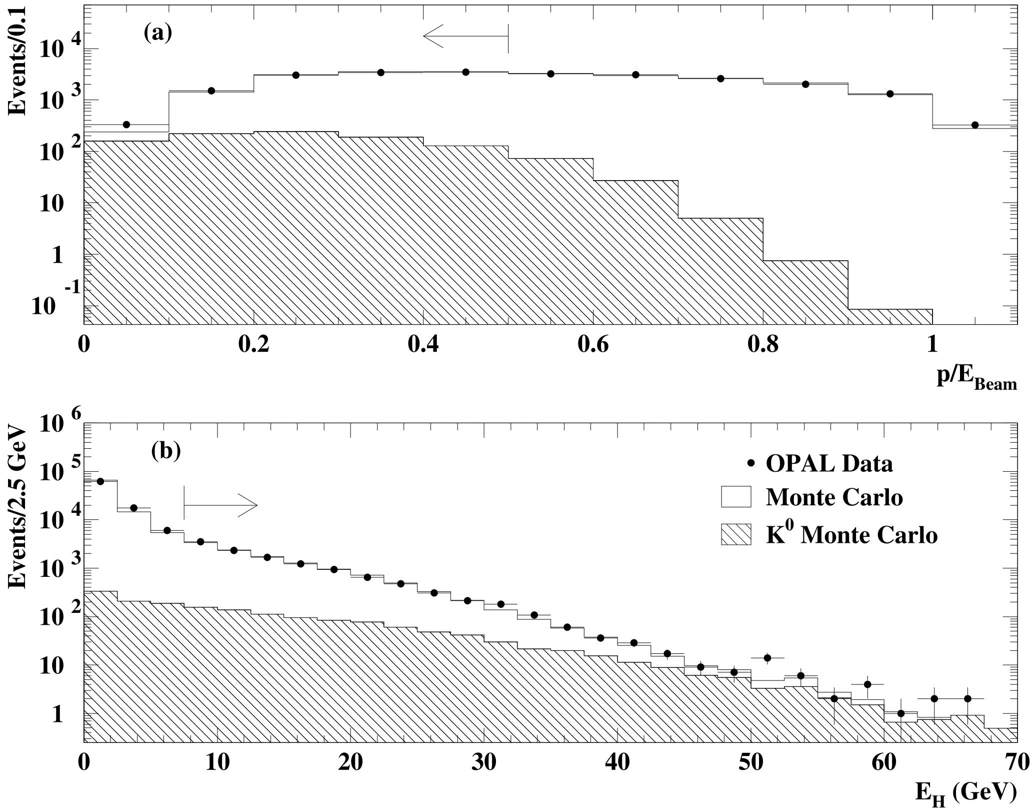

Figure 6.1: Histogram (a) shows the momentum divided by the beam energy (p/E_{Beam}) and histogram (b) shows the hadron calorimeter energy (E_{HB}). These plots show the number of decays for the one-prong τ sample and $e^+e^- \rightarrow q\overline{q}$ events after the other selection requirements (except S_{HB}) have been applied. The solid dots show the data, the open histogram shows the Monte Carlo and the hatched histogram shows the K^0_L component of the Monte Carlo.

at least one cluster in the hadron calorimeter and that the total energy deposited in the hadron calorimeter be greater than 7.5 GeV. Figure 6.1(b) shows the total hadron calorimeter energy (E_{HB}) for the one-prong sample after the other selection requirements, except S_{HB}, have been applied. The hatched region of the plot shows the K^0_L candidates in this sample. The energy calibration of the hadron calorimeter is discussed in Appendix A.

Decay mode	Background (%)
$\tau^- \to X^- \mathrm{K^0_S} \nu_\tau$	9.8 ± 0.5
$\tau^- \to h^- \pi^0 \nu_\tau$	6.5 ± 0.4
$\tau^- \to h^- \nu_\tau$	4.2 ± 0.4
$\tau^- \to h^- \geq 2\pi^0 \nu_\tau$	2.5 ± 0.3
other τ decays	0.2 ± 0.1
$\mathrm{e^+e^-} \to \mathrm{q\overline{q}}$	5.5 ± 0.4
total	28.6 ± 0.8

Table 6.1: The background contributions in the $\tau^- \to X^- \mathrm{K^0_L} \nu_\tau$ sample, including decays that contained $\mathrm{K^0_S}$ mesons. The quoted errors are the statistical uncertainties.

The decay, $\tau^- \to X^- \mathrm{K^0_L} \nu_\tau$, on average will deposit more energy in the hadron calorimeter than most other tau decays due to the neutral hadron $\mathrm{K^0_L}$ present in the final state. The hadronic energy measurement is exploited in the selection using a variable known as the significance factor, S_{HB}. This variable is defined as

$$S_{\mathrm{HB}} = \frac{E_{\mathrm{HB}} - p}{\sigma_{\mathrm{HB}}}, \tag{6.1}$$

where E_{HB} is the total energy deposited in the hadron calorimeter for the jet, p is the momentum of the track and σ_{HB} is the hadron calorimeter resolution at the energy E_{HB}. The $\mathrm{K^0_L} X^-$ decays are selected by requiring that $S_{\mathrm{HB}} \geq 2.0$. Figure 6.2 shows S_{HB} after the remaining requirements have been applied. Further details concerning S_{HB}, E_{HB} and σ_{HB} are discussed in Appendix A.

A total of 305 candidates are selected using the above requirements. The background is estimated to be 24% from other τ decays (including $\mathrm{K^0_S}$ final states) and 6% from $\mathrm{e^+e^-} \to \mathrm{q\overline{q}}$ events. Table 6.1 shows the contributions of the major background components in the $\tau^- \to X^- \mathrm{K^0_L} \nu_\tau$ sample.

Further, it should also be noted that some $\mathrm{K^0_S}$ mesons will be selected by the $\mathrm{K^0_L}$ selection. Approximately one-third of the $\mathrm{K^0_S}$ mesons will decay into $2\pi^0$ mesons. These are unlikely to be selected as the total energy deposited in the hadron calorimeter is small. The remaining $\mathrm{K^0_S}$ mesons decay into $\pi^+\pi^-$ pairs. The decay length

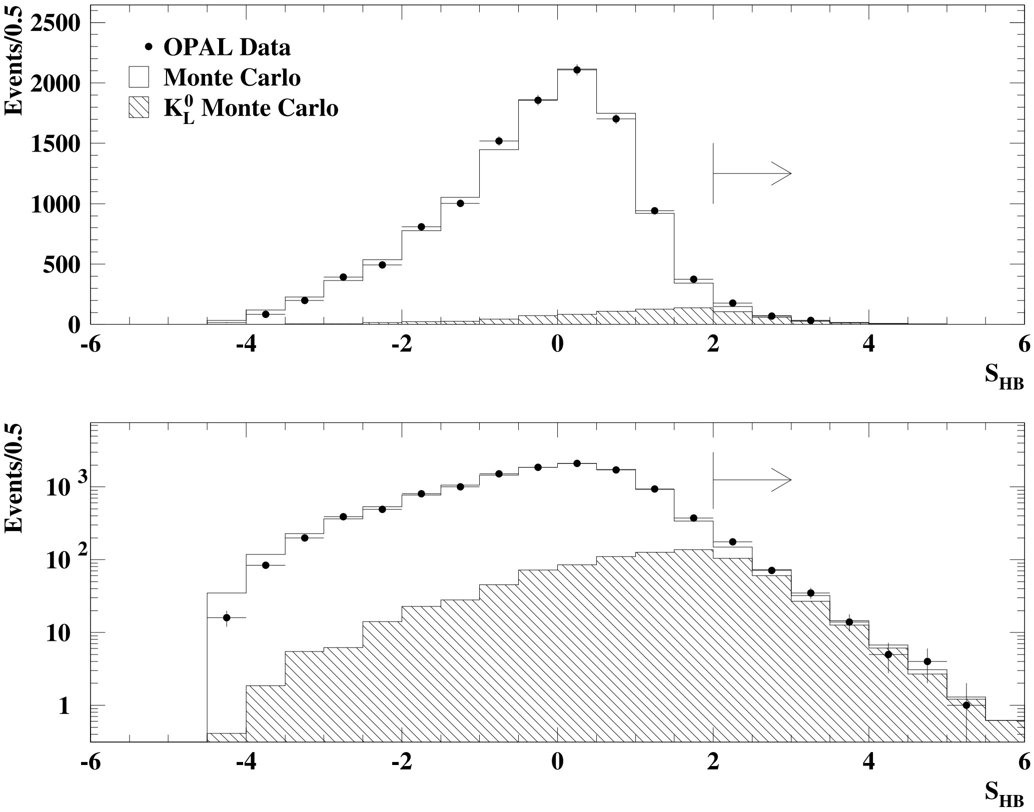

Figure 6.2: A histogram S_{HB} is plotted for the K^0_L candidates after the other selection requirements have been applied. The upper plot is linear and the lower plot is logarithmic. The solid dots show the data, the open histogram shows the Monte Carlo and the hatched histogram shows the K^0_L component of the Monte Carlo.

of some K^0_S mesons will be sufficiently long that they will be indistinguishable from K^0_L mesons. For the inclusive selection, these K^0_S mesons will be considered to be background which is estimated from the Monte Carlo. For the exclusive selections, described in the next section, these K^0_S mesons are included as part of the signal. Subsequently, the exclusive branching ratios are quoted as the sum of the branching ratios of the $\tau^- \to X^-\mathrm{K}^0_\mathrm{L}\nu_\tau$ and $\tau^- \to X^-\mathrm{K}^0_\mathrm{S}\nu_\tau$ decay modes. Figure 6.3 shows the K^0_S decay length plotted for the Monte Carlo K^0_S candidates selected after the $\tau^- \to X^-\mathrm{K}^0_\mathrm{L}\nu_\tau$ selection algorithm (except S_{HB}) was applied to the τ sample (open

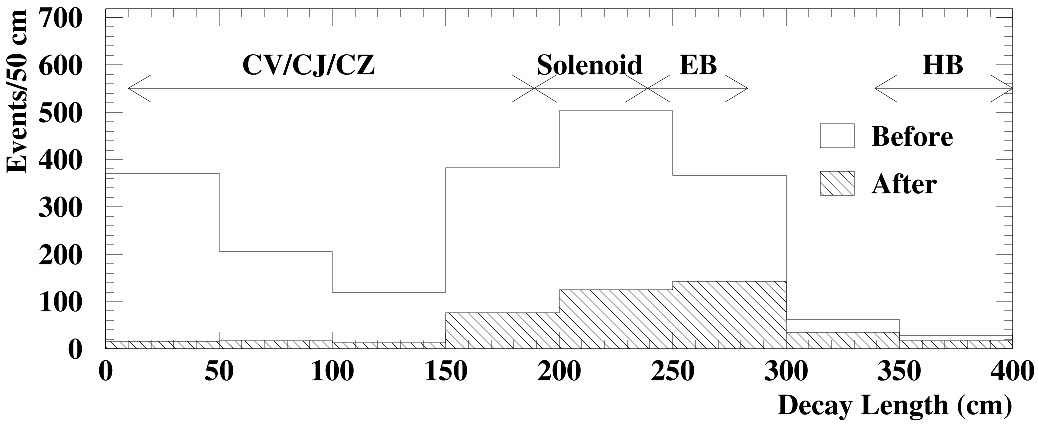

Figure 6.3: The open histogram shows the transverse decay length of the $\mathrm{K^0_S}$ decays after the selection requirements, except S_{HB}, have been applied to the τ sample. The $\mathrm{K^0_S}$ decays to both the $\pi^+\pi^-$ and $\pi^0\pi^0$ final states are shown. The hatched histogram shows the $\mathrm{K^0_S}$ decays after all the selection requirements were imposed on the τ sample. The various detector radii ranges are shown across the top of the plot.

histogram) and after the entire $\mathrm{K^0_L}$ selection (hatched histogram). Following the $\mathrm{K^0_L}$ selection, the Monte Carlo predicts that the sample is composed of 86% $\mathrm{K^0_L}$ and 14% $\mathrm{K^0_S}$ mesons.

6.2 Exclusive $\mathrm{K^0_L}$ Decay Modes

The inclusive $\tau^- \rightarrow X^-\mathrm{K^0_L}\nu_\tau$ candidate sample is divided into two sets using the energy loss ($\mathrm{d}E/\mathrm{d}x$) of the track in the jet chamber. The first sample contains decays where the charged track has been identified to be a pion, while the second sample contains decays in which the track has been identified as a kaon. The sample with charged pions is then passed through an additional selection which separates out the decays that include a π^0 meson. These selections will yield three decay modes: $\tau^- \rightarrow \pi^-\overline{\mathrm{K}}^0\nu_\tau$, $\tau^- \rightarrow \pi^-\overline{\mathrm{K}}^0 \geq 1\pi^0\nu_\tau$ and $\tau^- \rightarrow \mathrm{K^-K^0} \geq 0\pi^0\nu_\tau$. The $\tau^- \rightarrow \mathrm{K^-K^0} \geq 0\pi^0\nu_\tau$ decay mode is not subdivided further into decays with and without π^0 mesons because of the very low statistics of the charged kaon decay modes.

6.2.1 Charged Hadron Separation

In this analysis, charged kaons are identified on a statistical basis using the energy loss of the charged track, $\mathrm{d}E/\mathrm{d}x$, in the jet chamber. This technique is applied to the $\tau^- \to X^-\mathrm{K}^0_\mathrm{L}\nu_\tau$ candidate sample to distinguish $\tau^- \to \mathrm{K}^-\mathrm{K}^0_\mathrm{L}(\pi^0)\nu_\tau$ decays from $\tau^- \to \pi^-\overline{\mathrm{K}}^0_\mathrm{L}(\pi^0)\nu_\tau$ decays. The identification of the charged hadron uses the normalised $\mathrm{d}E/\mathrm{d}x$ which is defined to be

$$N\left(\frac{\mathrm{dE}}{\mathrm{d}x}\right) = \frac{\mathrm{d}E/\mathrm{d}x(\text{measured}) - \mathrm{d}E/\mathrm{d}x(\text{expected})}{\sigma_{\mathrm{d}E/\mathrm{d}x}}, \tag{6.2}$$

where $\mathrm{d}E/\mathrm{d}x$(measured) is the measured $\mathrm{d}E/\mathrm{d}x$ for the particle of interest at a given momentum, $\mathrm{d}E/\mathrm{d}x$(expected) is the expected value of the $\mathrm{d}E/\mathrm{d}x$ for the particle of interest at a given momentum and $\sigma_{\mathrm{d}E/\mathrm{d}x}$ is the momentum dependent $\mathrm{d}E/\mathrm{d}x$ resolution. As shown in Figure 4.1, the $\mathrm{d}E/\mathrm{d}x$ provides the best separation for charged pion and kaon mesons, at the level of 2σ, in the momentum range of 2-30 GeV. Figure 6.4(a) shows the number of $\mathrm{d}E/\mathrm{d}x$ hits that were used in the measurement and Figures 6.4(b) and (c) show the normalised $\mathrm{d}E/\mathrm{d}x$ for the pion and kaon hypotheses, respectively, for those events selected as $\tau^- \to X^-\mathrm{K}^0_\mathrm{L}\nu_\tau$ candidates.

The actual selection criteria to separate charged pions and kaons is made using a signed $\mathrm{d}E/\mathrm{d}x$ probability variable (W), which is calculated from the normalised $\mathrm{d}E/\mathrm{d}x$ variable for each particle species. The probability variable (or weight) is a flat distribution between -1 and 1 for a pure particle species (see Section 4.1 for more information). The probability of selecting pions or kaons is done using two new variables created from the weights:

$$\begin{aligned} \mathrm{P}(\pi) &= W_\pi/(W_\pi + W_\mathrm{K}) \qquad (6.3)\\ \mathrm{P}(\mathrm{K}) &= W_\mathrm{K}/(W_\pi + W_\mathrm{K}). \end{aligned}$$

Thus $\mathrm{P}(\pi)$ is the probability of selecting pions and $\mathrm{P}(\mathrm{K})$ is the probability of selecting kaons. Figures 6.4 (d) and (e) show $\mathrm{P}(\pi)$ and $\mathrm{P}(\mathrm{K})$ for the $\tau^- \to X^-\mathrm{K}^0_\mathrm{L}\nu_\tau$ decays. In

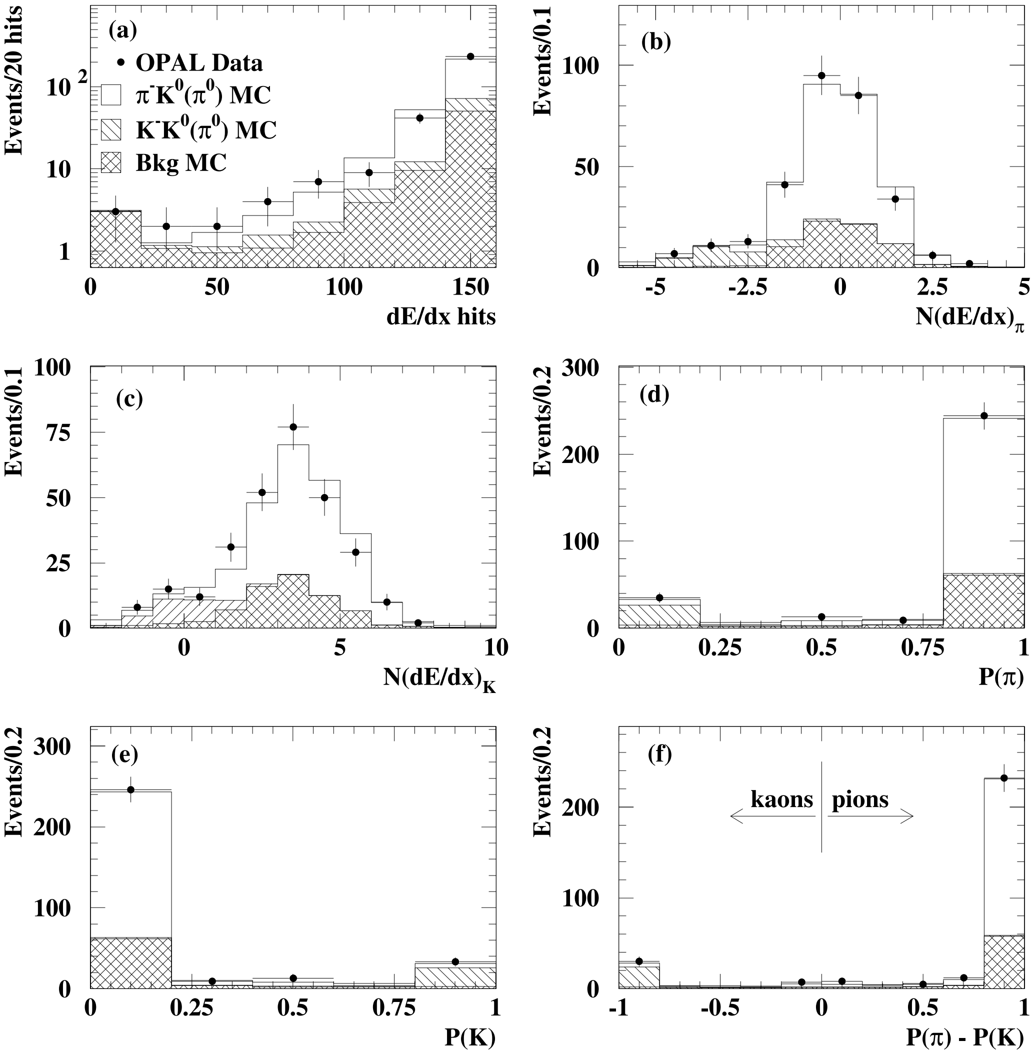

Figure 6.4: The normalised dE/dx variables for $\tau^- \rightarrow X^- \mathrm{K}^0_\mathrm{L}\nu_\tau$ decays. Histogram (a) shows the number of hits used in the dE/dx measurement for those events selected as $\tau^- \rightarrow X^- \mathrm{K}^0_\mathrm{L}\nu_\tau$ decays. Histograms (b) and (c) show the normalised dE/dx for the pion and kaon hypotheses, respectively. Histograms (d) and (e) show P(π) and P(K), respectively, and histogram (f) shows P(π) − P(K) for jets that pass the K^0_L selection. The points are the OPAL data, the open histogram shows the Monte Carlo simulation of the $\tau^- \rightarrow \pi^- \overline{\mathrm{K}}^0(\pi^0)\nu_\tau$ decays, the single hatched histogram shows the $\tau^- \rightarrow \mathrm{K}^- \mathrm{K}^0(\pi^0)\nu_\tau$ decays and the double hatched histogram shows the background contamination in the selected sample of decays.

Figure 6.4(f), $\mathrm{P}(\pi)-\mathrm{P}(\mathrm{K})$ is shown; a track is considered to be a pion if $\mathrm{P}(\pi) > \mathrm{P}(\mathrm{K})$ and a kaon otherwise. The selection yields 39 $\tau^- \to \mathrm{K}^-\mathrm{K}^0_\mathrm{L}(\pi^0)\nu_\tau$ candidates and 261 $\tau^- \to \pi^-\overline{\mathrm{K}}^0_\mathrm{L}(\pi^0)\nu_\tau$ candidates.

6.2.2 π^0 Finding Algorithm

The π^0 decays that are selected in this analysis involve only those π^0 mesons that decay into two photons due to the one-prong nature of the selection. At LEP, the π^0 mesons from τ decays are highly relativistic and the two photons from the $\pi^0 \to \gamma\gamma$ decay will be very close to each other. Hence, the two photons will usually form one electromagnetic cluster, although at low energies two clusters can sometimes result. Some photons may also travel close to the charged hadron, thus the energy deposited by the photons and the charged hadron merge and form one cluster. Further, the K^0_L can leave energy in the electromagnetic calorimeter that can be misidentified as a π^0 meson. Thus any electromagnetic clusters in the jet may have energy from both the K^0_L and the π^0. Consequently, this analysis used a neural net algorithm to select decays with π^0 mesons, instead of trying to identify the individual π^0 mesons in the decays.

The neural net algorithm used in this analysis was constructed using the JETNET 3.4 [51] algorithm. The variable selection is described in Appendix C. The neural network used seven variables, which are described below:

- The total energy of the jet in the electromagnetic calorimeter divided by the beam energy, E/E_{beam}.
- The total energy of the jet in the electromagnetic calorimeter divided by the momentum of the track, E/p.
- The number of electromagnetic clusters in the jet with $E_{\mathrm{clusters}} > 1$ GeV.

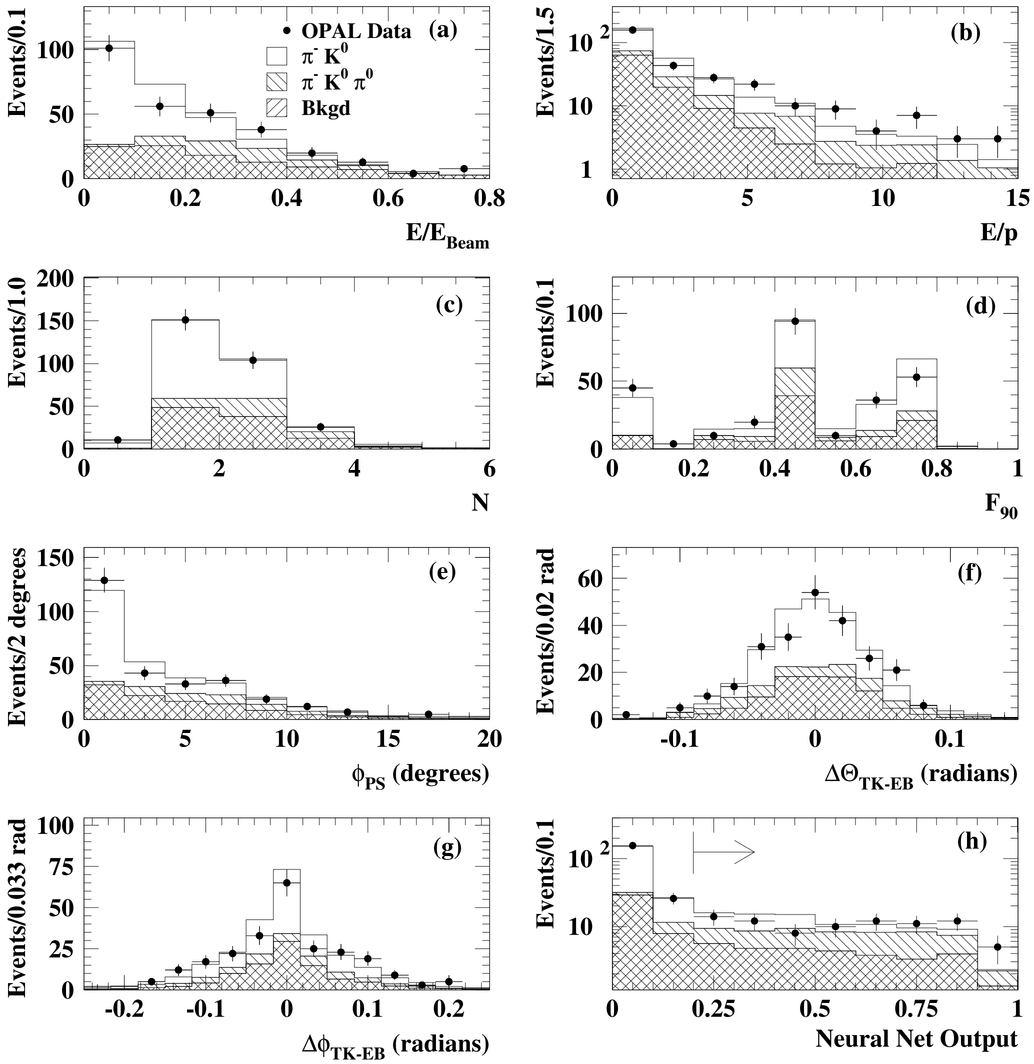

Figure 6.5: The variables used in the neural network routine for identifying π^0 mesons in the K^0_L selection: Histogram (a) shows the electromagnetic energy divided by the beam energy; plot (b) shows the ratio of the electromagnetic cluster energy (E) with the momentum of the track (p); plot (c) shows the number of electromagnetic calorimeter clusters (N); plot (d) shows the fraction of lead glass blocks in the electromagnetic calorimeter with over 90% of the energy in the jet; plot (e) shows angle between the position of the track at the presampler and the presampler cluster furthest away from the jet axis; plots (f) and (g) show the difference in theta ($\Delta\theta$) and phi ($\Delta\phi$) between the track and the vector obtained by adding all the clusters in the electromagnetic calorimeter; and plot (h) shows the output of the neural network.

- The minimum fraction of active lead glass blocks which together contains more than 90% of the total electromagnetic energy of the jet, F_{90}.
- The difference in the azimuthal angle between the track and the presampler signal farthest away from the track but still within the jet, ϕ_{PS}.
- The difference in theta ($\Delta\theta$) and phi ($\Delta\phi$) between the track and the vector obtained by adding together all the electromagnetic calorimeter clusters in the jet.

The variables used in the neural network and the output are shown in Figure 6.5. If the neural network output is larger than 0.2 then the decay is considered to contain a π^0 meson. The cut was chosen to maximise the $\tau^- \rightarrow \pi^-\overline{\mathrm{K}}^0 \geq 1\pi^0\nu_\tau$ signal while reducing as much as possible the $\tau^- \rightarrow \pi^-\overline{\mathrm{K}}^0\nu_\tau$ contamination in the $\tau^- \rightarrow \pi^-\overline{\mathrm{K}}^0 \geq 1\pi^0\nu_\tau$ sample. The variation of the cut on the neural network output is discussed further in Section 7.3.6 where it is observed that the branching ratios remain consistent when the cut is varied between 0.1 and 0.8. This selection gives 178 $\tau^- \rightarrow \pi^-\overline{\mathrm{K}}^0\nu_\tau$ decays and 81 $\tau^- \rightarrow \pi^-\overline{\mathrm{K}}^0 \geq 1\pi^0\nu_\tau$ decays. For more information about the neural network algorithm see Appendix C.

Chapter 7

Results

This chapter describes the calculation of the inclusive branching ratio of the $\tau^- \to X^- \mathrm{K}^0_\mathrm{L} \nu_\tau$ decay mode and the exclusive decay modes $\tau^- \to \pi^- \overline{\mathrm{K}}^0 \nu_\tau$, $\tau^- \to \pi^- \overline{\mathrm{K}}^0 \geq 1\pi^0 \nu_\tau$ and $\tau^- \to \mathrm{K}^- \mathrm{K}^0 \geq 0\pi^0 \nu_\tau$. The first section describes the measurement of the inclusive branching fraction. The second section describes the calculation of the branching ratios of the three exclusive decay modes.

7.1 Inclusive Branching Ratio

7.1.1 Branching ratio for a single decay channel

The branching ratio to a final state X (eg. $\tau^- \to X^- \nu_\tau$) is defined as

$$B_X \equiv \frac{N_X}{N_\tau}, \tag{7.1}$$

where N_X is the number of $\tau^- \to X^- \nu_\tau$ decays in a sample containing N_τ taus. In practice, the sample of tau decays will contain background from other events. Consequently, the true number of taus in the sample (N_τ) is given by

$$N_\tau = (1 - f^{\mathrm{non}-\tau}) N_\tau^{\mathrm{sel}}, \tag{7.2}$$

where $f^{\text{non}-\tau}$ is the fraction of background events present in a sample of N_τ^{sel} taus. The number of true $\tau^- \to X^-\nu_\tau$ decays, N_X, is given by

$$N_X = \frac{(1 - f^{\text{non}-X})N_X^{\text{sel}}}{\epsilon} \tag{7.3}$$

where N_X^{sel} is the number of selected $\tau^- \to X^-\nu_\tau$ decays, $f^{\text{non}-X}$ is the fraction of background events present in the selected sample of $\tau^- \to X^-\nu_\tau$ decays and ϵ is the selection efficiency of the $\tau^- \to X^-\nu_\tau$ decays determined by the Monte Carlo. Finally, equation 7.1 is rewritten as

$$B_X = \frac{1}{\epsilon}\frac{N_X^{\text{sel}}(1 - f^{\text{non}-X})}{N_\tau^{\text{sel}}(1 - f^{\text{non}-\tau})}. \tag{7.4}$$

The τ pair selection does not select all decay modes equally and introduces relative biases between τ decays. These biases were studied using the Monte Carlo samples. The *bias factors* are used to correct the biases in the branching ratios from the τ pair selected sample, such that the true branching ratio is obtained by dividing equation 7.4 by its bias factor (F^{bias}):

$$B_X^{\text{true}} = \frac{B_X}{F^{\text{bias}}}. \tag{7.5}$$

The bias factor for the $\tau^- \to X^-\mathrm{K}_\mathrm{L}^0\nu_\tau$ decays is measured to be 0.991 ± 0.007. A more thorough description of the bias factors is given in Appendix D.

7.1.2 Results

The inclusive analysis selected 305 $\tau^- \to X^-\mathrm{K}_\mathrm{L}^0\nu_\tau$ candidates. The selection efficiency ϵ and τ background ($f^{\text{non}-X^-\mathrm{K}_\mathrm{L}^0}$) are summarised in Table 7.1. For the inclusive selection, the decays containing K_S^0 are included as part of the background which is determined by the Monte Carlo. Evaluating equation 7.4 and correcting for the bias factor, $F^{\text{bias}}_{X^-\text{K}^0_\text{L}}$, yields the branching ratio:

$$B(\tau^- \to X^-\text{K}^0_\text{L}\nu_\tau) = (10.01 \pm 0.79 \pm 0.64) \times 10^{-3}, \tag{7.6}$$

where the first error is the statistical uncertainty and the second error is the systematic uncertainty. The statistical uncertainty is given by the binomial error on the ratio $N_{X^-\text{K}^0_\text{L}}/N_\tau$, where $N_{X^-\text{K}^0_\text{L}}$ is the selected number (N^{sel}_X) of $\tau^- \to X^-\text{K}^0_\text{L}\nu_\tau$ decays. Systematic uncertainties are discussed in Section 7.3.

N_τ	201850
$N_{X^-\text{K}^0_\text{L}}$	305
ϵ	0.110 ± 0.002
$f^{\text{non}-\tau}$	0.016 ± 0.001
$f^{\text{non}-X^-\text{K}^0_\text{L}}$	0.286 ± 0.008
$F^{\text{bias}}_{X^-\text{K}^0_\text{L}}$	0.991 ± 0.007
$B(\tau^- \to X^-\text{K}^0_\text{L}\nu_\tau)$	$(10.01 \pm 0.79 \pm 0.64) \times 10^{-3}$

Table 7.1: Summary of results for the inclusive $\tau^- \to X^-\text{K}^0_\text{L}\nu_\tau$ selection. The quoted errors on the efficiency, backgrounds and bias factor are given by the statistical uncertainty. The first error on the branching ratio is the statistical uncertainty while the second is the systematic uncertainty.

7.2 Exclusive Branching Ratios

In this analysis, three decay modes (channels) were identified: $\tau^- \to \pi^-\overline{\text{K}}^0\nu_\tau$, $\tau^- \to \pi^-\overline{\text{K}}^0 \geq 1\pi^0\nu_\tau$ and $\tau^- \to \text{K}^-\text{K}^0 \geq 0\pi^0\nu_\tau$. However, the selection algorithms did not select each mode exclusively, therefore each selected sample contains some decays from the other two decay modes. For example, the $\tau^- \to \pi^-\overline{\text{K}}^0\nu_\tau$ decay mode includes some $\tau^- \to \pi^-\overline{\text{K}}^0 \geq 1\pi^0\nu_\tau$ and $\tau^- \to \text{K}^-\text{K}^0 \geq 0\pi^0\nu_\tau$ decays as well as other τ decays (background decays). As a result, the branching ratios for the three decay modes are calculated simultaneously to take these correlations into account.

The number of observed decays for each channel can be written in terms of the number of true (signal) decays, background from other τ decays and background from non-τ events as

$$N^{\rm sel} = \sum_s N_s^{\rm sel} + \sum_b N_b^{\rm sel} + N^{\rm non-\tau}. \tag{7.7}$$

or alternatively, using equation 7.3 this equation can be written as

$$N^{\rm sel} = \sum_s \epsilon_s N_s + \sum_b \epsilon_b N_b + N^{\rm non-\tau}, \tag{7.8}$$

where s is the index over all signal channels, b is the index over all background channels, N_s (N_b) is the number of signal (background) decays, ϵ_s (ϵ_b) is the efficiency to select signal (background) decays and $N^{\rm non-\tau}$ is the number of non-τ events in the selected sample. Dividing equation 7.8 by N_τ and substituting equations 7.1 and 7.2 gives

$$\sum_s \epsilon_s B_s + \sum_b \epsilon_b B_b = \frac{N^{\rm sel} - N^{\rm non-\tau}}{(1 - f^{\rm non-\tau}) N_\tau^{\rm sel}}, \tag{7.9}$$

where B_s and B_b are the branching ratios of the signal and background decays.

The formalism can be extended into three selections, $\tau^- \to \pi^- \overline{\rm K}^0 \nu_\tau$, $\tau^- \to \pi^- \overline{\rm K}^0 \geq 1\pi^0 \nu_\tau$ and $\tau^- \to {\rm K}^- {\rm K}^0 \geq 0\pi^0 \nu_\tau$ by adding an index i to equation 7.9,

$$\epsilon_{i1} B_1 + \epsilon_{i2} B_2 + \epsilon_{i3} B_3 + \sum_{k=4}^{M} \epsilon_{ik} B_k = \frac{N_i^{\rm sel} - N_i^{\rm non-\tau}}{N_\tau^{\rm sel}(1 - f^{\rm non-\tau})}\ , \tag{7.10}$$

where ϵ_{ij} ($j = 1, 3$) are the efficiencies for selecting signal j using selection i and ϵ_{ik} ($k = 4, ...$) are the efficiencies for selecting the τ background modes using selection i. The branching ratios of the signal channels and backgrounds are B_j ($j = 1, 3$) and B_k ($k = 4, ...$), respectively. The number of data events that pass the selection i is $N_i^{\rm sel}$ and $N_i^{\rm non-\tau}$ is the non-τ background present in each selection i. The fraction of non-tau events in the tau pair sample is $f^{non-\tau}$ and $N_\tau^{\rm sel}$ is the total number of data τ's that pass the tau pair selection.

The selection efficiencies (ϵ_{ij}) for both signal and background are determined directly from the Monte Carlo. The efficiency for detecting decay channel j in selection i is defined as

$$\epsilon_{ij} = \frac{N_{ij}}{N_j} \tag{7.11}$$

and the uncertainty on the efficiency is given by the binomial error as

$$\sigma_{\epsilon_{ij}} = \sqrt{\frac{\epsilon_{ij}(1-\epsilon_{ij})}{N_j}}, \tag{7.12}$$

where N_{ij} is the number of j decays identified by selection i and N_j is the total number of j decays.

Equation 7.10 can be written in matrix form as

$$[\epsilon][B] = [n] \tag{7.13}$$

where $[\epsilon]$ is a 3×3 matrix of all signal efficiencies, $[B]$ is a 3×1 dimensional matrix of the signal branching ratios and $[n]$ is a 3×1 dimensional matrix with entries

$$n_i = \frac{N_i^{\mathrm{sel}} - N_i^{\mathrm{non}-\tau}}{N_\tau(1 - f^{\mathrm{non}-\tau})} - \sum_{k=4}^{M} \epsilon_{ik} B_k \tag{7.14}$$

containing the fraction of events in each selection after the background is subtracted. If $[\epsilon]$ is a nonsingular matrix, the branching ratios $[B]$ can be solved as

$$[B] = [\epsilon]^{-1}[n] \tag{7.15}$$

where $[\epsilon]^{-1}$ is the inverse of the efficiency matrix. Finally, each branching ratio is divided by its bias factor (F^{bias}) to correct for the fact that the tau-pair selection favours some decay modes over others (see Appendix D).

The branching ratio B_i can be written explicitly using equation 7.13 as,

$$B_i = \frac{1}{F_i^{\mathrm{bias}}} \sum_{j=1}^{3} \epsilon_{ij}^{-1} \left(\frac{N_j^{\mathrm{sel}} - N_j^{\mathrm{non}-\tau}}{(1 - f^{\mathrm{non}-\tau}) N_\tau^{\mathrm{sel}}} - \sum_{k=4}^{M} \epsilon_{jk} B_K \right). \tag{7.16}$$

The statistical uncertainty on B_i comes from the first term inside the parentheses in equation 7.16. It is calculated to be

$$\sigma^2_{B_i}(\text{stat}) = \frac{1}{(1 - f^{\text{non}-\tau})^2} \sum_{j=1}^{3} \left(\epsilon^{-1}_{ij} \sigma^{\text{stat}}_j \right)^2, \tag{7.17}$$

where

$$\sigma^{\text{stat}}_j = \sqrt{\frac{\frac{N^{\text{sel}}_j}{N^{\text{sel}}_\tau} \left(1 - \frac{N^{\text{sel}}_j}{N^{\text{sel}}_\tau}\right)}{N^{\text{sel}}_\tau}}. \tag{7.18}$$

More information on how to calculate the error on an inverse matrix is described in Appendix E. The systematic uncertainties due to the Monte Carlo statistics is described in Section 7.3.1. These uncertainties arise from the errors on each element of the inverse efficiency matrix ϵ^{-1}_{ij}.

7.2.1 Results

The selections for the $\tau^- \to \pi^- \overline{\text{K}}^0 \nu_\tau$, $\tau^- \to \pi^- \overline{\text{K}}^0 \geq 1\pi^0 \nu_\tau$ and $\tau^- \to \text{K}^- \text{K}^0 \geq 0\pi^0 \nu_\tau$ decays yielded 178, 81 and 41 events, respectively. These decay modes include both K^0_L and K^0_S mesons which are collectively called K^0. The selection efficiencies ϵ_{ij} for both signal and background are determined directly from the Monte Carlo and are given in the top part of Table 7.2. The central part of Table 7.2 gives the results of this analysis. The uncertainties on the backgrounds and bias factors are the binomial errors due to the Monte Carlo statistics only. The quoted efficiencies are calculated for observing a K^0. The branching ratios obtained using this analysis are

$$\begin{aligned}
B(\tau^- \to \pi^- \overline{\text{K}}^0 \nu_\tau) &= (9.1 \pm 0.9 \pm 0.6) \times 10^{-3} \\
B(\tau^- \to \pi^- \overline{\text{K}}^0 \geq 1\pi^0 \nu_\tau) &= (3.6 \pm 1.3 \pm 1.0) \times 10^{-3} \\
B(\tau^- \to \text{K}^- \text{K}^0 \geq 0\pi^0 \nu_\tau) &= (3.3 \pm 0.9 \pm 0.7) \times 10^{-3},
\end{aligned}$$

where the first uncertainty is statistical and the second is systematic. The statistical correlation coefficients between the three branching ratios are shown in Table 7.2. The correlation coefficients ρ_{ij} were calculated using

$$\rho_{ij} = \frac{\mathrm{cov}_{ij}}{\sigma_i \sigma_j}, \tag{7.19}$$

where cov_{ij} is the covariance between branching ratio i and j, and σ_i (σ_j) is the statistical error on branching ratio i (j). The statistical error matrix between the three branching ratios is given by [52]

$$\mathrm{cov}_{ij} = \frac{\delta B_j}{\delta n_i} \; \sigma_{n_j} \; \frac{\delta B_i}{\delta n_j}, \tag{7.20}$$

where cov_{ij} is the covariance between branching ratio i and j, $\delta B_{j,i}/\delta n_{i,j}$ is the uncertainty on branching ratio j (i) due to fraction n_i (n_j) and σ_{n_j} is the statistical error on fraction n_i given by equation 7.18. In addition, if $i = j$ then $\mathrm{cov}_{ij} = \sigma_i$ is the statistical error on branching ratio i. Finally, the systematic uncertainty is discussed in the next section.

7.3 Systematic error evaluation

This section discusses the systematic errors of the branching ratios. There are two kinds of systematic errors. The first type, although considered a systematic error, is statistical in nature as it arises from the finite size of the Monte Carlo sample. The second type of systematic error includes instrumental uncertainties associated with the modelling of the physical processes or the modelling of the detectors response. The estimated systematic errors on the branching ratio measurements are shown in Table 7.3. The statistical uncertainties will be described first, followed by the instrumental uncertainties.

Efficiency Matrix

Selection	Decay Channel		
	$\tau^- \to \pi^- \overline{\mathrm{K}}^0 \nu_\tau$	$\tau^- \to \pi^- \overline{\mathrm{K}}^0 \geq 1\pi^0 \nu_\tau$	$\tau^- \to \mathrm{K}^- \mathrm{K}^0 \geq 0\pi^0 \nu_\tau$
$\tau^- \to \pi^- \overline{\mathrm{K}}^0 \nu_\tau$	0.0736 ± 0.0018	0.0081 ± 0.0009	0.0028 ± 0.0006
$\tau^- \to \pi^- \overline{\mathrm{K}}^0 \geq 1\pi^0 \nu_\tau$	0.0105 ± 0.0007	0.0360 ± 0.0019	0.0008 ± 0.0003
$\tau^- \to \mathrm{K}^- \mathrm{K}^0 \geq 0\pi^0 \nu_\tau$	0.0043 ± 0.0005	0.0019 ± 0.0004	0.0353 ± 0.0021

Exclusive Results

	$\tau^- \to \pi^- \overline{\mathrm{K}}^0 \nu_\tau$	$\tau^- \to \pi^- \overline{\mathrm{K}}^0 \geq 1\pi^0 \nu_\tau$	$\tau^- \to \mathrm{K}^- \mathrm{K}^0 \geq 0\pi^0 \nu_\tau$
$N_i^{\mathrm{K}^0}$	178	81	41
N_τ	201850	201850	201850
$f^{\mathrm{non}-\tau}$	0.016 ± 0.001	0.016 ± 0.001	0.016 ± 0.001
$f^{\mathrm{non}-\mathrm{K}^0}$	0.218 ± 0.009	0.448 ± 0.016	0.215 ± 0.019
F^{bias}	0.986 ± 0.009	0.995 ± 0.015	0.999 ± 0.015
$\mathrm{BR}(\times 10^{-3})$	$9.1 \pm 0.9 \pm 0.6$	$3.6 \pm 1.3 \pm 1.0$	$3.3 \pm 0.9 \pm 0.7$

Statistical Correlation Coefficients

	$\tau^- \to \pi^- \overline{\mathrm{K}}^0 \nu_\tau$	$\tau^- \to \pi^- \overline{\mathrm{K}}^0 \geq 1\pi^0 \nu_\tau$
$\tau^- \to \pi^- \overline{\mathrm{K}}^0 \geq 1\pi^0 \nu_\tau$	$-.349$	
$\tau^- \to \mathrm{K}^- \mathrm{K}^0 \geq 0\pi^0 \nu_\tau$	$-.133$	$-.041$

Table 7.2: Summary of results for the exclusive K^0 selections. The first table gives the efficiencies for identifying the signals for each selection. The second table shows the number of selected events for each channel, the background fraction, the bias factor and the branching ratios. The third table gives the statistical correlation coefficients between the three branching ratios.

7.3.1 Monte Carlo statistics

The error on the branching ratios due to the Monte Carlo statistics is calculated directly from the statistical uncertainties on the elements of the inverse efficiency matrix $[\epsilon]^{-1}$ for the exclusive channels, and the statistical uncertainty of the efficiency for the inclusive channel. The systematic uncertainty on B_i is found from equation 7.15

Systematic	Selection			
Error	$\mathrm{K_L^0}X^-\nu_\tau$	$\overline{\mathrm{K}}^0\pi^-\nu_\tau$	$\overline{\mathrm{K}}^0\pi^- \geq 1\pi^0\nu_\tau$	$\mathrm{K^0K^-} \geq 0\pi^0\nu_\tau$
$\mathrm{K_L^0}$ Selection	±0.55	±0.40	±0.68	±0.42
Background	±0.24	±0.29	±0.50	±0.31
MC Statistics	±0.22	±0.24	±0.28	±0.24
Bias Factor	±0.07	±0.14	±0.05	±0.05
dE/dx modeling	—	±0.21	±0.11	±0.33
π^0 Selection	—	±0.14	±0.27	—
MC modelling	—	±0.00	±0.39	±0.17
Total	±0.64	±0.62	±1.02	±0.68

Table 7.3: Systematic errors on the branching ratios for the inclusive and exclusive decay channels. All values in the table should be multiplied by 10^{-3}.

and is given by

$$\sum_{j=1}^{3}(\sigma_{\epsilon_{ij}^{-1}} n_j)^2. \tag{7.21}$$

Each element of the inverse efficiency matrix has a covariance matrix which is made up of contributions from all the statistical errors in the efficiency matrix. A more thorough description of $\sigma_{\epsilon_{ij}^{-1}}$ is given in Appendix E.

7.3.2 Bias factor

A small correction, as described in Appendix D, must be applied to the branching ratios to correct for the slight bias introduced by the τ-pair selection criteria. The systematic error on each branching ratio is calculated using the bias factor error. The factors are found to be relatively insensitive to the branching ratios and detector configurations used in the Monte Carlo sample. Further, minor variations in the tau pair selection are found to have little impact on the values of the bias factors.

7.3.3 K^0_L selection efficiency

The K^0_L selection efficiency was sensitive to the calibration of the momentum, the energy measured by the hadron calorimeter and the resolution of the hadron calorimeter. A recent OPAL result estimated that the momentum scale was measured to better than 1% [53]. Consequently the systematic error on the K^0_L selection efficiency was estimated by varying the momentum of the track of the charged hadron by ±1%. After the momentum was varied, the branching ratio was recalculated and the difference between this value and the nominal value was taken as the systematic error. The uncertainty in the energy calibration of the hadron calorimeter was obtained by studying a sample of single charged hadrons from tau decays (see Appendix A) and agreement between data and Monte Carlo was good at the 1.5% level. The energy measured by the hadron calorimeter was varied by ±1.5% and the branching ratios were recalculated, the difference between these results and the nominal branching ratios were taken as the systematic errors. The uncertainty due to the measurement of the resolution of the hadron calorimeter was estimated by varying the resolution within its uncertainties and recalculating the branching ratios; the differences between these branching ratios and the nominal branching ratios were taken as the systematic errors. The contributions to the systematic error from the various sources are shown in Table 7.4. Several consistency checks were done by varying the cut values on p/E_{Beam}, E_{HB} and S_{HB}: p/E_{Beam} was varied between 0.3 and 0.7; E_{HB} was varied from 0.0 GeV to 15.0 GeV; and S_{HB} was varied from 1.6 to 2.4. The results were within the systematic uncertainty for each branching ratio.

Systematic	Selection			
Error	$\mathrm{K^0_L} X^- \nu_\tau$	$\overline{\mathrm{K}}^0 \pi^- \nu_\tau$	$\overline{\mathrm{K}}^0 \pi^- \geq 1\pi^0 \nu_\tau$	$\mathrm{K^0 K^-} \geq 0\pi^0 \nu_\tau$
p scale	±0.24	±0.14	±0.24	±0.12
E_{HB} scale	±0.43	±0.48	±0.50	±0.31
Resolution (σ_{HB})	±0.24	±0.23	±0.42	±0.36
Total	±0.55	±0.40	±0.68	±0.42

Table 7.4: Systematic errors on the branching ratios for the $\mathrm{K^0_L}$ selection efficiency. The values in the table should be multiply by 10^{-3}.

7.3.4 Background

The systematic error due to the background in the $\mathrm{K^0_L}$ selection includes the uncertainty in the branching ratios of the background decays as well as the Monte Carlo statistical uncertainty. This background includes the $\tau^- \to \pi^- \overline{\mathrm{K}}^0 \mathrm{K}^0 \nu_\tau$ and $\tau^- \to \pi^- \overline{\mathrm{K}}^0 \mathrm{K}^0 \pi^0 \nu_\tau$ decay modes in which the two K^0 mesons appear as one K^0 meson in the selected sample. The uncertainty in the background due to these branching ratios includes the Monte Carlo statistical uncertainty plus a contribution due to the uncertainty in the branching ratios of these decays [3, p. 286] [54]. The non-K^0 background consists primarily of π^-, $\rho(770)^-$ and $\mathrm{a}_1(1260)^-$ decays.

To investigate this background, the S_{HB} selection cut was reversed and the invariant mass spectra were studied for each decay mode (see Figure 7.1). The ratios of the data to the Monte Carlo simulation: 0.97 ± 0.02, 1.04 ± 0.02 and 0.94 ± 0.06 for the $\pi^- \overline{\mathrm{K}}^0$, $\pi^- \overline{\mathrm{K}}^0 \geq 1\pi^0$ and $\mathrm{K^- K^0} \geq 0\pi^0$ selections, respectively, are consistent. The errors on the ratios are taken as contributions to the systematic uncertainty on the background. The various contributions to the total systematic error from the background are added in quadrature.

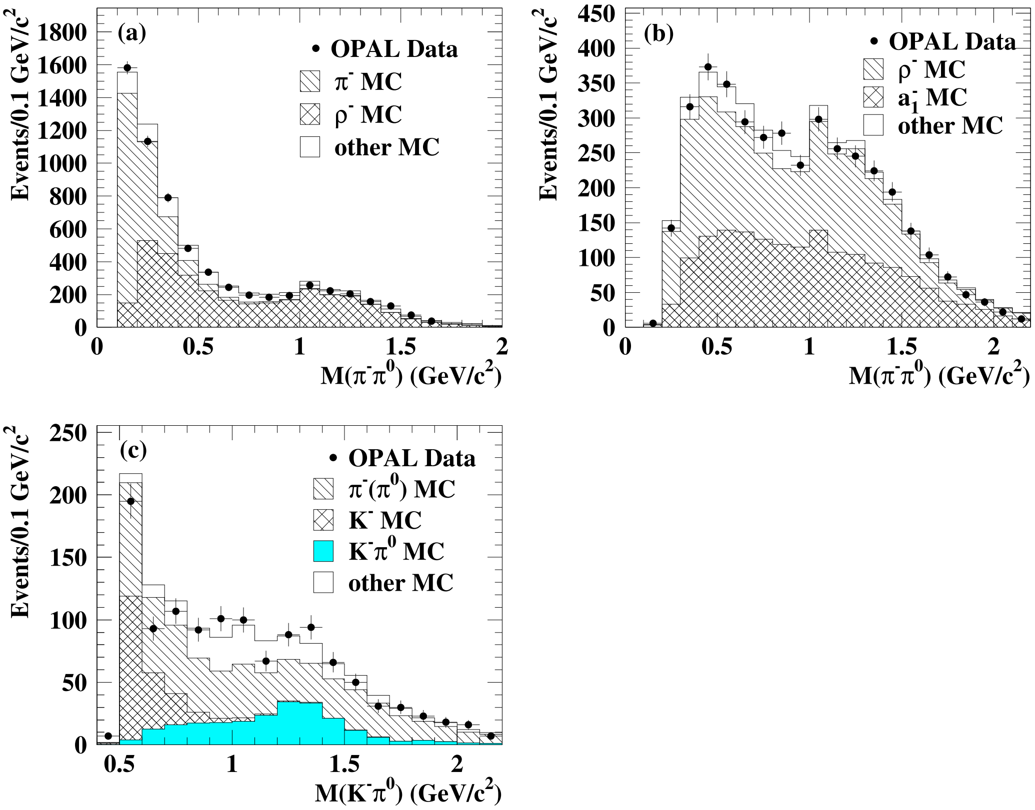

Figure 7.1: The jet mass is plotted for those decays that are rejected by the K^0_L selection when the requirement on S_{HB} is reversed. The plots, (a), (b) and (c) respectively, are shown for the decays rejected by the $\tau^- \to \pi^-\overline{\mathrm{K}}^0\nu_\tau$, $\tau^- \to \pi^-\overline{\mathrm{K}}^0 \geq 1\pi^0\nu_\tau$ and $\tau^- \to \mathrm{K}^-\mathrm{K}^0 \geq 0\pi^0\nu_\tau$ selections. The data are the points while the various tau background decays are shown on each plot.

7.3.5 dE/dx Modeling

The dE/dx pion and kaon probabilities are obtained from the normalized pion and kaon dE/dx, respectively. The Monte Carlo parameterization of the normalized dE/dx distributions was studied using a sample of single charged hadrons from tau decays. The systematic error on the branching ratios associated with the dE/dx modelling, see Appendix B, was obtained by varying the means of the normalised dE/dx

distributions by ±1 standard deviation from their central values. In addition, to account for possible differences in the $\mathrm{d}E/\mathrm{d}x$ modelling, the widths of the normalised $\mathrm{d}E/\mathrm{d}x$ distributions are varied by ±30%. Varying the mean of the normalised $\mathrm{d}E/\mathrm{d}x$ distributions for the pion hypothesis gave errors of 0.00008, 0.00007 and 0.00022 on the $\pi^-\overline{\mathrm{K}}^0$, $\pi^-\overline{\mathrm{K}}^0 \geq 1\pi^0$ and $\mathrm{K}^-\mathrm{K}^0 \geq 0\pi^0$ modes, respectively. Similarly, varying the mean of the normalised $\mathrm{d}E/\mathrm{d}x$ distributions for the kaon hypothesis gave errors of 0.00010, 0.00005 and 0.00014, while varying the widths gave errors of 0.00015, 0.00007 and 0.00019 for the three decay modes, respectively. The errors are added in quadrature and are shown in Table 7.3.

7.3.6 π^0 Identification

The analysis used a neural network algorithm to separate $\tau^- \to \pi^-\overline{\mathrm{K}}^0\nu_\tau$ from $\tau^- \to \pi^-\overline{\mathrm{K}}^0 \geq 1\pi^0\nu_\tau$ decays. The most powerful variable for distinguishing between these two decays is the energy deposited in the electromagnetic calorimeter. The systematic error on the branching ratios is evaluated by shifting the electromagnetic energy scale by ±1.0% based on studies of tau 3-prong decays [55]. The branching ratios were recalculated using the different energy scales and the difference between these results and the nominal branching ratios were taken as the systematic errors: 0.00007 and 0.00013 for the $\pi^-\overline{\mathrm{K}}^0$ and $\pi^-\overline{\mathrm{K}}^0 \geq 1\pi^0$ decays, respectively.

The uncertainty on the π^0 identification also includes the maximum difference when each of the remaining variables (except the ones that depend on the energy) are individually dropped from the neural network algorithm. The contributions to the error are 0.00014 and 0.00027 for the $\pi^-\overline{\mathrm{K}}^0$ and $\pi^-\overline{\mathrm{K}}^0 \geq 1\pi^0$ decays, respectively. These uncertainties are added in quadrature with those obtained from the energy scale uncertainty. Several consistency checks on the branching ratios were conducted. For

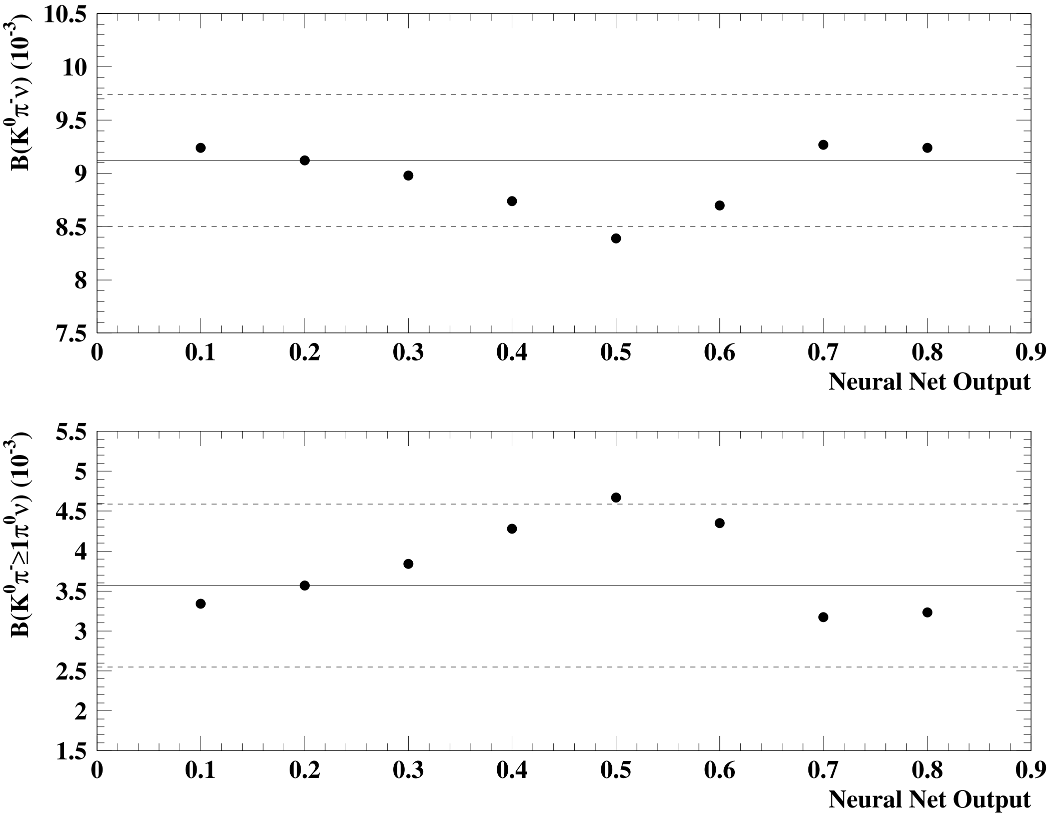

Figure 7.2: The branching ratio of the $\tau^- \to \pi^- \overline{\mathrm{K}}^0 \nu_\tau$ and $\tau^- \to \pi^- \overline{\mathrm{K}}^0 \geq 1\pi^0 \nu_\tau$ decay modes is plotted against the output of the neural network. The solid line give the nominal branching ratio and the dotted lines show the systematic error.

example, the neural net output cut was varied between 0.1 and 0.8 (see Figure 7.2). Another check consisted of removing each of the variables starting with the least sensitive until only two variables remained. The results were consistent with the full neural net algorithm. For more information about the systematic errors for the π^0 finding algorithm see Appendix C.

7.3.7 Monte Carlo modelling

The models used in the Monte Carlo generator can effect both the pion and kaon momentum and energy spectra. This effect can produce biases when determining the K^0 identification efficiency, the momentum dependent K/π separation and the π^0 identification. The dynamics of the $\pi^-\overline{\mathrm{K}}^0$ decay mode is well understood and it is generated by Tauola via the $\mathrm{K}^*(892)^-$ resonance. The $\mathrm{K}^-\mathrm{K}^0$ final state is generated by Tauola using phase space only.

As discussed in Chapter 5, the $\tau^- \to \pi^-\overline{\mathrm{K}}^0 \geq 1\pi^0\nu_\tau$ decay mode is composed of $\tau^- \to \pi^-\overline{\mathrm{K}}^0\pi^0\nu_\tau$ and $\tau^- \to \pi^-\overline{\mathrm{K}}^0\pi^0\pi^0\nu_\tau$ decays. The $\tau^- \to \pi^-\overline{\mathrm{K}}^0\pi^0\nu_\tau$ channel is modelled by Tauola assuming that the decay proceeds via the $\mathrm{K}_1(1400)$ resonance. Recent results from ALEPH [45], on one-prong τ decays with kaons, and OPAL [44], using $\tau^- \to \mathrm{K}^-\pi^-\pi^+\nu_\tau$ decays, suggest that the $\tau^- \to \pi^-\overline{\mathrm{K}}^0\pi^0\nu_\tau$ decay will also proceed via the $\mathrm{K}_1(1270)$ resonance. A special Monte Carlo simulation was generated in which the final state was created using the $\mathrm{K}_1(1270)$ and $\mathrm{K}_1(1400)$ resonances, using the algorithm developed for the analysis described in references [44,46]. The selection efficiency of the $\tau^- \to \pi^-\overline{\mathrm{K}}^0\pi^0\nu_\tau$ final state is estimated from the special Monte Carlo for both resonances. The efficiencies are found to agree at a level of 10% giving a systematic error of 0.00037.

The $\tau^- \to \pi^-\overline{\mathrm{K}}^0\pi^0\pi^0\nu_\tau$ decay mode is not modelled by Tauola. The branching ratio of this mode was recently measured to be $(0.26 \pm 0.24) \times 10^{-3}$ [54]. A special Monte Carlo sample of the $\tau^- \to \pi^-\overline{\mathrm{K}}^0\pi^0\pi^0\nu_\tau$ decay mode is generated using flat phase space [46] and it is found that the efficiency of this mode is within 30% of the efficiency of the $\tau^- \to \pi^-\overline{\mathrm{K}}^0\pi^0\nu_\tau$ decay mode. For the systematic uncertainty associated with this decay mode, 30% of the $\tau^- \to \pi^-\overline{\mathrm{K}}^0\pi^0\pi^0\nu_\tau$ branching ratio is used.

The $\tau^- \to K^- K^0 \geq 0\pi^0\nu_\tau$ decay mode is composed of $\tau^- \to K^- K^0 \pi^0 \nu_\tau$ and $\tau^- \to K^- K^0 \pi^0 \pi^0 \nu_\tau$ decays. The $\tau^- \to K^- K^0 \pi^0 \nu_\tau$ decay mode is generated by Tauola through a combination of the $\rho(1700)$ and $a_1(1260)$ resonances. A special Monte Carlo sample of these two modes was generated separately using the algorithm developed for the analysis described in [44,46]. The selection efficiencies of the $\tau^- \to K^- K^0 \pi^0 \nu_\tau$ decay mode is calculated for these two samples and are found to be equivalent within statistical error. No systematic uncertainty is included for this channel. The $\tau^- \to K^- K^0 \pi^0 \pi^0 \nu_\tau$ decay mode is not modelled by Tauola. The Particle Data Group [3, p. 286] give a limit of 0.18×10^{-3} for this channel. A special Monte Carlo sample of the $\tau^- \to K^- K^0 \pi^0 \pi^0 \nu_\tau$ decay mode is generated using flat phase space [46] and it is found that the efficiency of this mode is within 30% of the efficiency of the $\tau^- \to K^- K^0 \pi^0 \nu_\tau$ decay mode. For the systematic uncertainty associated with this decay mode, 30% of the $\tau^- \to K^- K^0 \pi^0 \nu_\tau$ branching ratio limit is used.

Finally, the $\tau^- \to K^- K^0 \geq 0\pi^0\nu_\tau$ selection efficiency may depend on the relative $\tau^- \to K^- K^0 \nu_\tau$ and $\tau^- \to K^- K^0 \pi^0 \nu_\tau$ branching ratios. Using the current world averages from [3, p. 286], the relative contribution of each channel is varied by ±25%. The branching ratio is observed to change by up to 0.00015 from the nominal value; this is included as a systematic error for this channel.

7.3.8 Additional checks

Potential detector-related systematic biases to the branching ratios were evaluated by comparing the branching ratio measurements obtained in different regions of the detector or with different detector requirements. The parity invariance of the detector was tested by comparing the branching ratios in the two hemispheres $(\cos\theta > 0)$ and $(\cos\theta < 0)$ of the detector. The charge dependence, and hence the invariance under

Selection	$\mathrm{K}^0_\mathrm{L} X^- \nu_\tau$	$\overline{\mathrm{K}}^0 \pi^- \nu_\tau$	$\overline{\mathrm{K}}^0 \pi^- \geq 1\pi^0 \nu_\tau$	$\mathrm{K}^0 \mathrm{K}^- \geq 0\pi^0 \nu_\tau$
Charge conjugation	± 0.12	± 0.28	± 0.30	± 0.08
Parity	± 0.49	± 0.15	± 0.17	± 0.27
$N^{\mathrm{hits}}_{\mathrm{d}E/\mathrm{d}x} > 80$	-0.11	-0.16	$+0.14$	-0.03
CZ acceptance	-0.32	-0.16	$+0.09$	$+0.05$
HCAL leakage	-0.11	-0.40	-0.39	$+0.40$

Table 7.5: The shift in the branching ratio measurements resulting from changes to the selection procedures ($\times 10^{-3}$).

the assumption of invariance under charge conjugation, was checked by comparing the branching ratios for τ^- and τ^+ decays. In both cases, the branching ratio variations were within the statistical errors. These results were shown in Table 7.5. The effect of the dE/dx quality requirement of at least 40 wires was tested by increasing the threshold to 80 wires per track. This change was found to have a negligible effect on the branching ratio measurements.

The CZ detector has two small regions, corresponding to about 7% of the geometrical acceptance, which were inoperative for part of the data collection period. The τ Monte Carlo modelled these regions as if they were inoperative for the entire data collection period, leading to a slight difference in CZ acceptance between data and Monte Carlo. This may lead to differences in the calibration of the dE/dx, since non-gaussian effects may be present in the data without CZ hits. The sensitivity of the branching ratio determination to the Monte Carlo modelling of this effect was evaluated by recalculating the branching ratios excluding any decays that pass through an inoperative region of the CZ detector.

The energy calibration of the hadron calorimeter does not take into account the leakage of energy out the back. This leakage may change the energy calibration of those decays not fully contained. Figure 7.3 shows the number of decays that have

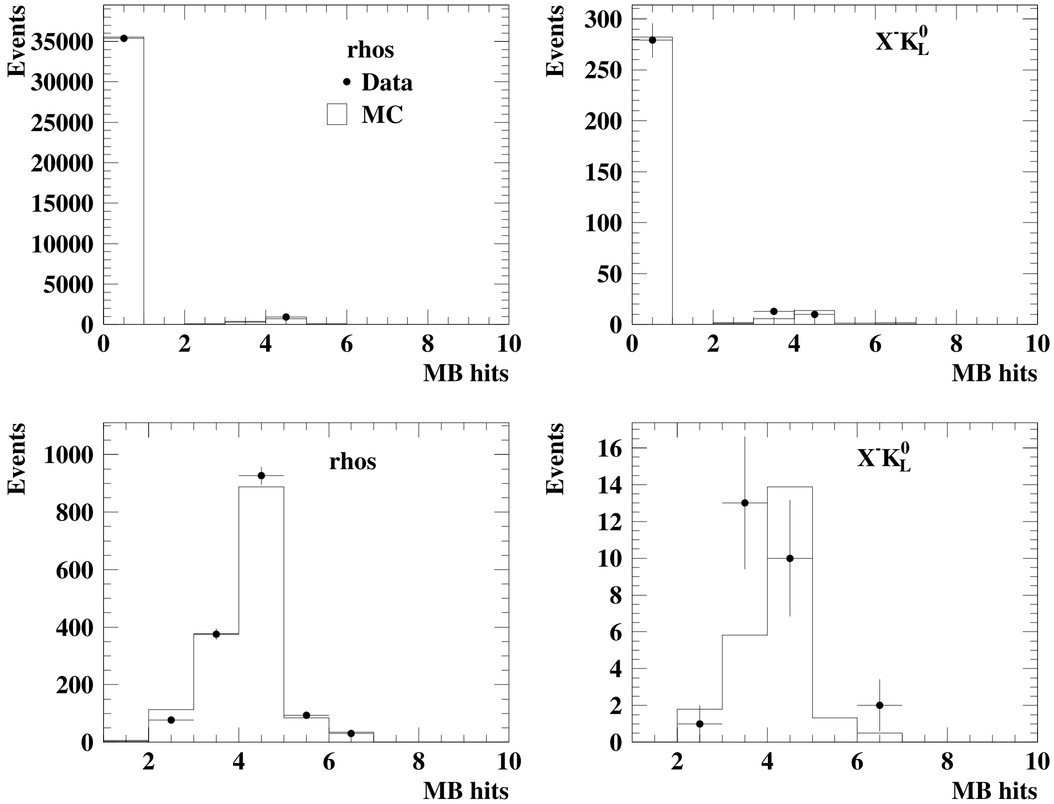

Figure 7.3: The number of muon chamber hits for tau decays into rho and $X^-\mathrm{K}^0_\mathrm{L}$ final states. The top plots show all the decays while the bottom plots only show those decays that have muon chamber hits.

muon hits for tau decays into rho mesons and $X^-\mathrm{K}^0_\mathrm{L}$ final states. These plots show that approximately 4% of rho final states are not contained while about 8% of $X^-\mathrm{K}^0_\mathrm{L}$ final states have muon hits. To check the calibration of the hadron calorimeter, tau decays to rho mesons that have muon chamber hits are studied. The top plot in Figure 7.4 shows E_HB/p versus p for data and Monte Carlo, while the bottom plot shows the ratio of the data to Monte Carlo. It is observed that even if the decay is not completely stopped by the hadron calorimeter the total energy deposited by the

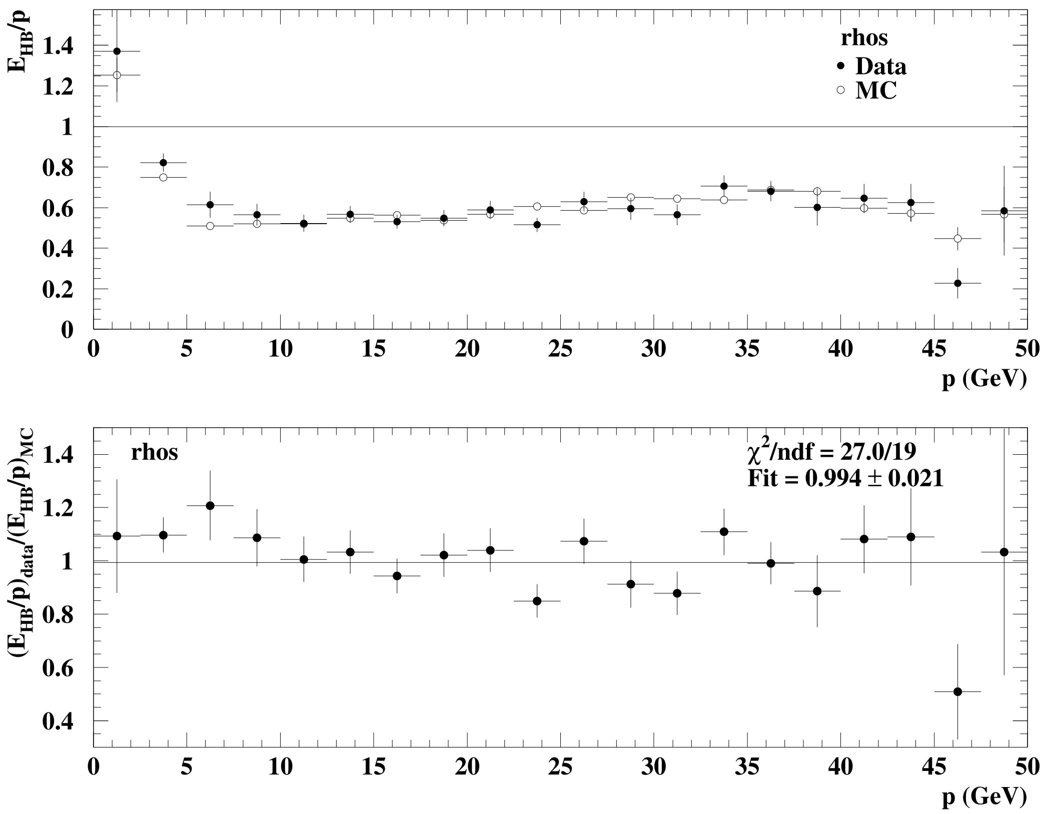

Figure 7.4: E_{HB}/p versus p and $(E_{HB}/p)_{data}/(E_{HB}/p)_{MC}$ versus p for rho decays where muon hits are required. The points in the second plot are fit to a flat distribution.

decay is well described by the Monte Carlo. To check the sensitivity of the branching ratios to this effect, the branching ratios are recalculated requiring that each decay be stopped by the hadron calorimeter (ie. the decay does not have any muon hits).

As a final check on the calibration of the hadron calorimeter, the significance factor S_{HB} is plotted for samples of $\tau^- \to \mathrm{K}^-\nu_\tau$ and $\tau^+ \to \mathrm{K}^+\overline{\nu}_\tau$ decays to check the response of the hadron calorimeter to strangeness enhanced hadronic showers (see Figure 7.5). The selection uses the algorithm outlined in Appendix A and uses the $\mathrm{d}E/\mathrm{d}x$ separation procedure described in Chapter 6 for the $X^-\mathrm{K}^0_{\mathrm{L}}$ analysis. Both

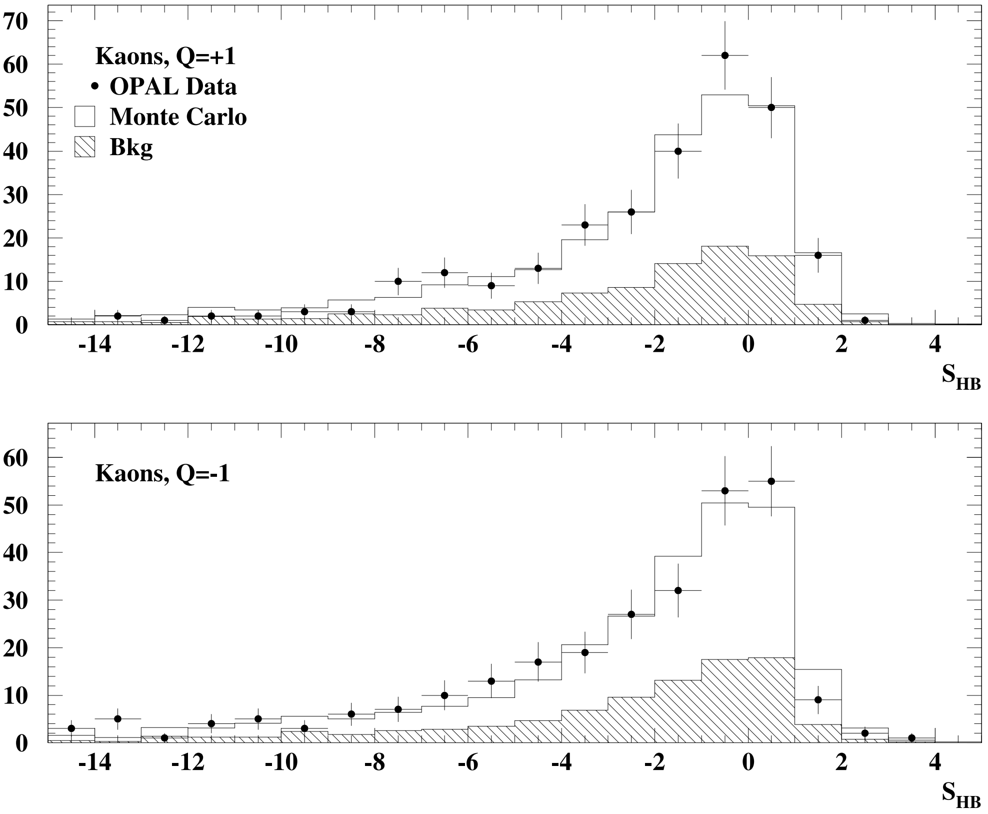

Figure 7.5: The significance factor S_{HB} for $\tau^+ \to \mathrm{K}^+\overline{\nu}_\tau$ (top plot) and $\tau^- \to \mathrm{K}^-\nu_\tau$ (bottom plot) decays. The hatched region shows the background decays.

plots show good agreement between the data and Monte Carlo.

Chapter 8

Discussion

The inclusive $\tau^- \to X^-\mathrm{K^0_L}\nu_\tau$ branching ratio was measured to be $(10.01 \pm 0.79 \pm 0.64) \times 10^{-3}$, where the first error is statistical and the second is systematic. Recalling that the $\mathrm{K^0}$ ($\overline{\mathrm{K}}{}^0$) meson can be composed of 50% $\mathrm{K^0_L}$ and 50% $\mathrm{K^0_S}$ mesons, the branching ratios of both the $\tau^- \to X^-\mathrm{K^0_L}\nu_\tau$ and $\tau^- \to X^-\mathrm{K^0_S}\nu_\tau$ decay modes are expected to be equal. Figure 8.1 shows that the $\tau^- \to X^-\mathrm{K^0_L}\nu_\tau$ branching ratio result is in agreement with the published results [56,57] involving the $\mathrm{K^0_S}$ meson. The solid band on the plot is the average of the two previous results involving the $\mathrm{K^0_S}$ meson and is 9.70 ± 0.67.

The $\tau^- \to \pi^-\overline{\mathrm{K}}{}^0\nu_\tau$ branching ratio includes both the $\mathrm{K^0_L}$ and $\mathrm{K^0_S}$ mesons, as do the remaining exclusive decay modes. The branching ratio of this mode was measured to be $(9.1 \pm 0.9 \pm 0.6) \times 10^{-3}$ and is in good agreement with the analogous OPAL branching ratio measurement involving the $\mathrm{K^0_S}$ meson of $(9.6 \pm 1.0 \pm 0.7) \times 10^{-3}$ [58] and the world average of $(8.64 \pm 0.42) \times 10^{-3}$. Figure 8.2(a) shows these results and other experimental results [45, 56, 57, 59] and theoretical predictions. The analyses are labelled with either $\mathrm{K^0_L}$ or $\mathrm{K^0_S}$ depending upon the primary component in the decay. The theoretical predictions of the $\tau^- \to \pi^-\overline{\mathrm{K}}{}^0\nu_\tau$ branching ratio have been estimated by several authors in recent years. For example, Finkemeier and

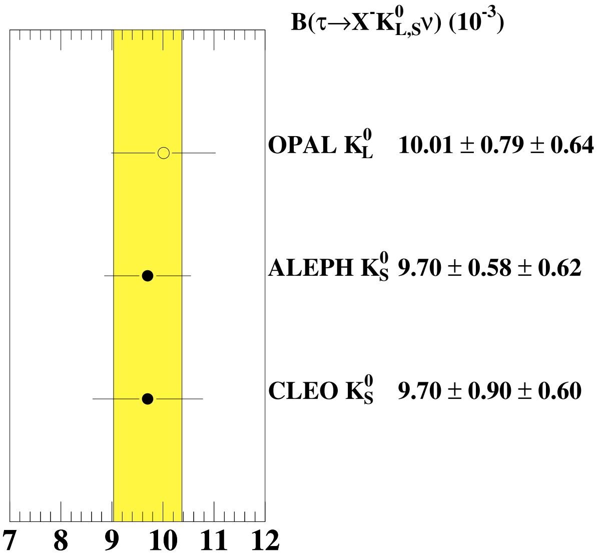

Figure 8.1: Branching ratios of the $\tau^- \to X^-\mathrm{K}^0_\mathrm{L}\nu_\tau$ and $\tau^- \to X^-\mathrm{K}^0_\mathrm{S}\nu_\tau$ decay modes measured to date. The solid band is the average branching ratio of the two previous measurements.

Mirkes [13] calculate the hadronic matrix element, $\mathcal{M}$, in terms of form factors which are predicted using low-energy effective Lagrangians using $SU(3)_L \times SU(3)_R$ chiral symmetry, supplemented by information about any possible low-lying resonances in the different channels. They also take the isospin symmetry relations into account. Braaten, Oakes and Tse [14] use a similar approach to predict the tau semi-leptonic branching ratios. They use a $U(3) \times U(3)$ chiral symmetry and take into account symmetry breaking effects by using the measured value of the meson masses in calculating phase space and the vector meson propagators. Finkemeier and Mirkes [13] predict that the branching ratio is in the range of $(6.6 - 9.6) \times 10^{-3}$ while Braaten *et al.* [14] predict a range of $(8.9 - 10.3) \times 10^{-3}$. Both predictions agree with the new OPAL result and are shown on the last two rows of Figure 8.2(a).

It is known that the $\tau^- \to \pi^-\overline{\mathrm{K}}^0\nu_\tau$ decay mode is dominated by the $\mathrm{K}^*(892)^-$ resonance. This can be observed from the $\overline{\mathrm{K}}^0\pi^-$ invariant mass distribution shown

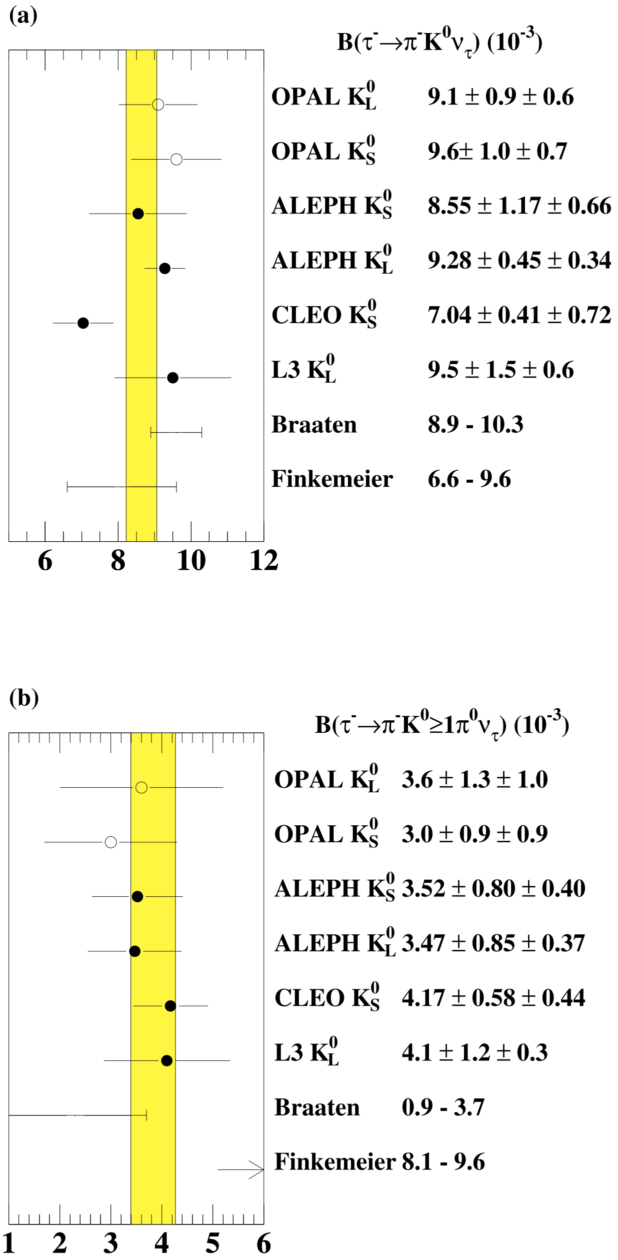

Figure 8.2: Branching ratios of the $\tau^- \rightarrow \pi^- \overline{\mathrm{K}}^0 \nu_\tau$ and $\tau^- \rightarrow \pi^- \overline{\mathrm{K}}^0 \geq 1\pi^0 \nu_\tau$ decays measured and predicted to date. The solid band is the average branching ratio of the previous measurements. The $\tau^- \rightarrow \pi^- \overline{\mathrm{K}}^0 \geq 1\pi^0 \nu_\tau$ results include both the $\tau^- \rightarrow \pi^- \overline{\mathrm{K}}^0 \pi^0 \nu_\tau$ and $\tau^- \rightarrow \pi^- \overline{\mathrm{K}}^0 \pi^0 \pi^0 \nu_\tau$ measurements. The theoretical estimates are shown for the $\tau^- \rightarrow \pi^- \overline{\mathrm{K}}^0 \pi^0 \nu_\tau$ decay mode only. The open points show the new OPAL results, the solid points show other experimental results and the bounded region shows the theoretical predictions of the branching fractions.

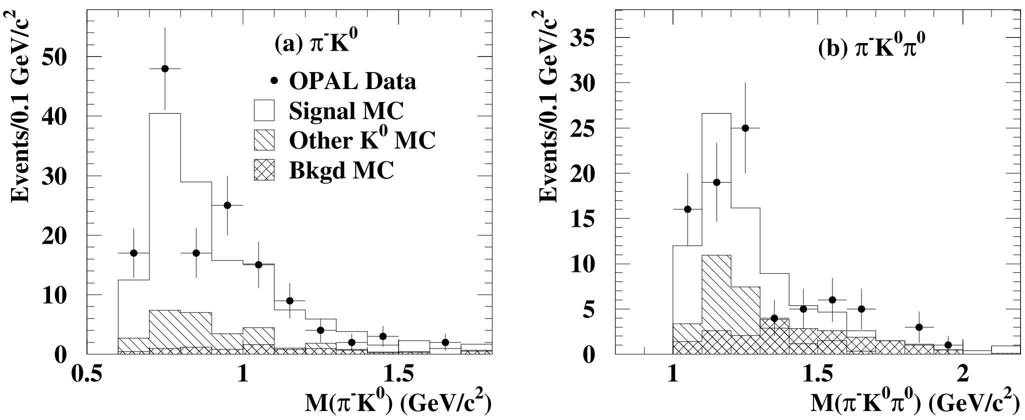

Figure 8.3: The jet mass is plotted for the data and Monte Carlo for the $\tau^- \to \pi^-\overline{\mathrm{K}}^0\nu_\tau$ and $\tau^- \to \pi^-\overline{\mathrm{K}}^0 \geq 1\pi^0\nu_\tau$ decay modes. Each mass plot assumes that the charged track is a pion. Histogram (a) shows the invariant mass of the $\pi^-\overline{\mathrm{K}}^0$ mesons from the $\tau^- \to \pi^-\overline{\mathrm{K}}^0\nu_\tau$ decay. Histogram (b) shows the invariant mass of the $\pi^-\overline{\mathrm{K}}^0\pi^0$ system from the $\tau^- \to \pi^-\overline{\mathrm{K}}^0\nu_\tau$ decay.

in Figure 8.3(a). The data agree with the Monte Carlo simulation which assumes that this channel proceeds through the K*(892)$^-$ resonance. Using the $\tau^- \to \pi^-\overline{\mathrm{K}}^0\nu_\tau$ branching ratio measured in this analysis and isospin conservation,[1] an estimate of the $\tau^- \to \mathrm{K}^*(892)^-\nu_\tau$ branching ratio is calculated, giving

$$B(\tau^- \to \mathrm{K}^*(892)^-\nu_\tau) = 0.0137 \pm 0.0016. \qquad (8.1)$$

The analogous OPAL result involving primarily K^0_S final states give 0.00144 ± 0.0018 [58]. Finally, the combined OPAL result, including both the K^0_L and K^0_S studies is

$$B(\tau^- \to \mathrm{K}^*(892)^-\nu_\tau) = 0.0140 \pm 0.0013. \qquad (8.2)$$

This value is consistent with the current world average 0.0128 ± 0.0008 [3, p. 286].

---

[1] Recall that the isospin conservation relation for the K*(892)$^-$ decay is $|\mathrm{K}^{*-}\rangle = \sqrt{1/3}|\mathrm{K}^-\pi^0\rangle - \sqrt{2/3}|\mathrm{K}^0\pi^-\rangle$.

The decay constant of the $\tau^- \to \mathrm{K}^*(892)^-\nu_\tau$ decay, f_{K^*}, is estimated using equation 2.15:

$$f_{\mathrm{K}^*} = \frac{8\pi}{G_F V_{\mathrm{us}} m_\tau^{3/2}} \left(1 - \frac{m_{\mathrm{K}^*}^2}{m_\tau^2}\right)^{-1} \left(1 + \frac{2m_{\mathrm{K}^*}^2}{m_\tau^2}\right)^{-1/2} \sqrt{\frac{B(\tau^- \to \mathrm{K}^*(892)^-\nu_\tau)}{T_\tau}}. \quad (8.3)$$

Inserting the branching ratio of the $\tau^- \to \mathrm{K}^*(892)^-\nu_\tau$ decay into this equation gives $f_{\mathrm{K}^*} = 799.8 \pm 14.2 \pm 38.0$ MeV, where the first error comes from the uncertainty on V_{us} and the second error comes from the uncertainty on the branching ratio.

Predictions of the decay constant f_{K^*} using various theoretical models have been made. These models predict the f_{K^*} decay constant by relating it to the f_ρ decay constant using sum rule relations between the spectral functions based on assumptions of $SU(3)_f$ symmetry derived by Oneda [16] using a set of sum rules originally derived by Das, Mathur and Okubo (DMO) [17]. At the flavour-$SU(3)_f$ symmetry limit ($m_{\mathrm{u}} = m_{\mathrm{d}} = m_{\mathrm{s}}$), the decay constant ratio is unity $f_{\mathrm{K}^*} = f_\rho$. If asymptotic $SU(3)_f$ symmetry becomes exact at high q^2 where its breaking can be explained by the production of few resonances at low mass one estimates [16]

$$\frac{f_\rho}{f_{\mathrm{K}^*}} = \frac{m_\rho}{m_{\mathrm{K}^*}} = 0.86. \quad (8.4)$$

Recalling equation 2.17, the ratio of the decay constants, f_ρ/f_{K^*}, can be determined using the decay widths of the $\tau^- \to \rho^-\nu_\tau$ decay with respect to the $\tau^- \to \mathrm{K}^*(892)^-\nu_\tau$ decay:

$$\frac{f_\rho}{f_{\mathrm{K}^*}} = \tan\theta_c \sqrt{\frac{B(\tau^- \to \rho^-\nu_\tau)}{B(\tau^- \to \mathrm{K}^*(892)^-\nu_\tau)}} \left(\frac{m_\tau^2 - m_{\mathrm{K}^*}^2}{m_\tau^2 - m_\rho^2}\right) \sqrt{\frac{m_\tau^2 + 2m_{\mathrm{K}^*}^2}{m_\tau^2 + 2m_\rho^2}}. \quad (8.5)$$

To estimate this ratio, the OPAL measurement of the branching ratio of the $\tau^- \to h^-\pi^0\nu_\tau$ decay mode is used, $B(\tau^- \to h^-\pi^0\nu_\tau) = 0.2589 \pm 0.0034$ [49]. The $\tau^- \to h^-\pi^0\nu_\tau$ decay mode is the sum of the decay modes $\tau^- \to \pi^-\pi^0\nu_\tau$ and $\tau^- \to \mathrm{K}^-\pi^0\nu_\tau$.

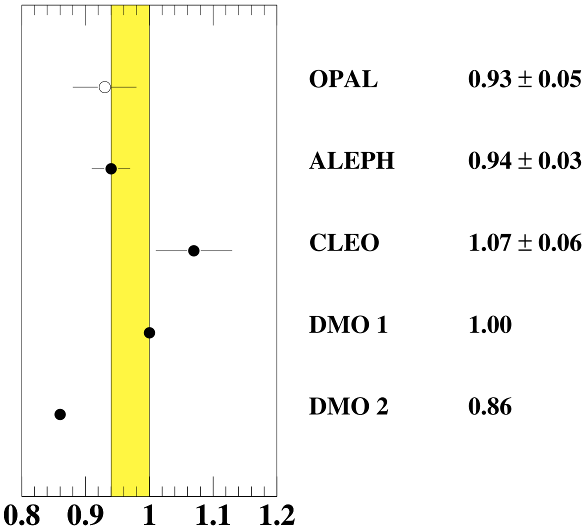

Figure 8.4: Decay constant ratios f_ρ/f_{K^*} using results from tau decays and the DMO sum rules [17]. The first DMO result uses the assumption that the flavour-$SU(3)_f$ symmetry limit is reached while the second ratio assumes asymptotic flavour-$SU(3)_f$ symmetry. The solid band in the average of the previous measured decay constant ratios.

The branching ratio of the $\tau^- \to \mathrm{K}^-\pi^0\nu_\tau$ decay mode can be calculated using isospin conservation from the $\tau^- \to \pi^-\overline{\mathrm{K}}^0\nu_\tau$ branching ratio giving $(4.67 \pm 0.42) \times 10^{-3}$; consequently the branching fraction of the $\tau^- \to \pi^-\pi^0\nu_\tau$ decay mode is estimated to be 0.2543 ± 0.0034. Using the Cabibbo angle θ_c and the particle masses from [3, p. 103, 286, 364 and 472], the decay constant ratio is

$$\frac{f_\rho}{f_{\mathrm{K}^*}} = 0.93 \pm 0.05. \tag{8.6}$$

Figure 8.4 shows this measurement together with other measurements of the decay constant ratio [45, 57]. This result does not indicate which theoretical assumption is better.

The $\tau^- \to \pi^-\overline{\mathrm{K}}^0 \geq 1\pi^0\nu_\tau$ branching ratio was measured to be $(3.3\pm0.9\pm0.7)\times10^{-3}$

and is shown in Figure 8.2(b) in comparison with other measurements. The result is in good agreement with the world average of $(3.83 \pm 0.45) \times 10^{-3}$. If one assumes that the decay only contains one π^0 meson, then the decay can be compared to theoretical predictions. Note that the current branching ratio of the $\tau^- \to \pi^- \overline{\mathrm{K}}^0 \pi^0 \pi^0 \nu_\tau$ is measured to be only $(0.26 \pm 0.24) \times 10^{-3}$ [54]. Finkemeier and Mirkes predict that the branching ratio will be in the range of $(0.81 - 0.96) \times 10^{-3}$ [13] and Braaten *et al.* predict a range of $(0.9 - 3.7) \times 10^{-3}$ [14]. The $\tau^- \to \pi^- \overline{\mathrm{K}}^0 \pi^0 \nu_\tau$ branching ratio by Finkemeier and Mirkes is significantly higher than the experimental results, however they argue that the widths of the K_1 resonance [3, p. 474] used in their calculation are unusually narrow and that increasing the K_1 width would give a prediction that agrees with the experimental measurements [60]. The invariant mass of the $\tau^- \to \pi^- \overline{\mathrm{K}}^0 \geq 1\pi^0 \nu_\tau$ system is plotted in Figure 8.3(b).

The $\tau^- \to \mathrm{K}^- \mathrm{K}^0 \geq 0\pi^0 \nu_\tau$ branching fraction was measured to be $(3.3 \pm 0.9 \pm 0.7) \times 10^{-3}$. Figure 8.5 shows this measurement in comparison with other recent results. The results shown are the sum of the $\tau^- \to \mathrm{K}^- \mathrm{K}^0 \nu_\tau$, $\tau^- \to \mathrm{K}^- \mathrm{K}^0 \pi^0 \nu_\tau$ and $\tau^- \to \mathrm{K}^- \mathrm{K}^0 \pi^0 \pi^0 \nu_\tau$ branching ratios for the experimental results. The results from this study agree well with the world average branching ratio of $(3.08 \pm 0.42) \times 10^{-3}$. The theoretical predictions are the sum of the $\tau^- \to \mathrm{K}^- \mathrm{K}^0 \nu_\tau$ and $\tau^- \to \mathrm{K}^- \mathrm{K}^0 \pi^0 \nu_\tau$ branching ratios, since no predictions of the $\tau^- \to \mathrm{K}^- \mathrm{K}^0 \pi^0 \pi^0 \nu_\tau$ decay mode have been made. The current upper limit of the $\tau^- \to \mathrm{K}^- \mathrm{K}^0 \pi^0 \pi^0 \nu_\tau$ branching ratio is 0.18×10^{-3} [3, p. 286]. Finkemeier and Mirkes predict the branching ratio should be in the range of $(2.3 - 2.7) \times 10^{-3}$ [13] while Braaten *et al.* predict a range of $(2.4 - 4.0) \times 10^{-3}$ [14]. Predictions of the $\tau^- \to \mathrm{K}^- \mathrm{K}^0 \nu_\tau$ decay mode are possible using the charge vector current (CVC) hypothesis [61] using low energy $\mathrm{e}^+\mathrm{e}^- \to \pi^+\pi^-$ data scaled by a kinematic factor to take into account the $\pi - \mathrm{K}$ mass difference, estimates

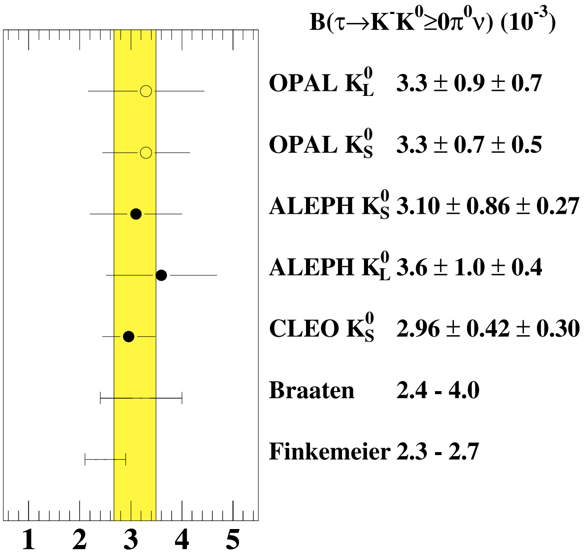

Figure 8.5: Branching ratios of the $\tau^- \to \mathrm{K}^-\mathrm{K}^0 \geq 0\pi^0\nu_\tau$ decay mode measured and predicted to date. The solid band is the average branching ratio of the previous measurements. The $\tau^- \to \mathrm{K}^-\mathrm{K}^0 \geq 0\pi^0\nu_\tau$ results are the sum of the $\tau^- \to \mathrm{K}^-\mathrm{K}^0\nu_\tau$, $\tau^- \to \mathrm{K}^-\mathrm{K}^0\pi^0\nu_\tau$ and $\tau^- \to \mathrm{K}^-\mathrm{K}^0\pi^0\pi^0\nu_\tau$ decays. There are no theoretical predictions for the $\tau^- \to \mathrm{K}^-\mathrm{K}^0\pi^0\pi^0\nu_\tau$ decay mode. The open points show the new OPAL results, the solid points other experimental results and the bounded lines show two theoretically predicted ranges of the branching fractions.

of $(1.1 \pm 0.3) \times 10^{-3}$ [62] and $(1.6 \pm 0.2) \times 10^{-3}$ are obtained. These predictions are approximately one-half of the $\tau^- \to \mathrm{K}^-\mathrm{K}^0 \geq 0\pi^0\nu_\tau$ branching ratio as expected.

Chapter 9

Conclusion

This dissertation presents evidence for the first observation of the $\mathrm{K^0_L}$ meson using data collected between 1991 and 1995 with the OPAL detector at LEP. Using this observation, the first OPAL measurement of a branching ratio of the τ lepton decaying into a final state containing at least one $\mathrm{K^0_L}$ meson was made. The branching ratio for the inclusive τ decay to the $\mathrm{K^0_L}$ meson is measured to be:

$$B(\tau^- \to X^- \mathrm{K^0_L} \nu_\tau) = (10.01 \pm 0.79 \pm 0.64) \times 10^{-3},$$

where X^- represents a π^- or K^- meson accompanied by any number of neutral mesons. The first error is statistical and the second is systematic. This is the first inclusive measurement using the OPAL detector of the τ decaying into a $\mathrm{K^0_L}$ meson.

The decays from the inclusive selection are then subjected to additional criteria to identify the particles accompanying the $\mathrm{K^0_L}$ meson. These criteria identify three exclusive decay modes: $\tau^- \to \pi^- \overline{\mathrm{K}}^0 \nu_\tau$, $\tau^- \to \pi^- \overline{\mathrm{K}}^0 \geq 1\pi^0 \nu_\tau$, and $\tau^- \to \mathrm{K}^- \mathrm{K}^0 \geq 0\pi^0 \nu_\tau$. The branching ratios of these modes are measured to be

$$\begin{array}{lcl} B(\tau^- \to \pi^- \overline{\mathrm{K}}^0 \nu_\tau) & = & (9.1 \pm 0.9 \pm 0.6) \times 10^{-3}, \\ B(\tau^- \to \pi^- \overline{\mathrm{K}}^0 \geq 1\pi^0 \nu_\tau) & = & (3.6 \pm 1.3 \pm 1.0) \times 10^{-3}, \\ B(\tau^- \to \mathrm{K}^- \mathrm{K}^0 \geq 0\pi^0 \nu_\tau) & = & (3.3 \pm 0.9 \pm 0.7) \times 10^{-3}, \end{array}$$

where the first error is statistical and the second is systematic. The exclusive decays include $\mathrm{K^0_L}$ mesons and a small component of $\mathrm{K^0_S}$ mesons which have a sufficient lifetime to remain in the selected sample. These exclusive branching ratios are the first OPAL measurements involving τ decays into $\mathrm{K_L^0}$ mesons.

The branching ratio of the $\tau^- \to \pi^- \overline{\mathrm{K}}^0 \nu_\tau$ decay mode and isospin conservation of the $\mathrm{K^*(892)}$ meson were subsequently used to calculate the branching ratio of the $\tau^- \to \mathrm{K^*(892)}^- \nu_\tau$ decay, giving $B(\tau^- \to \mathrm{K^*(892)}^- \nu_\tau) = 0.0140 \pm 0.0013$. This result is in good agreement with other current results.

Finally, using the branching ratio of the $\tau^- \to \mathrm{K^*(892)}^- \nu_\tau$ decay mode calculated in this analysis, the ratio of the $\rho(770)$ decay constant, f_ρ, to the $\mathrm{K^*(892)}$ decay constant, $f_{\mathrm{K^*}}$, was measured to be $f_\rho/f_{\mathrm{K^*}} = 0.93 \pm 0.05$. This ratio was predicted using the DMO sum rules to have two different values depending upon the theoretical model used, either $f_\rho/f_{\mathrm{K^*}} = 1.0$ or $f_\rho/f_{\mathrm{K^*}} = 0.86$. The ratio measured in this analysis is consistent with either theoretical prediction.

Appendix A

HCAL Significance Factor

A new variable called the significance factor and denoted by S_{HB}, was created to help select K^0_L candidates from τ decays. This variable is defined as

$$S_{\mathrm{HB}} = \frac{E_{\mathrm{HB}} - p}{\sigma_{\mathrm{HB}}}, \tag{A.1}$$

where E_{HB} is the total energy deposited in the hadron calorimeter (HCAL) for the jet, p is the momentum of the charged track and σ_{HB} is the hadron calorimeter energy resolution. The first section describes the Monte Carlo simulation of E_{HB} and the second section describes the measurement of the HCAL resolution.

A.1 Monte Carlo Simulation of the HCAL

The Monte Carlo simulation of the hadron calorimeter energy, E_{HB}, is studied to ensure that the Monte Carlo agrees well with the data. The HCAL energy of the Monte Carlo was studied using isolated hadrons that leave a small amount of energy in the electromagnetic calorimeter through ionization and consequently leave almost all of their energy in the hadronic calorimeter. These hadrons will be referred to as minimum ionizing pions (mips) throughout the remainder of this Appendix. The mips used in this study of S_{HB} come from the $\tau^- \to \pi^- \nu_\tau$ decay. Each decay is required to be within the barrel region of the OPAL detector, $|\cos\theta| < 68°$, to ensure that the HCAL energy is well measured. Each decay is required to have a presampler multiplicity, the sum of hits in the presampler, less than 4 and to have only one track accompanied by one cluster in the electromagnetic calorimeter with an energy less than 1.5 GeV. The decays were required to have a difference in the azimuthal angle between the track and presampler cluster farthest away from the track to be less than 0.5°. To reject electrons, the electromagnetic cluster energy divided by the momentum was required to be less than 0.8. Finally, to remove muons, the $\tau^- \to h^-\nu_\tau$ candidates were not allowed to have any hits in the muon chambers.

The Monte Carlo simulation was checked using tau decays into pion and rho meson final states. The $\tau^- \to \pi^-\nu_\tau$ decays were selected as above without the electromagnetic calorimeter requirement. The $\tau^- \to \rho^-\nu_\tau$ decays were selected following the algorithm described in [63], which selected decays within the barrel region of the OPAL detector. Each decay was allowed to have only one track and up to three clusters in the electromagnetic calorimeter in which two of the clusters are not associated with the track. The energy of the cluster closest to the track divided by the momentum was required to be less than 0.9 and the neutral clusters were required to deposit at least 1.2 GeV of energy in the electromagnetic calorimeter. Finally, the mass of the reconstructed π^0 meson had to be less than 0.28 GeV to be consistent with the true π^0 mass.

The momentum and hadron calorimeter energy for the mips in each jet is shown in Figure A.1. Plot (a) shows that the momentum is well modelled by the Monte Carlo, whereas plot (b) shows some discrepancies between the Monte Carlo and data for the hadron calorimeter energy (E_{HB}). To explore this discrepancy further, a profile histogram of E_{HB}/p is shown in Figure A.2. Figure A.2 shows that the Monte

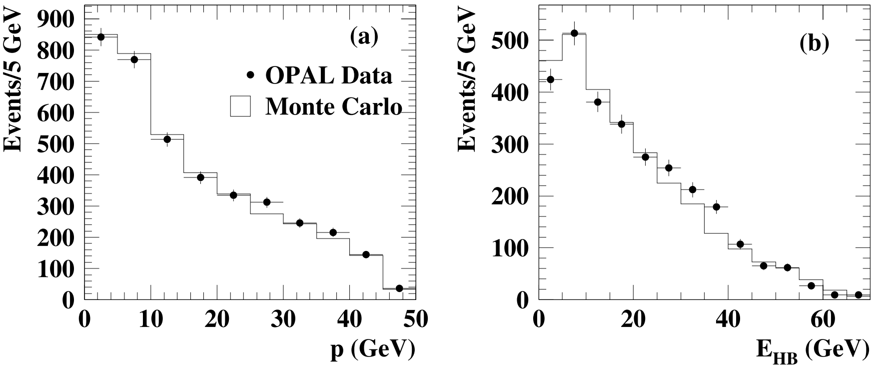

Figure A.1: (a) shows the momentum and (b) shows the hadron calorimeter energy for mips with $E_{\mathrm{EB}} < 1.5$ GeV.

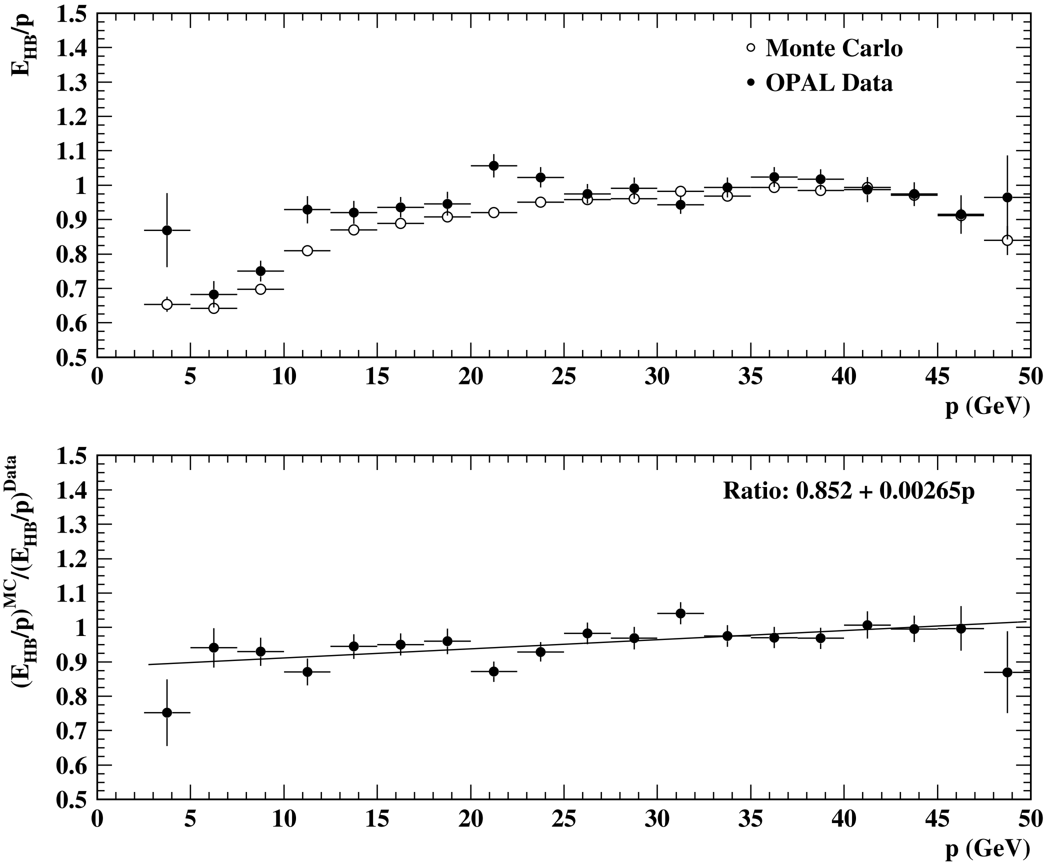

Figure A.2: Hadron calorimeter energy study for mips. The top plot shows the ratio E_{HB}/p for mips. The bottom plot shows the ratio between the data and Monte Carlo.

Carlo underestimates the hadron calorimeter energy by up to 5%, and is momentum dependent. To correct the Monte Carlo, a ratio of the Monte Carlo and data profile histograms is computed, giving a correction factor of

$$\frac{(E_{\mathrm{HB}}/p)^{\mathrm{MC}}}{(E_{\mathrm{HB}}/p)^{\mathrm{Data}}} = 0.852 + 0.00265\,p. \tag{A.2}$$

To check the Monte Carlo simulation of E_{HB} after it has been corrected, the ratio of E_{HB}/p is plotted as a function of p for tau decays into mips, pion and rho meson final states in Figure A.3 for data and Monte Carlo. The ratio of $(E_{\mathrm{HB}}/p)^{\mathrm{Data}}$ for the data to $(E_{\mathrm{HB}}/p)^{\mathrm{MC}}$ for the Monte Carlo is plotted for the three selections in Figure A.4. If the modelling of the HCAL energy is adequate, then $(E_{HB}/p)^{\mathrm{Data}}/(E_{HB}/p)^{\mathrm{MC}}$ should be unity. Indeed, in all three cases the ratios of ratios are approximately one. The uncertainties on the fits suggest that the Monte Carlo simulates HCAL energy to better than 1.5% for the three selections. The χ^2 per degree of freedom, shown on the plots, is close to unity for all three samples.

With the components of S_{HB} checked for consistency, S_{HB} is plotted to ensure that the Monte Carlo agrees with the data. Figure A.5(a) shows S_{HB} for the mips sample that was used to correct E_{HB}, while Figure A.5(b) shows a similar plot for the $\tau^- \to \rho^- \nu_\tau$ decays. The dotted line in both plots shows the Monte Carlo E_{HB} before it was corrected while the solid line gives the energy after it has been corrected. It can be observed that the corrected Monte Carlo agrees well with the data for the two control samples; the χ^2 difference between the data and Monte Carlo is shown on the plots.

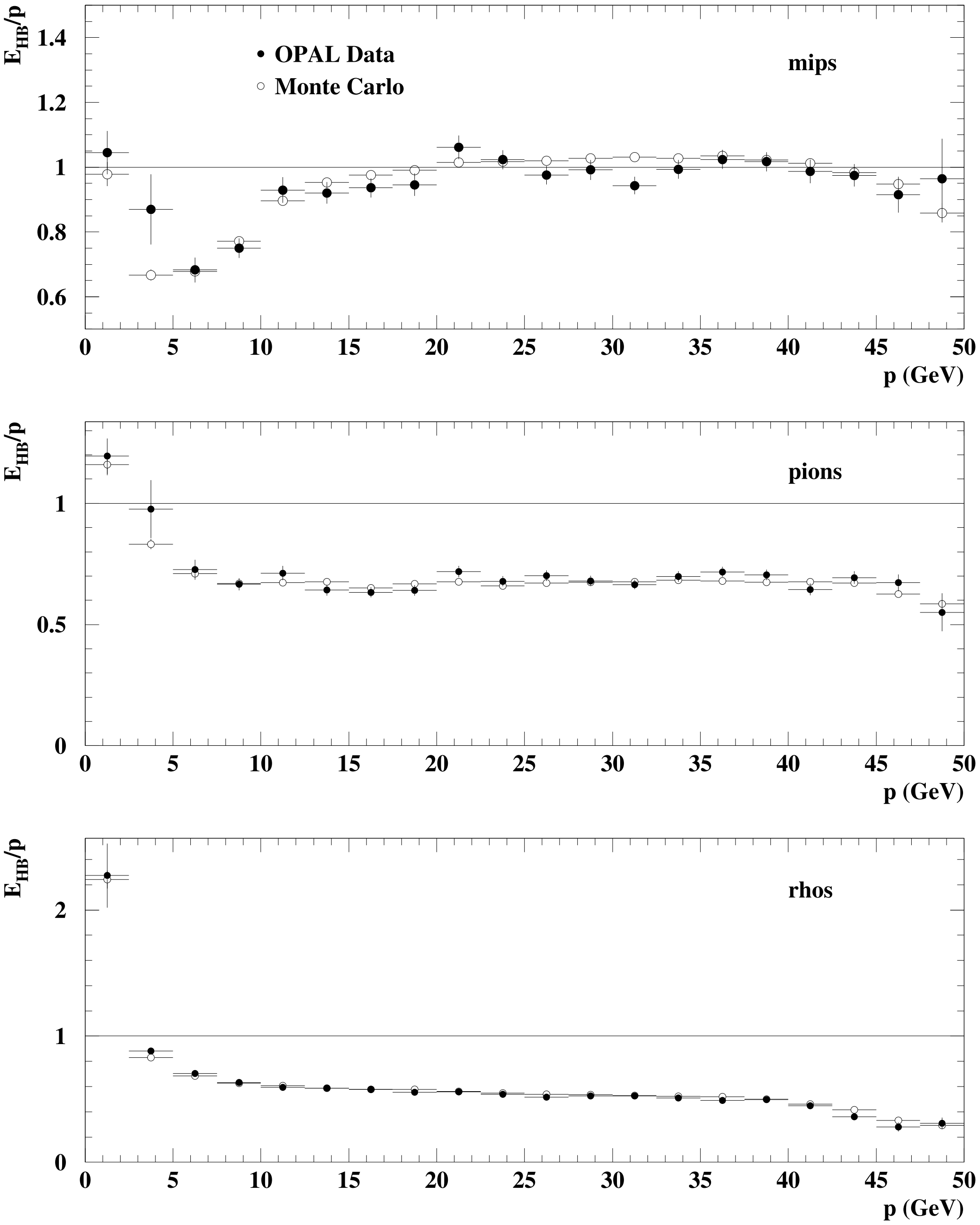

Figure A.3: E_{HB}/p versus p for mips, pion and rho mesons after the Monte Carlo is corrected.

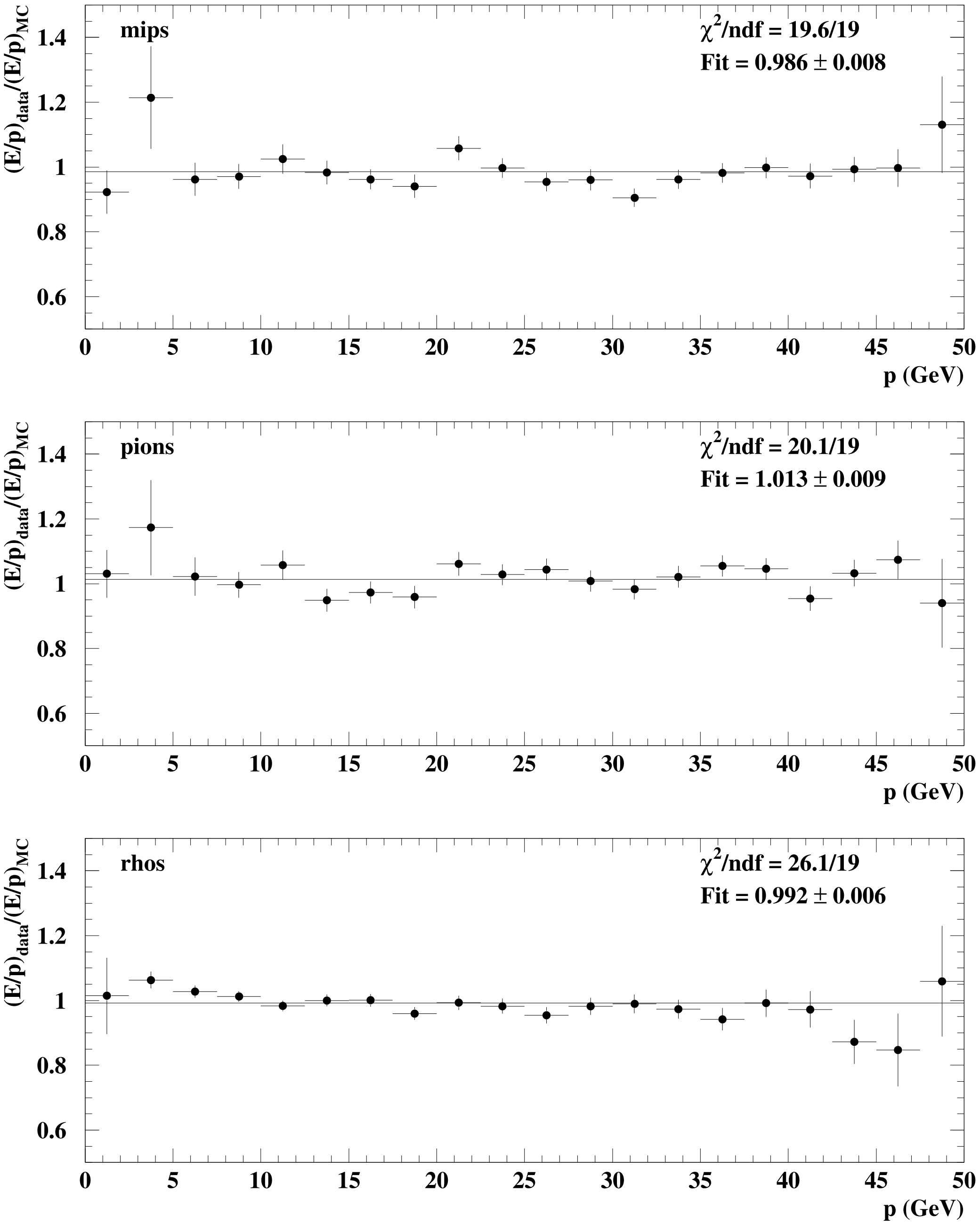

Figure A.4: $(E_{HB}/p)^{\mathrm{Data}}/(E_{HB}/p)^{\mathrm{MC}}$ versus p for mips, pion and rho mesons. The fit values are given for the ratios and the χ^2 of the fits are also shown.

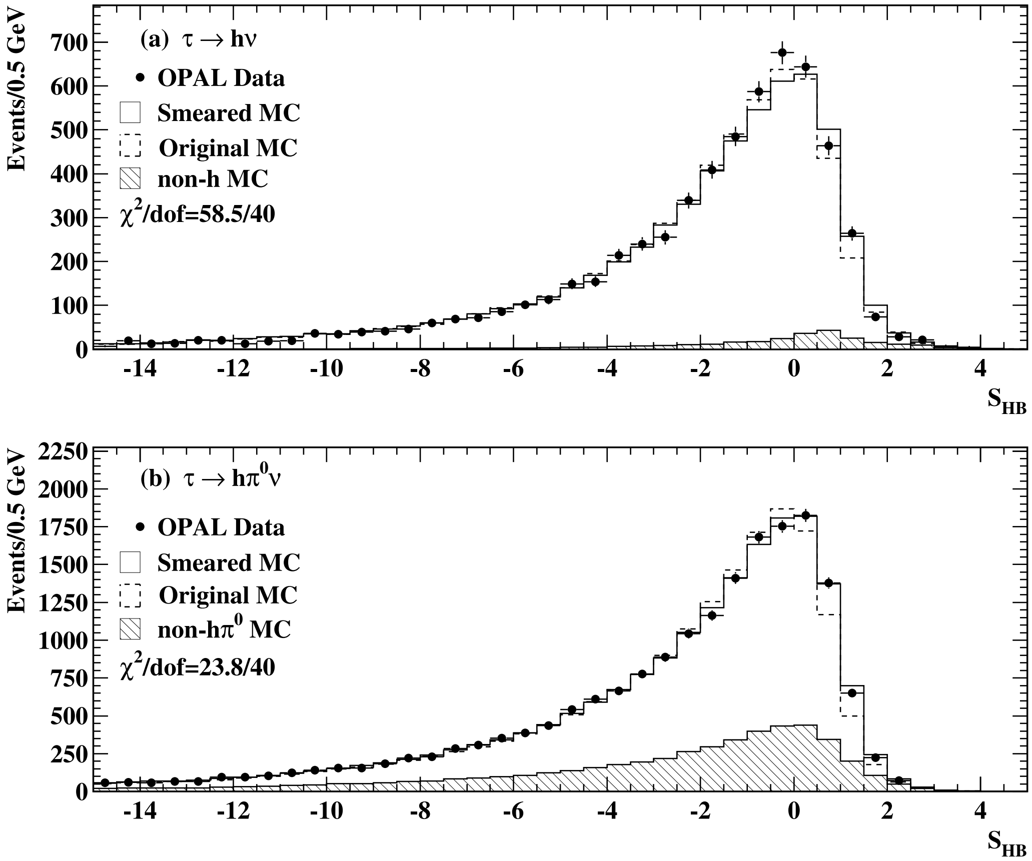

Figure A.5: $S_{\rm HB}$ for the mips and $\tau^- \to \rho^- \nu_\tau$ decays. The solid line histogram is the corrected Monte Carlo, the dashed histogram is the uncorrected Monte Carlo, the points are the data and the shaded areas are background in the two control samples. The χ^2 difference between the data and Monte Carlo is shown for both decays.

A.2 $E_{\rm HB}$ Resolution

The finite resolution of the hadron calorimeter limits the precision of the reconstructed hadron calorimeter energy. The resolution of the hadronic calorimeter was studied using the minimum ionizing pions selected in Appendix A.1. An analogous study of the resolution was also conducted on the $\tau^+\tau^-$ Monte Carlo sample used in this analysis.

The resolution is measured by comparing the difference between the measured energy (E_{HB}) and the incident energy (p) of the isolated hadrons. The resulting energy resolution, $\sigma_{\mathrm{HB}}/E_{\mathrm{HB}}$, follows the expected $A + B/\sqrt{E}$ form [33], where the constant term includes the sampling and shower fluctuations of the hadron calorimeter and the energy dependent term includes the detector response imperfections and noise. It should also be noted that in principle the width of the distributions is a function of both the momentum and the energy. This can be written as $\sigma^2_{\mathrm{HB}-p} = \sigma^2_{\mathrm{HB}} + \sigma^2_p$. However $\sigma_{\mathrm{HB}} \gg \sigma_p$, thus $\sigma_{\mathrm{HB}-p}$ can be approximated as σ_{HB}.

The actual resolution of the hadron calorimeter is estimated by comparing the difference between the incident energy and the energy deposited in the hadron calorimeter in eight momentum bins between 2 and 50 GeV. Figure A.6 shows the $E_{\mathrm{HB}} - p$ distributions for each momentum bin for the data and Monte Carlo. Each plot is fitted with a gaussian distribution to calculate the mean and the width of the peaks. The gaussian fits are performed within $\pm 2\sigma$ of the mean to reduce the effects of the non-gaussian tails. The means of the $E_{\mathrm{HB}} - p$ distributions may not be exactly zero as expected since the momentum distributions may not be uniform within the bin range. The means and widths of the eight distributions are listed in Table A.1 for the data and Monte Carlo.

Figure A.7 shows the plot of σ/E versus E for the data (filled dots) and Monte Carlo (open dots) with $E = E_{\mathrm{bin}} + \delta E$, where E_{bin} is given by the midpoint of each bin and δE is the shift in the mean from zero of the gaussian fit to the $E_{\mathrm{HB}} - p$ peak as given in Table A.1. The plot shows the expected $A + B/\sqrt{E}$ behaviour. The measured resolution of the hadron calorimeter from the data is $(0.165 \pm 0.024) + (0.847 \pm 0.100)/\sqrt{E}$. The resolution of the Monte Carlo is $(0.204 \pm 0.023) + (0.696 \pm 0.097)/\sqrt{E}$. It is observed that the data agree with the Monte Carlo within statistical errors on the fits, consequently the same resolution function is applied to both the data and Monte Carlo.

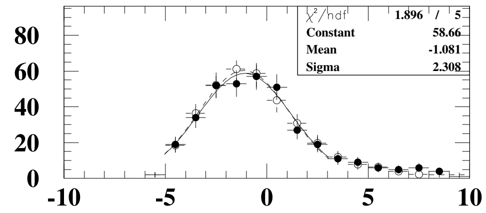

(E-p) 2-7.5

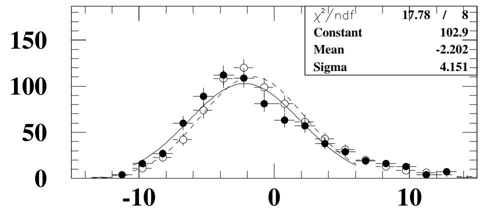

(E-p) 7.5-15

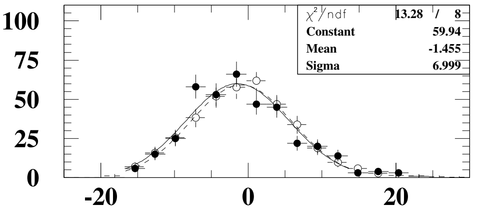

(E-p) 15-20

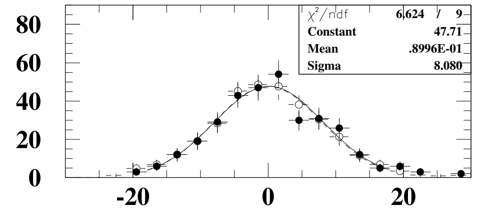

(E-p) 20-25

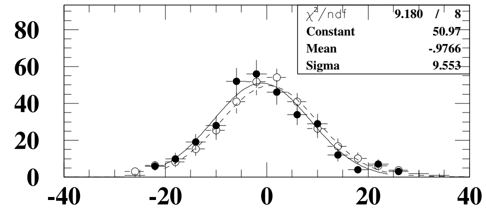

(E-p) 25-30

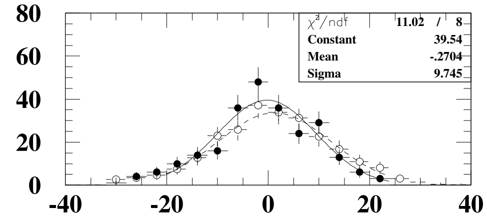

(E-p) 30-35

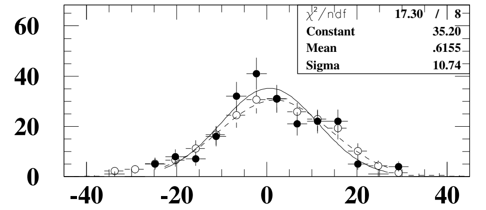

(E-p) 35-40

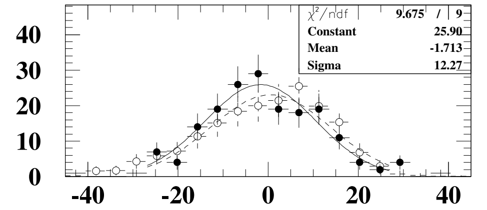

(E-p) 40-50

Figure A.6: The $E_{\mathrm{HB}} - \mathrm{p}$ resolution spectra for the 1991-1995 data plotted (filled dots and solid line) and Monte Carlo (open dots and dashed line). The distributions are fit with gaussians around $\pm 2\sigma$ of the mean. The statistics shown in the legend are for the data only.

Bin Range (GeV)	Data		Monte Carlo	
	Mean (δE)	Width (σ)	Mean (δE)	Width (σ)
2.0-7.5	-1.08 ± 0.16	2.31 ± 0.18	-1.12 ± 0.16	2.27 ± 0.17
7.5-15.0	-2.20 ± 0.18	4.15 ± 0.18	-1.59 ± 0.16	3.86 ± 0.15
15.0-20.0	-1.46 ± 0.40	7.00 ± 0.36	-0.97 ± 0.40	6.86 ± 0.35
20.0-25.0	0.10 ± 0.50	8.08 ± 0.44	-0.04 ± 0.49	8.00 ± 0.43
25.0-30.0	-0.98 ± 0.61	9.55 ± 0.52	0.48 ± 0.61	9.58 ± 0.53
30.0-35.0	-0.27 ± 0.70	9.75 ± 0.61	1.23 ± 0.85	11.12 ± 0.83
35.0-40.0	0.62 ± 0.81	10.74 ± 0.70	1.85 ± 0.97	12.16 ± 0.93
40.0-50.0	-1.71 ± 1.03	12.27 ± 0.92	0.51 ± 1.17	13.22 ± 1.11

Table A.1: Fitting parameters of the $E_{\mathrm{HB}} - p$ distribution for the 1991-1995 OPAL data and Monte Carlo

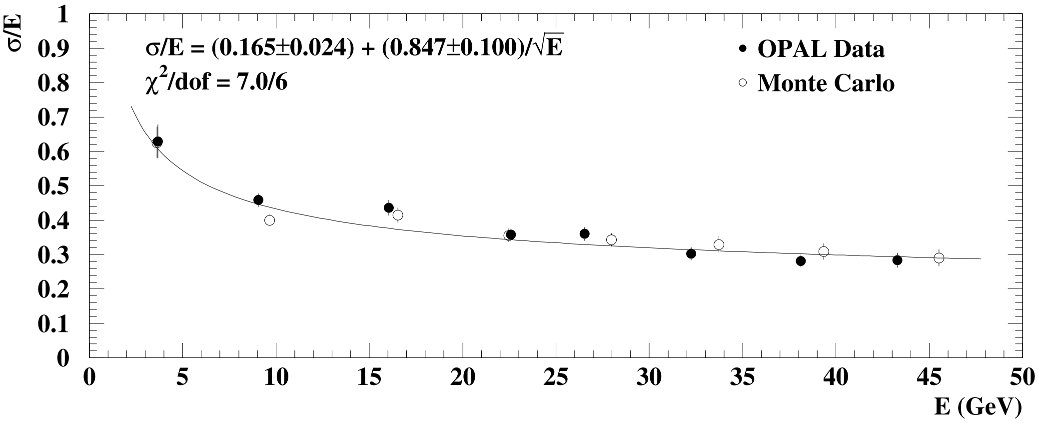

Figure A.7: The HCAL energy resolution. The plot shows σ/E versus E. The resolution for the data are shown using the filled dots while the Monte Carlo is shown with the open dots and the error bars give the statistical uncertainty for each measurement.

Appendix B

$\mathrm{d}E/\mathrm{d}x$ Modelling

Using the energy loss to distinguish pions from kaons requires an accurate $\mathrm{d}E/\mathrm{d}x$ parameterisation. This appendix checks the parameterisation of the Monte Carlo with respect to the data and computes any correction factors that may be required to improve the Monte Carlo modelling. The $\mathrm{d}E/\mathrm{d}x$ modelling was studied using τ one-prong hadronic decays. These decays were selected by requiring one charged track, the hadronic energy measured in the hadron calorimeter to be no less than 2.5 GeV and no hits in the muon chambers. These last two requirements remove nearly all of the leptonic tau decays. The normalised $\mathrm{d}E/\mathrm{d}x$, $N(\mathrm{d}E/\mathrm{d}x)$, is plotted in bins of $-\ln(1-\beta_\pi^2)$, where $\beta_\pi = p/E$ and $E^2 = p^2 + m_\pi^2$ for the pion hypothesis. The binning parameter comes directly from the first term inside the parenthesis of equation 4.1. Any differences observed between the means and widths of the $N(\mathrm{d}E/\mathrm{d}x)$ distributions for the data and Monte Carlo are corrected and the results are shown.

Figures B.1 and B.2 show the $N(\mathrm{d}E/\mathrm{d}x)$ distributions for the pion hypothesis. The plots on the left show the Monte Carlo distributions while the plots on the right show the data distributions. Similarly, Figures B.3 and B.4 show the $N(\mathrm{d}E/\mathrm{d}x)$ distributions for the kaon hypothesis. The distributions are fit with gaussians around approximately $\pm 2\sigma$ of the mean to reduce some of the effects of the non-gaussian tails. These tails are due to the charged kaon component in the τ one-prong hadronic decays which makes up approximately 5% of the one-prong sample. The presence of these charged kaons results in high χ^2 values per degree of freedom (dof) in some of the distributions. The resulting fits have 18 dof, except for the top plots in Figure B.3 which have 28 dof. For the 95% (99%) confidence level, the fits should have $\chi^2 \leq 29$ (42) for 18 dof and $\chi^2 \leq 41$ (48) for 28 dof [52]. Approximately half of the distributions satisfy these requirements at the 95% confidence level while 85% of the distributions satisfy these requirements at the 99% confidence level.

In order to check the calibration of the data by the Monte Carlo, the difference in the means of the data and Monte Carlo from the $N(\mathrm{d}E/\mathrm{d}x)$ distributions for the pion and kaon hypotheses are plotted as a function of $-\ln(1-\beta_\pi^2)$ in Figure B.5. The plots show that the difference is independent of $-\ln(1-\beta_\pi^2)$ up to 8.5 ($p = 20$ GeV). Above 8.5, a β_π dependent correction is required. The $N(\mathrm{d}E/\mathrm{d}x)$ offsets for the pion distributions are:

$$\begin{array}{lll}\text{if } -\ln(1-\beta_\pi^2) < 8.5 & \text{then} & -0.0687 \pm 0.0143 \\ \text{if } -\ln(1-\beta_\pi^2) > 8.5 & \text{then} & (-0.82 \pm 0.13) + (0.088 \pm 0.013)(-\ln(1-\beta_\pi^2)).\end{array}$$

Similarly, the $N(\mathrm{d}E/\mathrm{d}x)$ offsets for the kaon distributions are:

$$\begin{array}{lll}\text{if } -\ln(1-\beta_\pi^2) < 8.5 & \text{then} & -0.2345 \pm 0.0172 \\ \text{if } -\ln(1-\beta_\pi^2) > 8.5 & \text{then} & (-1.343 \pm 0.0172) + (0.133 \pm 0.015)(-\ln(1-\beta_\pi^2)).\end{array}$$

The resolutions of the $N(\mathrm{d}E/\mathrm{d}x)$ distributions are plotted versus $-\ln(1-\beta_\pi^2)$ in the left-hand plots in Figure B.6 for the pion and kaon hypotheses. The filled points show the data resolutions while the open points show the Monte Carlo resolutions. The right-hand plots show the ratio of the resolutions of the data with respect to the

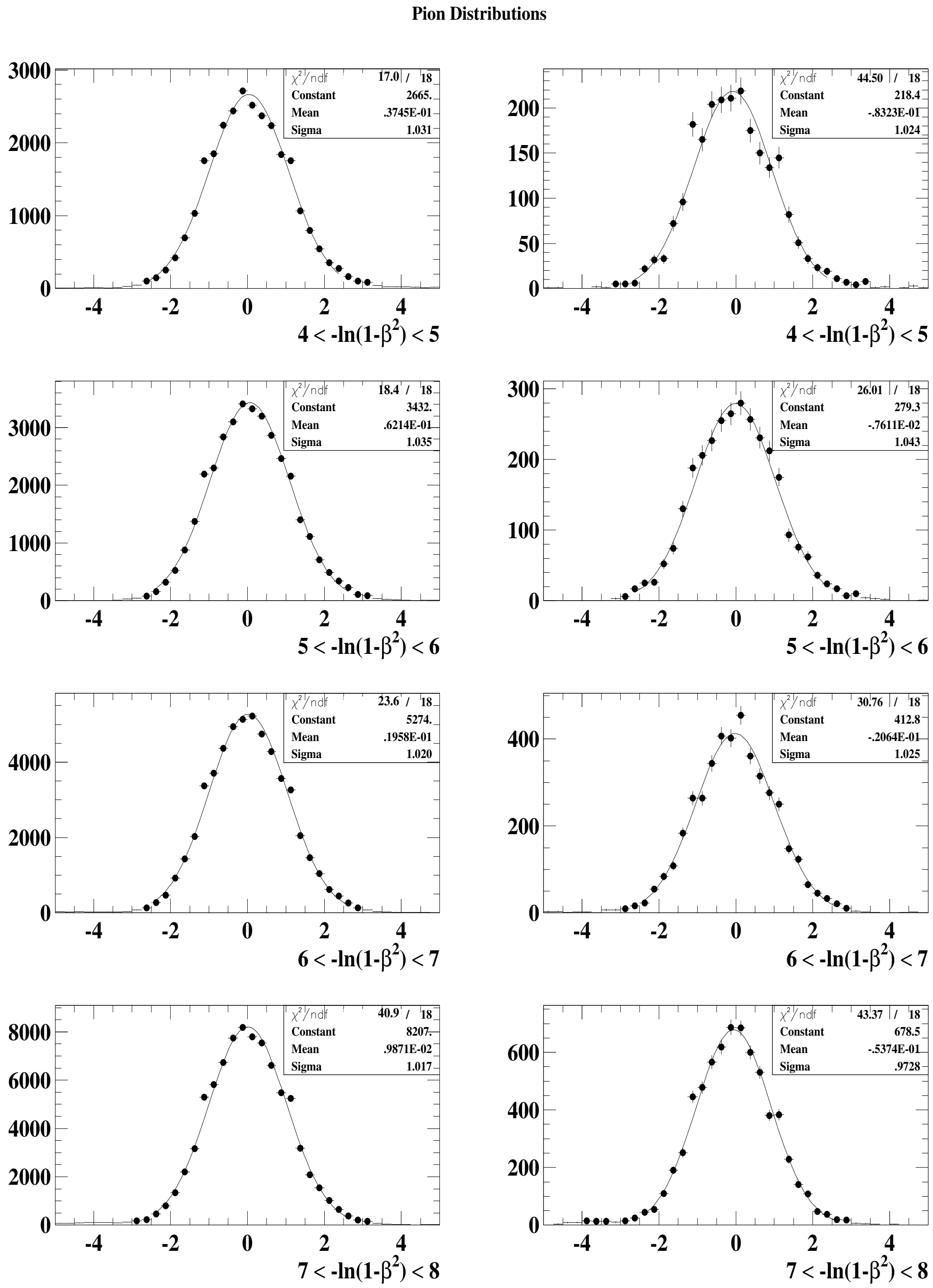

Figure B.1: The $N(\mathrm{d}E/\mathrm{d}x)_\pi$ distributions for the tau one-prong hadronic decays. The Monte Carlo plots are on the left and the data distributions are on the right. The legend gives the χ^2 and the gaussian fit parameters.

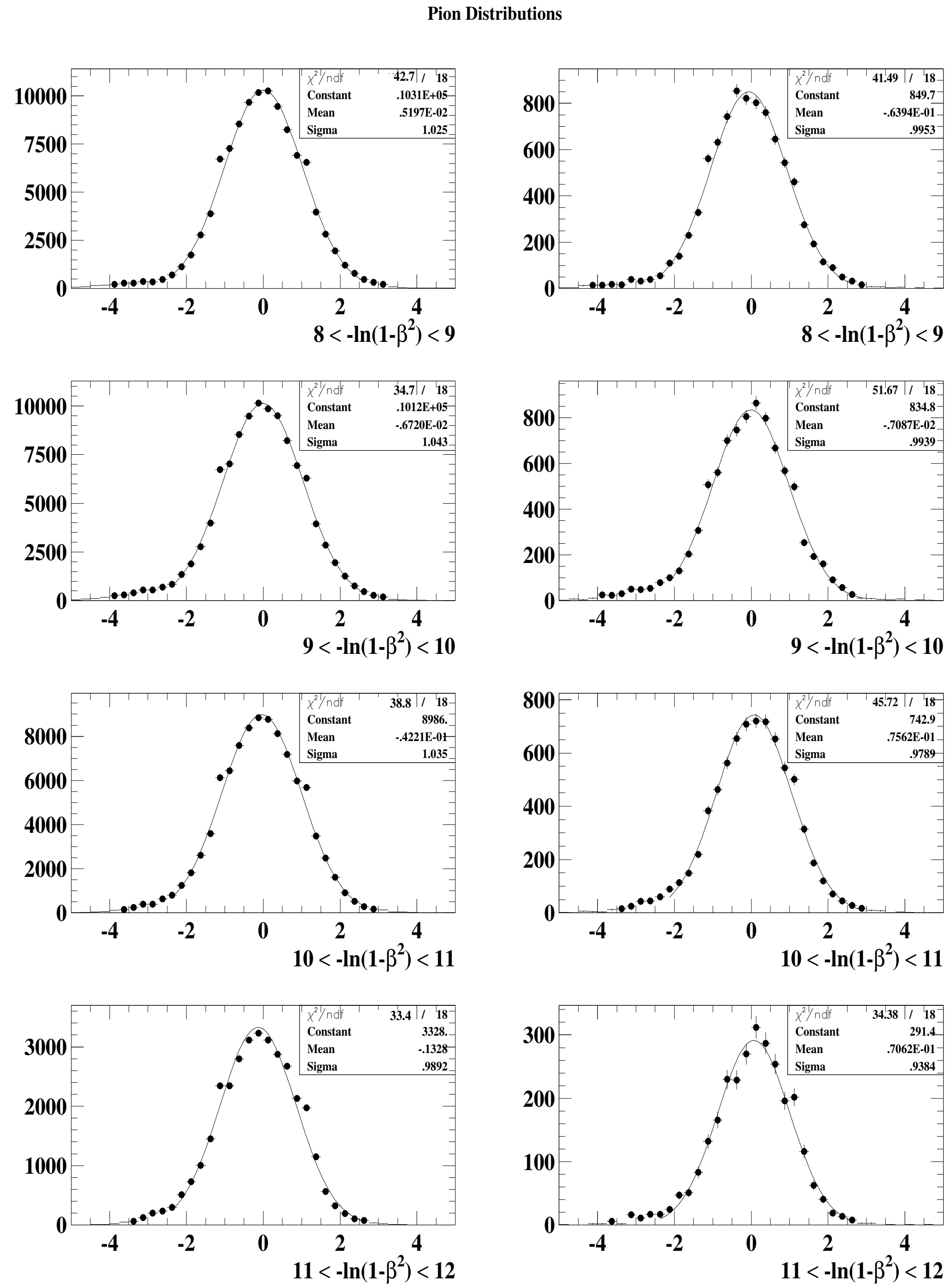

Figure B.2: The $N(\mathrm{d}E/\mathrm{d}x)_\pi$ distributions for the tau one-prong hadronic decays (continued). The Monte Carlo plots are on the left and the data distributions are on the right. The legend gives the χ^2 and the gaussian fit parameters.

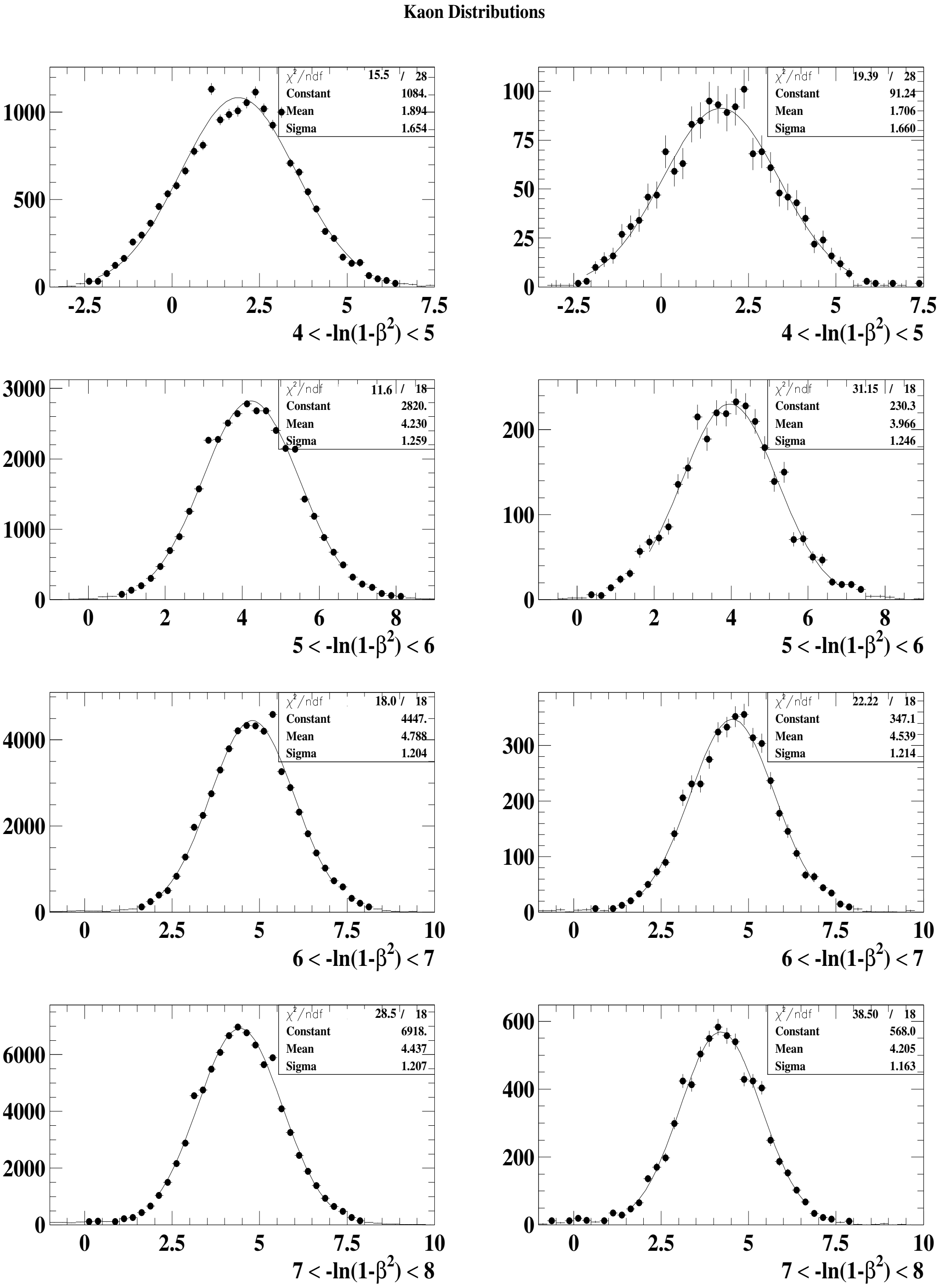

Figure B.3: The $N(\mathrm{d}E/\mathrm{d}x)_{\mathrm{K}}$ distributions for the tau one-prong hadronic decays. The Monte Carlo plots are on the left and the data distributions are on the right. The legend gives the χ^2 and the gaussian fit parameters.

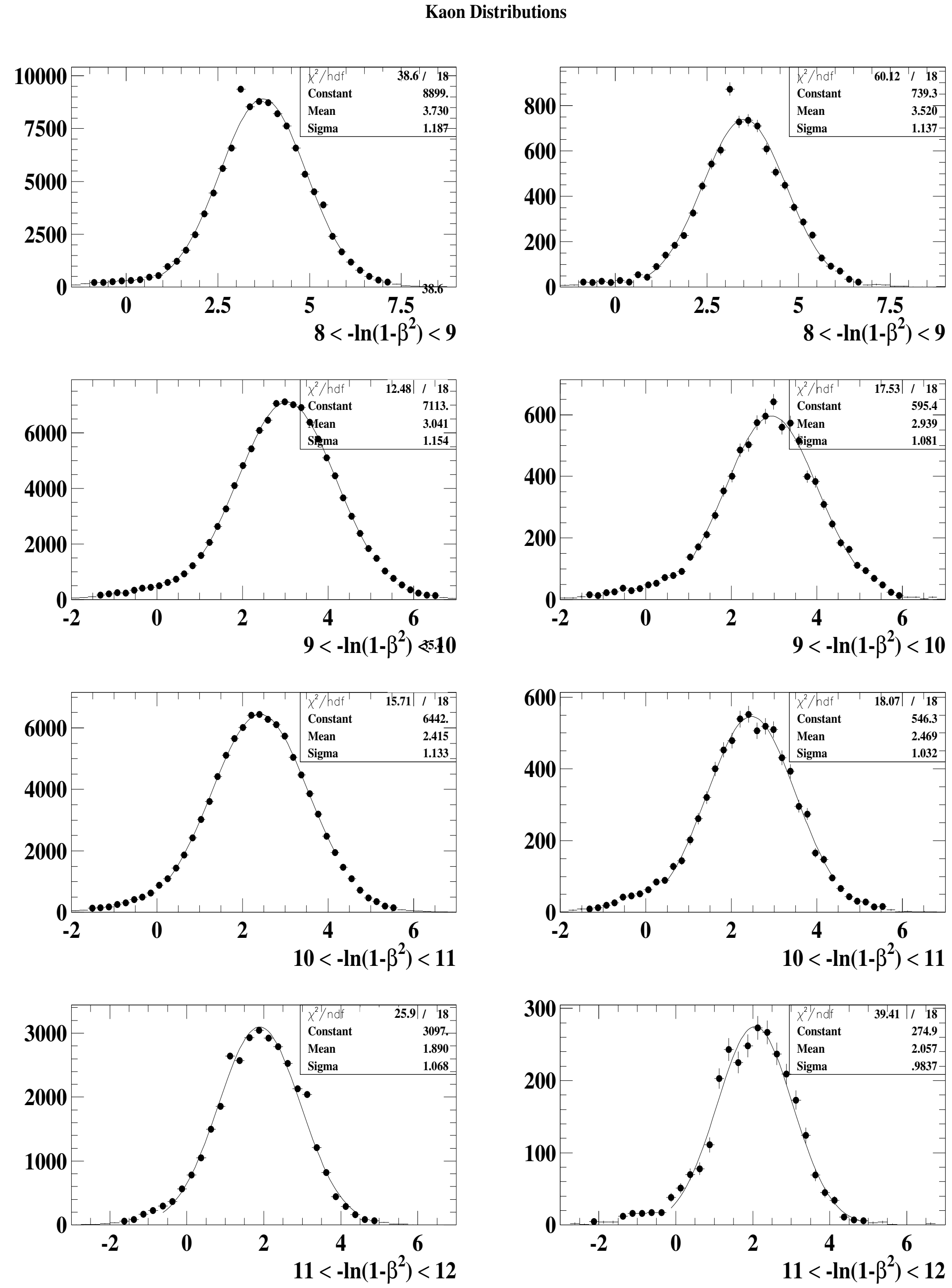

Figure B.4: The $N(\mathrm{d}E/\mathrm{d}x)_\mathrm{K}$ distributions for the tau one-prong hadronic decays (continued). The Monte Carlo plots are on the left and the data distributions are on the right. The legend gives the χ^2 and the gaussian fit parameters.

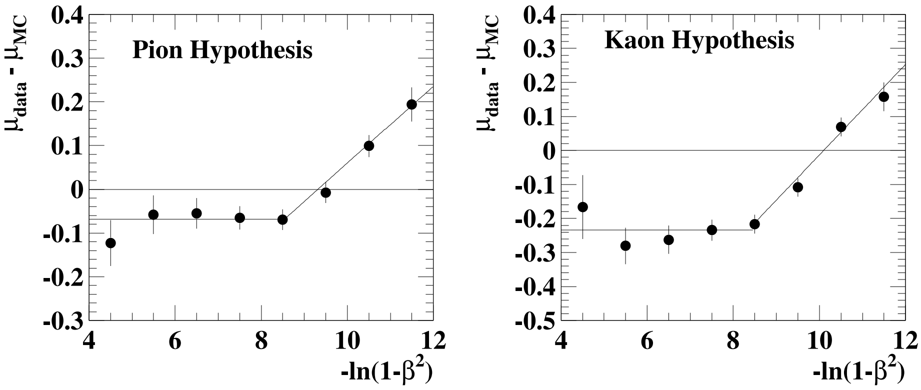

Figure B.5: The difference between the means of the data and Monte Carlo from the $N(\mathrm{d}E/\mathrm{d}x)$ distributions versus $-\ln(1-\beta_\pi^2)$.

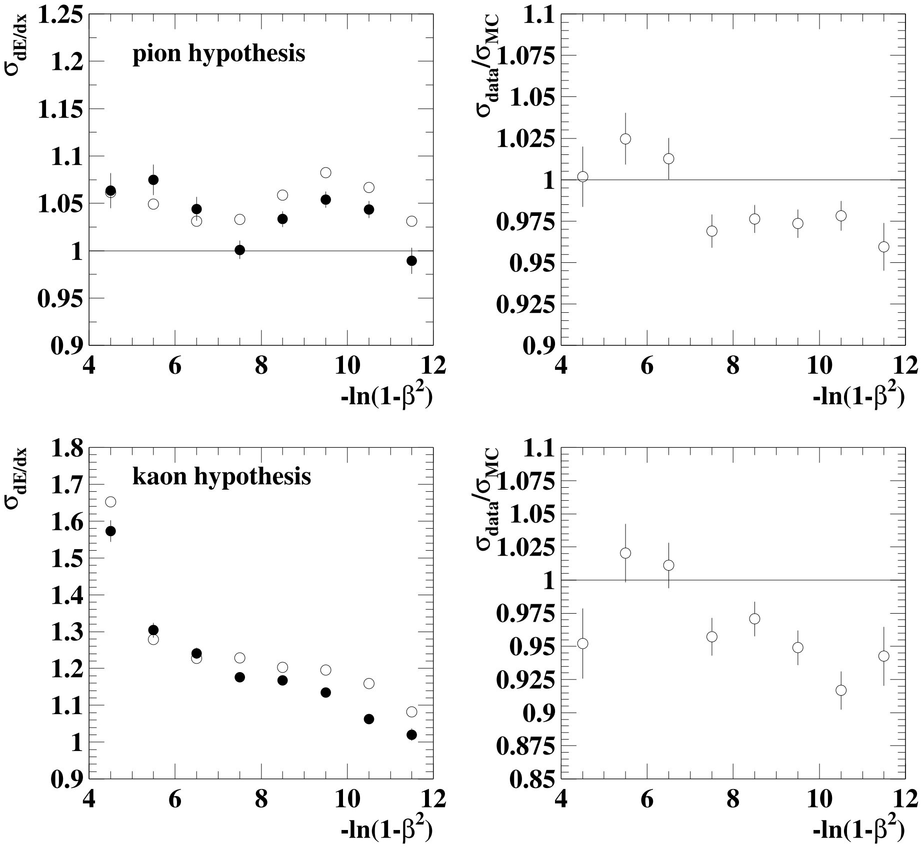

Figure B.6: The resolutions of the $N(\mathrm{d}E/\mathrm{d}x)$ distributions versus $-\ln(1-\beta_\pi^2)$ are plotted in the left-hand plots. The filled dots show the data and the open points show the Monte Carlo. The right-hand plots show the ratio of the data and Monte Carlo resolutions.

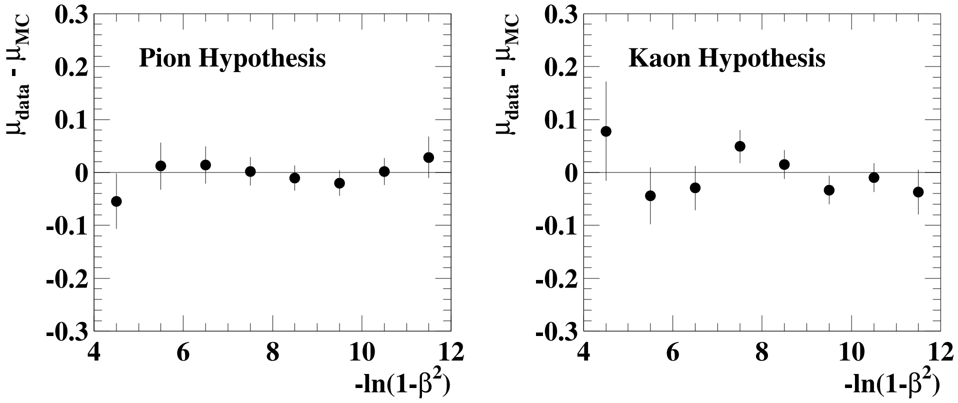

Figure B.7: The difference of the means of the data and Monte Carlo $N(\mathrm{d}E/\mathrm{d}x)$ distributions versus $-\ln(1-\beta_\pi^2)$ after the Monte Carlo has been corrected.

Monte Carlo. Both plots show that if $-\ln(1-\beta_\pi^2) > 7$ ($p > 5$ GeV) then the resolution of the Monte Carlo is larger than that of the data. The resolution of the pion and kaon $N(\mathrm{d}E/\mathrm{d}x)$ distributions are consequently scaled by 2.5% and 5%, respectively.

The results after the corrections have been applied to the Monte Carlo are shown in Figure B.7. The plots show the difference in the means of the $N(\mathrm{d}E/\mathrm{d}x)$ distributions after the corrections have been applied to the Monte Carlo as a function of $-\ln(1-\beta_\pi^2)$. The plots show that the means of the Monte Carlo $N(\mathrm{d}E/\mathrm{d}x)$ distributions are now consistent with the data. The χ^2 difference between the Monte Carlo and data for the pion hypothesis is $\chi^2/dof = 3.7/7$ and for the kaon hypothesis is $\chi^2/dof = 6.3/7$.

The resolutions of the $N(\mathrm{d}E/\mathrm{d}x)$ distributions are plotted versus $-\ln(1-\beta_\pi^2)$ in Figure B.8 after the Monte Carlo has been corrected. The data are the filled dots and the Monte Carlo are the open dots in the left hand plots. The right hand plots show the ratio of the resolution of the data with respect to the Monte Carlo. The plots show that the resolutions of the Monte Carlo are now consistent with the data.

Finally, to show that the corrected Monte Carlo models the data, several variables are plotted in Figure B.9. The number of hits, the normalised dE/dx distributions

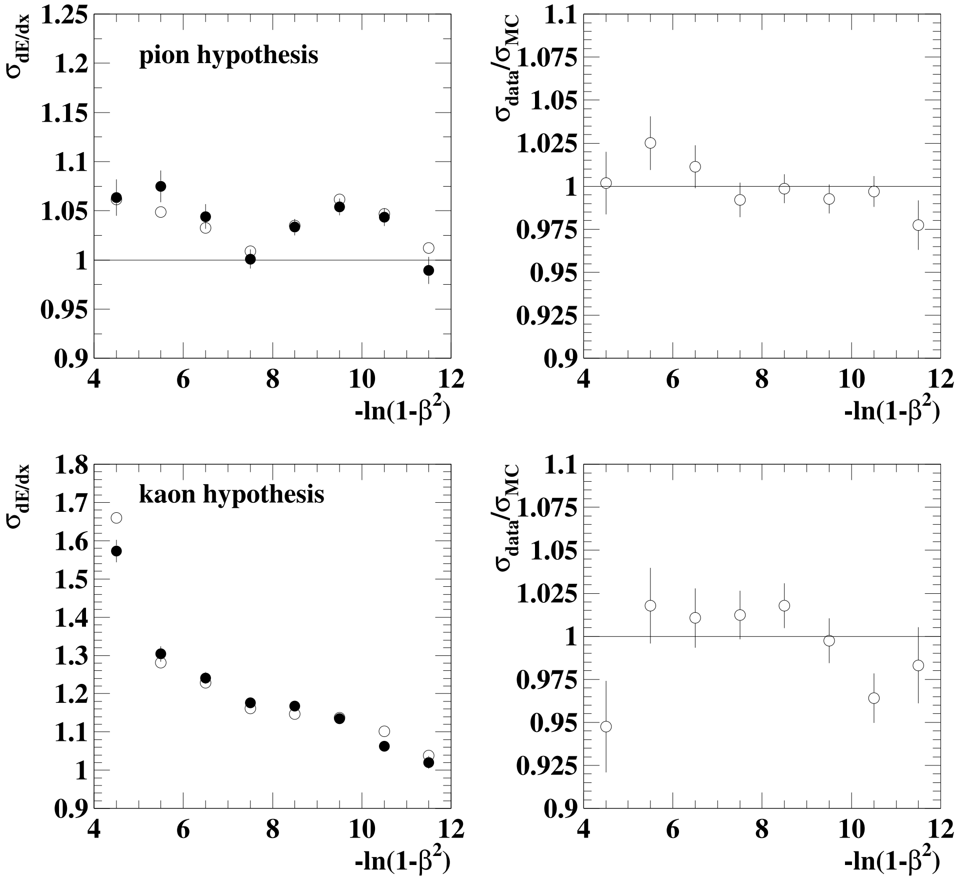

Figure B.8: The resolution of the $N(\mathrm{d}E/\mathrm{d}x)$ distributions versus $-\ln(1-\beta_\pi^2)$ after the corrections have been applied to the Monte Carlo are plotted in the left-hand plots. The filled dots show the data and the open dots show the Monte Carlo. The right-hand plots show the ratio of the data and corrected Monte Carlo resolutions.

for the pion and kaon hypotheses and the particle separation probability variables are plotted for the one-prong sample. Fits are are also shown on the $N(\mathrm{d}E/\mathrm{d}x)$ distributions. The hatched part of the plots shows the charged kaon contribution of the one-prong hadron sample. Good agreement is observed between the data and Monte Carlo for the six variables.

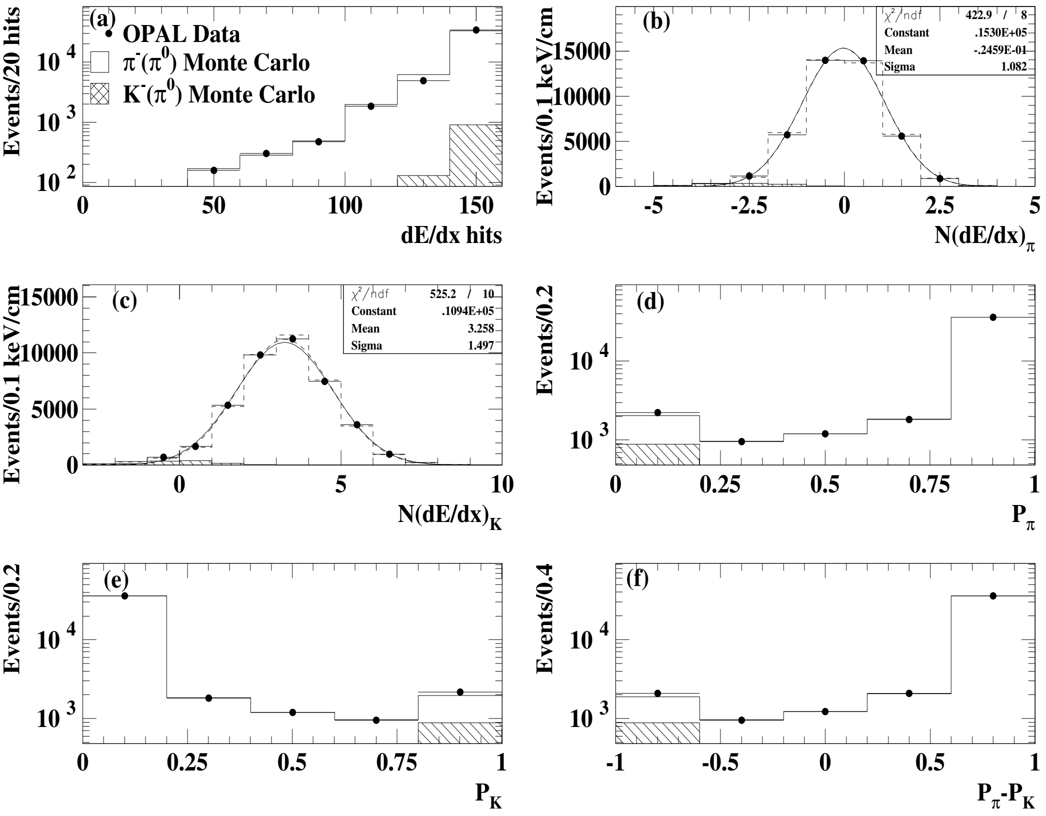

Figure B.9: Important dE/dx variables for the one-prong sample. (a) shows the number of dE/dx hits; (b) and (c) show the normalised dE/dx distributions for the pion and kaon hypotheses, respectively; and (d) – (f) show the particle separation probability variables for the one-prong sample.

Appendix C

The π^0 Finding Algorithm

The first section of this appendix describes the selection of the variables that are used in the neural network algorithm. The second section discusses the systematic studies that are performed to check the consistency of the neural network output.

C.1 Variable Selection

The first step in this analysis is to select variables that appear to have some separation power for decays containing π^0 mesons. These variables are then subjected to a statistical test to ensure that they do have separation power and to ensure that they are minimally correlated. Although there is no restriction on the number of variables, it is obvious that a small number will lead to more manageable and less time consuming algorithms. Various methods exist to quantify the usefulness of a variable with respect to its discriminating power and its correlation with other variables. This analysis used the F-test statistic as described in reference [64] which will now be outlined below.

Consider a set $\mathcal{E}$ of n events e_i divided into k classes, and described by l variables. Then all of the events are contained in a matrix x_{ij} with $i = 1, \dots, n$ and $j = 1, \dots, l$. For an arbitrary variable j, one can define g_j, the barycentre (gravity) of the entire event sample and h_j the barycentre of the events belonging to an arbitrary class C_m with n_m events:

$$g_j = \frac{1}{n}\sum_{i=1}^{n} x_{ij}, \qquad j = 1, \ldots, l \tag{C.1}$$

$$h_j = \frac{1}{n_m}\sum_{i \in C_m} x_{ij}, \qquad m = 1, \ldots, k \tag{C.2}$$

The *within* vector W describing the dispersion within a class can now be calculated using the above quantities

$$W_j = \sum_{m=1}^{k}\sum_{i \in C_m} \frac{1}{n}\left(x_{ij} - h_j\right)^2 . \tag{C.3}$$

Similarly, the *between* vector B describes the distance of a class to the overall barycentre g_j:

$$B_j = \frac{1}{n}\sum_{m=1}^{k} n_m \left(h_j - g_j\right)^2 . \tag{C.4}$$

Large values of B_j and small values of W_j characterise well separated and compact classes. Therefore the discriminating power of variable j is summarised in the F-test [64]:

$$F_j = \frac{(n-k)}{(k-1)}\frac{B_j}{W_j}. \tag{C.5}$$

The variables having high F-test values are considered to be those with the most discriminating power. For this analysis, the denominator gives 6 degrees of freedom while the numerator gives ∞ degrees of freedom, consequently any variable with an F-test value greater than 6.88 [52] would have adequate discriminating power.

For this analysis, the event sample is divided into two classes: class 1 ($\tau^- \to \pi^- \overline{\mathrm{K}}^0 \geq 1\pi^0 \nu_\tau$ decays) and class 2 ($\tau^- \to \pi^- \overline{\mathrm{K}}^0 \nu_\tau$ decays). The seven variables

	Variables						
	E/E_{Beam}	E/p	N	F_{90}	ϕ_{PS}	$\Delta\theta$	$\Delta\phi$
Class 1 Gravity	0.357	0.838	0.207	0.492	0.112	0.162	0.210
Class 2 Gravity	0.192	0.659	0.156	0.552	0.075	0.122	0.166
Total Gravity	0.237	0.171	0.170	0.536	0.085	0.133	0.178
Within Vector	0.015	0.033	0.007	0.013	0.007	0.015	0.036
Between Vector	0.0054	0.0031	0.0005	0.0007	0.0003	0.0003	0.0004
F-test	790.0	199.0	168.0	118.0	82.8	46.5	23.4

Table C.1: F-test results of the neural network variables.

described in Section 6.2.2 are subjected to the F-test and the results are shown in Table C.1. Note that the variables are normalised to be between zero and one, and are ordered according to the size of their F-test values. The results of the F-test show that the seven variables selected for the π^0 separation are statistically significant.

The correlations between the selected variables was checked to ensure that the seven variables were minimally correlated. Each element of the correlation matrix was calculated using [52]

$$\rho_{ij} = \frac{\text{cov}_{ij}}{\sqrt{\sigma_i \sigma_j}}, \tag{C.6}$$

where

$$\text{cov}_{ij} = \sum_{k=1}^{N} \frac{(x_{ij} - \mu_i)(y_{kj} - \mu_k)}{N-1} \tag{C.7}$$

is the covariance of the pair of variables ij in question with x_{ij} representing the value of one of the variables with mean μ_i and y_{kj} representing the second variable with mean μ_k. In addition, $\sigma_{i,j}$ is the variance of the variables i and j. The correlation matrix is shown in Table C.2. The largest correlation is between E/E_{Beam} and E/p at 0.544, which is below the recommended cutoff of 0.55 suggested in reference [64].

The seven variables that appear to have some π^0 separation ability are now input into the JETNET [51] neural net algorithm. The neural net was trained using the two classes of data as predicted by the Monte Carlo. The training was done using

	E/E_{Beam}	E/p	N	F_{90}	ϕ_{PS}	$\Delta\theta$	$\Delta\phi$
E/E_{Beam}	1.000	0.544	0.241	-0.393	0.176	0.032	0.078
E/p	0.544	1.000	0.134	-0.265	0.303	0.398	0.532
N	0.241	0.134	1.000	-0.294	0.270	0.138	0.162
F_{90}	-0.393	-0.265	-0.294	1.000	-0.061	-0.071	-0.103
ϕ_{PS}	0.176	0.303	0.270	-0.061	1.000	0.178	0.455
$\Delta\theta$	0.032	0.398	0.138	-0.071	0.178	1.000	0.372
$\Delta\phi$	0.078	0.532	0.162	-0.103	0.455	0.372	1.000

Table C.2: The correlation matrix for the π^0 variables.

three layers, including 7 input nodes, 12 internal neurons and 1 output node. The neural network was trained until the figure of merit (FOM) of the training sample was constant. The FOM measures the separation achieved between the two classes — values close to zero indicate no separation, whilst one indicates complete separation. A total of 40 epochs were used to train the neural net. The FOM versus the epoch number is shown for the training and test sample in Figure C.1. Additionally, the purity of the class 1 ($\tau^- \to \pi^-\overline{\mathrm{K}}^0 \geq 1\pi^0\nu_\tau$) decays is plotted versus the neural network output — for a properly trained network this should be linear, with the network output representing the signal purity; good agreement is observed between the training and test samples.

C.2 Systematic Studies

Several systematic studies were done to verify that the neural network algorithm adequately identifies decays containing π^0 mesons. The first test involved changing the energy scale of the Monte Carlo of the electromagnetic calorimeter by ±1%. This affects two variables: E/E_{beam} and E/p. The systematic errors were estimated by calculating the branching ratios for the scaled energy and taking the difference between these values and the nominal branching ratios. The systematic errors were 0.00007 and 0.00013 for the $\tau^- \to \pi^-\overline{\mathrm{K}}^0\nu_\tau$ and $\tau^- \to \pi^-\overline{\mathrm{K}}^0 \geq 1\pi^0\nu_\tau$ decays, respectively.

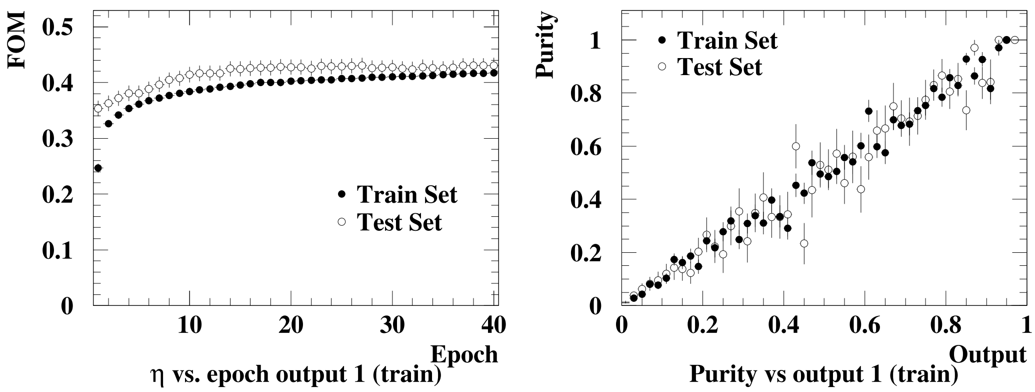

Figure C.1: The FOM versus the epoch number is shown on the left plot while the purity versus the neural network output of the $\tau^- \to \pi^- \overline{\mathrm{K}}^0 \geq 1\pi^0\nu_\tau$ decays is shown in the right plot.

	$\pi\mathrm{K}^0$	$\pi\mathrm{K}^0 \geq 1\pi^0$
Nominal	0.00912	0.00357
Drop N_{clus}	$+0.00011$	-0.00020
Drop F_{90}	$+0.00002$	-0.00003
Drop ϕ_{PS}	-0.00006	$+0.00013$
Drop $\Delta\theta$	-0.00012	$+0.00024$
Drop $\Delta\phi$	-0.00004	$+0.00007$

Table C.3: The change in the branching ratios when each non-energy dependent variable is dropped from the neural network.

For the next test, each non-energy dependent variable was dropped from the neural network and the differences calculated between these results and the nominal branching ratios. The results of these tests are shown in Table C.3. The largest change from the nominal branching ratios are taken as the systematic uncertainties.

The following checks are not included as part of the systematic uncertainties, but were done to ensure that the neural network output was stable within systematic uncertainties. The first check involved dropping each variable from the neural network until only the two most significant variables remained. The results of this check, along

	πK^0	$\pi K^0 \geq 1\pi^0$
Nominal	0.00912(0.00094)	0.00357(0.00131)
Drop $\Delta\phi$	0.00900(0.00094)	0.00365(0.00133)
$+\Delta\theta$	0.00908(0.00098)	0.00351(0.00141)
$+\phi_{\mathrm{PS}}$	0.00881(0.00103)	0.00408(0.00157)
$+F_{90}$	0.00869(0.00103)	0.00397(0.00161)
$+N_{clus}$	0.00889(0.00108)	0.00396(0.00169)

Table C.4: The branching ratios and statistical uncertainties when each of the variables are removed from the neural network until only two variables remain.

with the statistical errors on the branching ratios are shown in Table C.4. The table shows the expected results, such that as the variables are removed from the neural network the statistical uncertainty increases.

The correlation matrix coefficients of the $\tau^- \to X^- K^0_L \nu_\tau$ selected decays were calculated for the data and Monte Carlo. The Monte Carlo was divided into ten equal samples and the correlation matrix was calculated each time; these results were then averaged. In Table C.5 the correlation between each variable is shown for the data and Monte Carlo. The minimum and maximum correlation coefficients of the ten Monte Carlo samples is also shown. The uncertainty shown on the Monte Carlo coefficients is the standard deviation of the ten samples. The χ^2 is calculated for each pair of coefficients and the total χ^2/dof is 21.1/20, indicating that the seven variables chosen for the π^0 identification are well modelled by the Monte Carlo.

A final test of the neural networks ability to identify π^0 mesons was done by calculating the one-prong branching ratios: $\tau^- \to h^- \nu_\tau$ and $\tau^- \to h^- \geq 1\pi^0\nu_\tau$. This was done using the one-prong sample selected for the K^0_L analysis. In order to remove leptons, it was required that the hadronic energy be greater than 2.5 GeV. Using this requirement the following results were obtained: $B(\tau^- \to h^- \nu_\tau) = 0.1157 \pm 0.0022$

Variables	Data	MC(mean/sigma)	MC(min/max)		$(D-M)^2/\sigma^2$
E/E_b - E/p	0.70	0.65(0.05)	0.58	0.72	1.00
E/E_b - N_{cl}	0.25	0.23(0.04)	0.15	0.30	0.25
E/E_b - F_{90}	-0.35	$-0.39(0.06)$	-0.49	-0.33	0.44
E/E_b - ϕ_{PS}	0.36	0.28(0.04)	0.20	0.36	4.00
E/E_b - $\Delta\theta$	0.10	0.18(0.06)	0.10	0.32	1.78
E/E_b - $\Delta\phi$	0.26	0.21(0.04)	0.14	0.27	1.56
E/p - N_{cl}	0.23	0.18(0.03)	0.13	0.24	2.78
E/p - F_{90}	-0.21	$-0.22(0.06)$	-0.32	-0.14	0.03
E/p - ϕ_{PS}	0.43	0.38(0.03)	0.32	0.44	2.78
E/p - $\Delta\theta$	0.29	0.33(0.04)	0.25	0.42	1.00
E/p - $\Delta\phi$	0.61	0.55(0.04)	0.51	0.63	2.25
N_{cl} - F_{90}	-0.32	$-0.24(0.05)$	-0.34	-0.17	2.56
N_{cl} - ϕ_{PS}	0.38	0.36(0.08)	0.28	0.51	0.06
N_{cl} - $\Delta\theta$	0.26	0.22(0.04)	0.17	0.32	1.00
N_{cl} - $\Delta\phi$	0.31	0.28(0.06)	0.13	0.34	0.25
F_{90} - ϕ_{PS}	-0.04	$-0.07(0.07)$	-0.20	0.03	0.18
F_{90} - $\Delta\theta$	-0.10	$-0.10(0.04)$	-0.14	-0.02	0.00
F_{90} - $\Delta\phi$	-0.10	$-0.11(0.06)$	-0.22	-0.02	0.03
ϕ_{PS} - $\Delta\theta$	0.23	0.27(0.06)	0.14	0.35	0.44
ϕ_{PS} - $\Delta\phi$	0.51	0.54(0.05)	0.47	0.62	0.64
$\Delta\theta$ - $\Delta\phi$	0.39	0.35(0.05)	0.28	0.43	0.64
			Total (χ^2/dof):		21.1/20

Table C.5: The correlation coefficients for the 21 pairs of variables of the data (second column) and Monte Carlo (third column) for $\tau^- \to X^- \mathrm{K}^0_\mathrm{L} \nu_\tau$ decays. The fourth column shows the minimum and maximum correlations for the 10 Monte Carlo samples and the fifth column shows the χ^2 difference between the Monte Carlo and the data. The total χ^2/dof is shown in the last line of the table.

and $B(\tau^- \to h^- \geq 1\pi^0\nu_\tau) = 0.3882 \pm 0.0044$. The current world averages for these decay modes are [3, p. 286]: $B(\tau^- \to h^-\nu_\tau) = 0.1179 \pm 0.0012$ and $B(\tau^- \to h^- \geq 1\pi^0\nu_\tau) = 0.3691 \pm 0.0017$. The difference between the two decay modes were 2% and 5%, respectively. These errors are within the systematic errors quoted above for the K^0_L decays (2% and 7%), thus confirming the ability of the neural network to identify decays containing π^0 mesons.

Appendix D

The Bias Factor

The τ pair selection, discussed in Section 5.2, does not select all τ decay modes with an equal probability. This leads to a *bias* on the τ pair selection which selects certain decay modes over others. This is quantified as a set of *bias factors* for each decay mode in the Monte Carlo. The bias factors are calculated from the set of Monte Carlo samples used in this analysis, shown in Table D.1. The Monte Carlo samples used three different detector configurations, slightly different branching ratios and run 1520 used a different electromagnetic shower algorithm than the other Monte Carlo samples. These differences will be shown to have a negligible effect on the decay modes between the four different Monte Carlo samples.

Run Number	Detector Configuration	τ pair events generated at $E_{\mathrm{CM}} = 91.2$ GeV
1520	1994	600000
1536	1995	375000
1560	1994	800000
1565	1992	500000

Table D.1: The Monte Carlo samples used in the bias factor calculation.

The bias factor of decay mode i (F_i^{bias}) is defined as

$$F_i^{\mathrm{bias}} \equiv \frac{B_i^{\mathrm{after}}}{B_i^{\mathrm{before}}}, \tag{D.1}$$

where B_i^{before} (B_i^{after}) is the branching ratio of decay i before (after) the τ pair selection. The branching ratios are defined by equation 7.1, thus equation D.1 is written as

$$F_i^{\text{bias}} = \frac{N_i^{\text{after}}/N_\tau^{\text{after}}}{N_i^{\text{before}}/N_\tau^{\text{before}}} \tag{D.2}$$

where N_i^{after} (N_i^{before}) is the number of decays i after (before) the τ pair selection and N_τ^{after} (N_τ^{before}) is the total number of taus after (before) the τ pair selection. The uncertainty on the bias factor is calculated as the binomial error on the numerator and denominator of equation D.2. However, this estimate slightly overestimates the true error, as correlations between the branching ratios in the numerator and denominator are ignored. The bias factors from each Monte Carlo simulation are shown in Table D.2. In general, the bias factors from the four different Monte Carlo samples are consistent with each other within their statistical uncertainties. The bias factors for the decay modes measured in this work are shown in Table D.3.

The Monte Carlo used in this analysis was created with a centre-of-mass energy of 91.2 GeV, the Z^0 mass. However, some of the data collected by the OPAL detector between 1991 and 1995 was at energies slightly below and above the Z^0 mass. Consequently, to estimate any possible systematic variations on the bias factor due to the different energies, the requirements dependent on the centre-of-mass energy in Monte Carlo run 1560 were varied. This was done by rescaling the centre-of-mass energy by up to $\pm 1.0\%$ and recalculating the bias factor for each decay mode. The results are shown in Table D.4. Similar results were observed for the other Monte Carlo samples. As the centre-of-mass energy is scaled, the central values of the Monte Carlo 1560 bias factors change less than the statistical error. As a result, the statistical errors on the bias factors are considered sufficient to describe the total bias factor errors.

Decay Mode	MC1520	MC1536	MC1560	MC1565
$\tau^- \to \mathrm{e}^-\overline{\nu}_\mathrm{e}\nu_\tau$	1.004 ± 0.003	1.004 ± 0.004	1.007 ± 0.003	1.003 ± 0.004
$\tau^- \to \mu^-\overline{\nu}_\mu\nu_\tau$	0.983 ± 0.004	0.987 ± 0.004	0.985 ± 0.003	0.984 ± 0.004
$\tau^- \to \pi^-\nu_\tau$	0.987 ± 0.004	0.991 ± 0.005	0.992 ± 0.004	0.994 ± 0.005
$\tau^- \to \pi^-\pi^0\nu_\tau$	1.021 ± 0.003	1.019 ± 0.003	1.018 ± 0.002	1.018 ± 0.003
$\tau^- \to \pi^-\pi^+\pi^-\nu_\tau$	0.993 ± 0.005	0.990 ± 0.006	0.988 ± 0.004	0.987 ± 0.005
$\tau^- \to \pi^-2\pi^0\nu_\tau$	1.016 ± 0.005	1.013 ± 0.006	1.011 ± 0.004	1.016 ± 0.005
$\tau^- \to \mathrm{K}^-\nu_\tau$	1.008 ± 0.019	1.017 ± 0.023	0.996 ± 0.016	0.990 ± 0.020
$\tau^- \to \pi^-\pi^+\pi^-\pi^0\nu_\tau$	0.959 ± 0.007	0.958 ± 0.009	0.964 ± 0.006	0.971 ± 0.008
$\tau^- \to \pi^-3\pi^0\nu_\tau$	1.008 ± 0.012	0.998 ± 0.016	1.003 ± 0.011	1.006 ± 0.014
$\tau^- \to 3\pi^-2\pi^+\nu_\tau$	0.782 ± 0.063	0.793 ± 0.079	0.779 ± 0.054	0.753 ± 0.067
$\tau^- \to 3\pi^-2\pi^+\pi^0\nu_\tau$	0.827 ± 0.114	0.625 ± 0.149	0.799 ± 0.103	0.758 ± 0.132
$\tau^- \to \pi^-\pi^+\pi^-2\pi^0\nu_\tau$	0.944 ± 0.026	0.967 ± 0.030	0.934 ± 0.021	0.947 ± 0.027
$\tau^- \to \pi^-\pi^+\pi^-3\pi^0\nu_\tau$	0.832 ± 0.075	0.928 ± 0.060	0.934 ± 0.041	0.912 ± 0.051
$\tau^- \to \mathrm{K}^-2\pi^0\nu_\tau$	1.011 ± 0.072	1.042 ± 0.067	1.035 ± 0.047	1.014 ± 0.060
$\tau^- \to \mathrm{K}^-\mathrm{K}^0_\mathrm{L}\pi^0\nu_\tau$	1.010 ± 0.054	1.027 ± 0.075	0.957 ± 0.053	1.020 ± 0.067
$\tau^- \to \mathrm{K}^-\mathrm{K}^0_\mathrm{S}(2\pi^0)\pi^0\nu_\tau$	0.992 ± 0.103	1.109 ± 0.147	0.955 ± 0.102	1.128 ± 0.123
$\tau^- \to \mathrm{K}^-\mathrm{K}^0_\mathrm{S}(\mathrm{other})\pi^0\nu_\tau$	1.002 ± 0.066	0.952 ± 0.094	0.975 ± 0.065	0.937 ± 0.077
$\tau^- \to \pi^-\pi^0\eta(2\gamma)\nu_\tau$	1.090 ± 0.062	1.044 ± 0.076	0.991 ± 0.052	1.047 ± 0.068
$\tau^- \to \pi^-\pi^0\eta(3\pi^0)\nu_\tau$	1.037 ± 0.067	1.013 ± 0.084	0.960 ± 0.058	1.035 ± 0.072
$\tau^- \to \pi^-\mathrm{K}^0_\mathrm{L}\mathrm{K}^0_\mathrm{L}\nu_\tau$	1.114 ± 0.089	0.959 ± 0.130	0.960 ± 0.091	0.976 ± 0.111
$\tau^- \to \pi^-\mathrm{K}^-\mathrm{K}^+\nu_\tau$	1.011 ± 0.039	1.025 ± 0.052	0.999 ± 0.036	0.975 ± 0.046
$\tau^- \to \pi^-\pi^0\mathrm{K}^0_\mathrm{L}\nu_\tau$	1.014 ± 0.051	0.978 ± 0.044	1.032 ± 0.030	0.963 ± 0.040
$\tau^- \to \pi^-\pi^0\gamma\nu_\tau$	1.033 ± 0.063	1.035 ± 0.081	1.012 ± 0.056	1.020 ± 0.071
$\tau^- \to \pi^-\pi^0\mathrm{K}^0_\mathrm{S}(2\pi^0)\nu_\tau$	1.168 ± 0.092	1.019 ± 0.079	1.025 ± 0.057	0.994 ± 0.073
$\tau^- \to \pi^-\pi^0\mathrm{K}^0_\mathrm{S}(\mathrm{other})\nu_\tau$	0.994 ± 0.061	0.978 ± 0.053	0.987 ± 0.036	0.990 ± 0.045
$\tau^- \to \pi^-\pi^0\eta(\mathrm{other})\nu_\tau$	0.957 ± 0.072	0.977 ± 0.087	0.962 ± 0.060	1.004 ± 0.077
$\tau^- \to (\pi\pi\mathrm{K})^-\nu_\tau$	0.965 ± 0.037	0.975 ± 0.032	0.981 ± 0.022	0.984 ± 0.027
$\tau^- \to \mathrm{K}^-\mathrm{K}^0_\mathrm{L}\nu_\tau$	1.014 ± 0.040	0.993 ± 0.069	1.010 ± 0.048	1.032 ± 0.060
$\tau^- \to \mathrm{K}^-\mathrm{K}^0_\mathrm{S}(2\pi^0)\nu_\tau$	1.067 ± 0.076	1.073 ± 0.131	1.091 ± 0.088	1.032 ± 0.118
$\tau^- \to \mathrm{K}^-\mathrm{K}^0_\mathrm{S}(\mathrm{other})\nu_\tau$	0.996 ± 0.049	0.968 ± 0.082	1.011 ± 0.055	1.027 ± 0.070
$\tau^- \to \mathrm{K}^* \to \mathrm{K}^-\pi^0\nu_\tau$	0.988 ± 0.023	1.011 ± 0.029	1.024 ± 0.020	1.010 ± 0.026
$\tau^- \to \mathrm{K}^* \to \pi^-\mathrm{K}^0_\mathrm{L}\nu_\tau$	0.997 ± 0.024	0.989 ± 0.030	0.973 ± 0.021	0.996 ± 0.026
$\tau^- \to \mathrm{K}^* \to \pi^-\mathrm{K}^0_\mathrm{S}(2\pi^0)\nu_\tau$	1.059 ± 0.044	1.050 ± 0.055	1.031 ± 0.039	1.085 ± 0.048
$\tau^- \to \mathrm{K}^* \to \pi^-\mathrm{K}^0_\mathrm{S}(\mathrm{other})\nu_\tau$	1.003 ± 0.027	0.951 ± 0.035	0.992 ± 0.024	0.977 ± 0.031
$\tau^- \to \pi^-\mathrm{K}^0_\mathrm{L}\mathrm{K}^0_\mathrm{S}(2\pi^0)\nu_\tau$	1.043 ± 0.122	1.043 ± 0.162	1.053 ± 0.109	0.982 ± 0.136
$\tau^- \to \pi^-\mathrm{K}^0_\mathrm{L}\mathrm{K}^0_\mathrm{S}(\mathrm{other})\nu_\tau$	0.942 ± 0.077	1.005 ± 0.101	0.954 ± 0.070	0.948 ± 0.090
$\tau^- \to \pi^-\mathrm{K}^0_\mathrm{S}(2\pi^0)\mathrm{K}^0_\mathrm{S}(2\pi^0)\nu_\tau$	0.920 ± 0.369	1.267 ± 0.392	1.021 ± 0.322	1.032 ± 0.417
$\tau^- \to \pi^-\mathrm{K}^0_\mathrm{S}(2\pi^0)\mathrm{K}^0_\mathrm{S}(\mathrm{other})\nu_\tau$	1.005 ± 0.136	1.037 ± 0.170	0.924 ± 0.135	1.085 ± 0.166
$\tau^- \to \pi^-\mathrm{K}^0_\mathrm{S}(\mathrm{other})\mathrm{K}^0_\mathrm{S}(\mathrm{other})\nu_\tau$	0.906 ± 0.125	0.964 ± 0.184	0.914 ± 0.120	0.750 ± 0.177

Table D.2: The bias factors for all decay modes in each Monte Carlo sample. The errors shown are statistical.

Signal Channel	Bias Factor
$\tau^- \to X^-\mathrm{K}^0_\mathrm{L}\nu_\tau$	0.991 ± 0.007
$\tau^- \to \pi^-\overline{\mathrm{K}}^0\nu_\tau$	0.986 ± 0.009
$\tau^- \to \pi^-\overline{\mathrm{K}}^0 \geq 1\pi^0\nu_\tau$	0.995 ± 0.015
$\tau^- \to \mathrm{K}^-\mathrm{K}^0 \geq 0\pi^0\nu_\tau$	0.999 ± 0.015

Table D.3: The bias factors for the decay modes measured in this analysis.

Decay Mode	-1.0%	-0.5%	Nominal	$+0.5\%$	$+1.0\%$
$\tau^- \to \mathrm{e}^-\overline{\nu}_\mathrm{e}\nu_\tau$	1.007 ± 0.003	1.007 ± 0.003	1.007 ± 0.003	1.007 ± 0.003	1.006 ± 0.003
$\tau^- \to \mu^-\overline{\nu}_\mu\nu_\tau$	0.984 ± 0.003	0.985 ± 0.003	0.985 ± 0.003	0.986 ± 0.003	0.986 ± 0.003
$\tau^- \to \pi^-\nu_\tau$	0.992 ± 0.004	0.992 ± 0.004	0.992 ± 0.004	0.992 ± 0.004	0.992 ± 0.004
$\tau^- \to \pi^-\pi^0\nu_\tau$	1.019 ± 0.002	1.018 ± 0.002	1.018 ± 0.002	1.018 ± 0.002	1.018 ± 0.002
$\tau^- \to \pi^-\pi^+\pi^-\nu_\tau$	0.988 ± 0.004	0.988 ± 0.004	0.988 ± 0.004	0.988 ± 0.004	0.987 ± 0.004
$\tau^- \to \pi^-2\pi^0\nu_\tau$	1.011 ± 0.004	1.011 ± 0.004	1.011 ± 0.004	1.011 ± 0.004	1.011 ± 0.004
$\tau^- \to \mathrm{K}^-\nu_\tau$	0.996 ± 0.016	0.996 ± 0.016	0.996 ± 0.016	0.996 ± 0.016	0.996 ± 0.016
$\tau^- \to \pi^-\pi^+\pi^-\pi^0\nu_\tau$	0.965 ± 0.006	0.965 ± 0.006	0.964 ± 0.006	0.964 ± 0.006	0.964 ± 0.006
$\tau^- \to \pi^-3\pi^0\nu_\tau$	1.003 ± 0.011	1.004 ± 0.011	1.003 ± 0.011	1.004 ± 0.011	1.003 ± 0.011
$\tau^- \to 3\pi^-2\pi^+\nu_\tau$	0.780 ± 0.054	0.780 ± 0.054	0.779 ± 0.054	0.779 ± 0.054	0.779 ± 0.054
$\tau^- \to 3\pi^-2\pi^+\pi^0\nu_\tau$	0.800 ± 0.103	0.800 ± 0.103	0.799 ± 0.103	0.799 ± 0.103	0.799 ± 0.103
$\tau^- \to \pi^-\pi^+\pi^-2\pi^0\nu_\tau$	0.935 ± 0.021	0.935 ± 0.021	0.934 ± 0.021	0.934 ± 0.021	0.934 ± 0.021
$\tau^- \to \pi^-\pi^+\pi^-3\pi^0\nu_\tau$	0.933 ± 0.041	0.932 ± 0.041	0.934 ± 0.041	0.934 ± 0.041	0.934 ± 0.041
$\tau^- \to \mathrm{K}^-2\pi^0\nu_\tau$	1.035 ± 0.047	1.035 ± 0.047	1.035 ± 0.047	1.034 ± 0.047	1.032 ± 0.047
$\tau^- \to \mathrm{K}^-\mathrm{K}^0_\mathrm{L}\pi^0\nu_\tau$	0.956 ± 0.053	0.955 ± 0.053	0.957 ± 0.053	0.957 ± 0.053	0.956 ± 0.053
$\tau^- \to \mathrm{K}^-\mathrm{K}^0_\mathrm{S}(2\pi^0)\pi^0\nu_\tau$	0.949 ± 0.102	0.948 ± 0.102	0.955 ± 0.102	0.954 ± 0.102	0.954 ± 0.102
$\tau^- \to \mathrm{K}^-\mathrm{K}^0_\mathrm{S}(\mathrm{other})\pi^0\nu_\tau$	0.975 ± 0.065	0.975 ± 0.065	0.975 ± 0.065	0.975 ± 0.065	0.974 ± 0.065
$\tau^- \to \pi^-\pi^0\eta(2\gamma)\nu_\tau$	0.992 ± 0.052	0.992 ± 0.052	0.991 ± 0.052	0.991 ± 0.052	0.991 ± 0.052
$\tau^- \to \pi^-\pi^0\eta(3\pi^0)\nu_\tau$	0.959 ± 0.058	0.958 ± 0.058	0.960 ± 0.058	0.960 ± 0.058	0.960 ± 0.058
$\tau^- \to \pi^-\mathrm{K}^0_\mathrm{L}\mathrm{K}^0_\mathrm{L}\nu_\tau$	0.966 ± 0.091	0.966 ± 0.091	0.960 ± 0.091	0.960 ± 0.091	0.960 ± 0.091
$\tau^- \to \pi^-\mathrm{K}^-\mathrm{K}^+\nu_\tau$	1.000 ± 0.036	1.000 ± 0.036	0.999 ± 0.036	0.999 ± 0.036	0.998 ± 0.036
$\tau^- \to \pi^-\pi^0\mathrm{K}^0_\mathrm{L}\nu_\tau$	1.032 ± 0.030	1.032 ± 0.030	1.032 ± 0.030	1.031 ± 0.030	1.032 ± 0.030
$\tau^- \to \pi^-\pi^0\gamma\nu_\tau$	1.012 ± 0.056	1.012 ± 0.056	1.012 ± 0.056	1.011 ± 0.056	1.011 ± 0.056
$\tau^- \to \pi^-\pi^0\mathrm{K}^0_\mathrm{S}(2\pi^0)\nu_\tau$	1.026 ± 0.057	1.026 ± 0.057	1.025 ± 0.057	1.025 ± 0.057	1.025 ± 0.057
$\tau^- \to \pi^-\pi^0\mathrm{K}^0_\mathrm{S}(\mathrm{other})\nu_\tau$	0.987 ± 0.036	0.987 ± 0.036	0.987 ± 0.036	0.986 ± 0.036	0.986 ± 0.036
$\tau^- \to \pi^-\pi^0\eta(\mathrm{other})\nu_\tau$	0.962 ± 0.060	0.962 ± 0.060	0.962 ± 0.060	0.964 ± 0.060	0.963 ± 0.060
$\tau^- \to (\pi\pi\mathrm{K})^-\nu_\tau$	0.981 ± 0.022	0.981 ± 0.022	0.981 ± 0.022	0.981 ± 0.022	0.982 ± 0.022
$\tau^- \to \mathrm{K}^-\mathrm{K}^0_\mathrm{L}\nu_\tau$	1.011 ± 0.048	1.011 ± 0.048	1.010 ± 0.048	1.010 ± 0.048	1.010 ± 0.048
$\tau^- \to \mathrm{K}^-\mathrm{K}^0_\mathrm{S}(2\pi^0)\nu_\tau$	1.092 ± 0.088	1.091 ± 0.088	1.091 ± 0.088	1.091 ± 0.088	1.090 ± 0.088
$\tau^- \to \mathrm{K}^-\mathrm{K}^0_\mathrm{S}(\mathrm{other})\nu_\tau$	1.012 ± 0.055	1.011 ± 0.055	1.011 ± 0.055	1.011 ± 0.055	1.010 ± 0.055
$\tau^- \to \mathrm{K}^* \to \mathrm{K}^-\pi^0\nu_\tau$	1.023 ± 0.020	1.024 ± 0.020	1.024 ± 0.020	1.024 ± 0.020	1.024 ± 0.020
$\tau^- \to \mathrm{K}^* \to \pi^-\mathrm{K}^0_\mathrm{L}\nu_\tau$	0.973 ± 0.021	0.973 ± 0.021	0.973 ± 0.021	0.972 ± 0.021	0.972 ± 0.021
$\tau^- \to \mathrm{K}^* \to \pi^-\mathrm{K}^0_\mathrm{S}(2\pi^0)\nu_\tau$	1.032 ± 0.039	1.031 ± 0.039	1.031 ± 0.039	1.031 ± 0.039	1.030 ± 0.039
$\tau^- \to \mathrm{K}^* \to \pi^-\mathrm{K}^0_\mathrm{S}(\mathrm{other})\nu_\tau$	0.993 ± 0.024	0.992 ± 0.024	0.992 ± 0.024	0.992 ± 0.024	0.991 ± 0.024
$\tau^- \to \pi^-\mathrm{K}^0_\mathrm{L}\mathrm{K}^0_\mathrm{S}(2\pi^0)\nu_\tau$	1.054 ± 0.109	1.054 ± 0.109	1.053 ± 0.109	1.053 ± 0.109	1.053 ± 0.109
$\tau^- \to \pi^-\mathrm{K}^0_\mathrm{L}\mathrm{K}^0_\mathrm{S}(\mathrm{other})\nu_\tau$	0.954 ± 0.070	0.954 ± 0.070	0.954 ± 0.070	0.954 ± 0.070	0.953 ± 0.070
$\tau^- \to \pi^-\mathrm{K}^0_\mathrm{S}(2\pi^0)\mathrm{K}^0_\mathrm{S}(2\pi^0)\nu_\tau$	1.022 ± 0.322	1.021 ± 0.322	1.021 ± 0.322	1.021 ± 0.322	1.020 ± 0.322
$\tau^- \to \pi^-\mathrm{K}^0_\mathrm{S}(2\pi^0)\mathrm{K}^0_\mathrm{S}(\mathrm{other})\nu_\tau$	0.925 ± 0.135	0.925 ± 0.135	0.924 ± 0.135	0.924 ± 0.135	0.924 ± 0.135
$\tau^- \to \pi^-\mathrm{K}^0_\mathrm{S}(\mathrm{other})\mathrm{K}^0_\mathrm{S}(\mathrm{other})\nu_\tau$	0.915 ± 0.120	0.915 ± 0.120	0.914 ± 0.120	0.914 ± 0.120	0.914 ± 0.120

Table D.4: The bias factors for Monte Carlo 1560 with the centre-of-mass energy varied by up to ±1%. The errors shown are statistical.

Appendix E

Error on an inverse matrix

The inverse of the efficiency matrix is used to extract the branching ratios. Consequently, the uncertainty on each of the inverse matrix elements is needed to evaluate the systematic errors on the branching ratios. These uncertainties are evaluated from the known uncertainties of the efficiency matrix using the following method [65]. Often the errors of an inverted matrix are estimated by ignoring the off-diagonal elements of the covariance matrix. This is the correct procedure *only* if the quantities involved are independent of each other.

If one considers a nonsingular matrix $[\epsilon]$ with elements $\epsilon_{ij} \pm \sigma_{ij}$ then

$$[\epsilon][\epsilon]^{-1} = \mathbf{I} \tag{E.1}$$

where $[\epsilon]^{-1}$ is the inverse matrix with elements $\epsilon_{ij}^{-1} \pm \sigma_{\epsilon_{ij}^{-1}}$ and $\mathbf{I}$ is the unitary matrix. Taking the derivative of both sides of this equation yields

$$\delta[\epsilon][\epsilon]^{-1} + [\epsilon]\delta[\epsilon]^{-1} = [0] \tag{E.2}$$

or

$$\delta[\epsilon]^{-1} = -\left([\epsilon]^{-1}\delta[\epsilon][\epsilon]^{-1}\right). \tag{E.3}$$

Thus the uncertainty on each element of $[\epsilon]^{-1}$ $(\sigma_{\epsilon^{-1}_{ij}})$ is given by

$$[\sigma_{\epsilon^{-1}_{ij}}]^2 = \left|[\epsilon^{-1}_{ia}]\,\delta[\epsilon_{ab}]\,[\epsilon^{-1}_{bj}]\right|^2 , \tag{E.4}$$

where the ϵ_{ij} are all uncorrelated and the sum is over repeated indices unless otherwise noted. Substituting $\delta[\epsilon_{ab}] = [\sigma_{ab}]$ into equation E.4 gives

$$[\sigma_{\epsilon^{-1}_{ij}}]^2 = \left|[\epsilon^{-1}_{ia}]\,[\sigma_{ab}]\,[\epsilon^{-1}_{bj}]\right|^2 . \tag{E.5}$$

This equation is a reasonable approximation but is incorrect. It neglects any correlations between the elements of the inverse efficiency matrix, which can be significant. The following calculation shows how equation E.5 can be modified to include the off-diagonal elements of the inverse efficiency matrix.

It is always possible to write the inverse of a matrix in terms of its cofactors divided by the determinant, in which each element of an inverse matrix has elements of the original matrix in common. Thus the inverse matrix elements are correlated.

As above, consider a matrix $[\epsilon]$ with elements ϵ_{ij} and in the most general case covariances denoted by $\mathrm{cov}(\epsilon_{\alpha\beta}, \epsilon_{ab})$. The inverse matrix elements ϵ^{-1}_{ij}, in general, have covariances $\mathrm{cov}(\epsilon^{-1}_{\alpha\beta}, \epsilon^{-1}_{ab})$, which can be written as,

$$\mathrm{cov}(\epsilon^{-1}_{\alpha\beta}, \epsilon^{-1}_{ab}) = \epsilon^{-1}_{\alpha i}\epsilon^{-1}_{j\beta}\epsilon^{-1}_{ak}\epsilon^{-1}_{lb}\mathrm{cov}(\epsilon_{ij}, \epsilon_{kl}). \tag{E.6}$$

The full derivation is given in [65]. If there are no correlations between the elements of the efficiency matrix then

$$\mathrm{cov}(\epsilon_{ij}, \epsilon_{kl}) = [\sigma_{ij}]^2\delta_{ik}\delta_{jl}, \tag{E.7}$$

with no summation over repeated indices. Hence the full set of covariances of ϵ^{-1} is given by

$$\mathrm{cov}(\epsilon^{-1}_{\alpha\beta}, \epsilon^{-1}_{ab}) = \left([\epsilon^{-1}_{\alpha i}][\epsilon^{-1}_{ai}]\right)[\sigma_{ij}]^2\left([\epsilon^{-1}_{j\beta}][\epsilon^{-1}_{jb}]\right) , \tag{E.8}$$

where there is no sum over repeated indices inside the parenthesis. Consequently, the variance of an element of the inverse efficiency matrix is written as

$$[\sigma_{\alpha\beta}]^2 \equiv \mathrm{cov}(\epsilon_{\alpha\beta}^{-1}, \epsilon_{ab}^{-1}) = [\epsilon_{\alpha i}^{-1}]^2 [\sigma_{ij}]^2 [\epsilon_{j\beta}^{-1}]^2. \tag{E.9}$$

Equation E.9 gives the expression for the uncertainty on element ϵ_{ij}^{-1} in terms of the elements of the inverse matrix $[\epsilon]^{-1}$ and the original uncertainties of the matrix $[\epsilon]$. Note that each term of equation E.9 is squared before making the sum whereas in equation E.5 the sum is done first.

Bibliography

[1] M. Perl *et al.*, Phys. Lett., **B63** (1976) 466;
G. J. Feldman *et al.*, Phys. Rev. Lett., **B38** (1977) 117 and 576.

[2] S.L. Glashow, Nucl. Phys. **22** (1961) 579;
S. Weinberg, Phys. Rev. Lett. **19** (1967) 1264;
A. Salam, *Elementary Particle Theory* Ed. N. Svartholm, (Almquist and Wilsells, Stockholm, 1968) 357.

[3] C. Caso *et al.*, *Review of Particle Properties*, Eur. Phys. J. **C3** (1998) 1.

[4] D. Griffiths, *Introduction to Elementary Particles*, Wiley, (1987) Section 10.7.

[5] N. Cabibbo, Phys. Rev. Lett **10** (1963) 531.

[6] G.D. Rochester and C.C. Butler, Nature **160** (1947) 855.

[7] K. Lande *et. al.*, Phys. Rev. **103** (1956) 1901.

[8] C.F. Powell, P.H. Fowler and D.H. Perkins, Rep. Prog. Phys. **13** (1950) 384.

[9] S.L. Glashow, J. Iliopoulus and L. Maiani, Phys. Rev. **D2** (1970) 1585.

[10] M. Kobayashi and T. Maskawa, Prog. Theor. Phys. **49** (1973) 652.

[11] W. Heisenberg, Z. Phys. **77** (1932) 1;
Translation: D.M. Brink, *Nuclear Forces*, Pergamon Press Ltd. (1965) 144.

[12] F. Halzen and A.D. Martin, *Quarks and Leptons*, Wiley (1984) Section 14.2.

[13] M. Finkemeier and E. Mirkes, Z. Phys. **C69** (1996) 243.

[14] E. Braaten, R.J. Oakes and S. Tse, Int. J. Mod. Phys. **A5** (1990) 2737.

[15] Y.S. Tsai, Phys. Rev. **D4** (1971) 2821;
Phys. Rev. **D13** (1976) 771.

[16] S. Oneda, Phys. Rev. **D35** (1987) 397;
S. Matsuda and S. Oneda, Phys. Rev. **171** (1968) 1744.

[17] T. Das, V.S. Mathur and S. Okubo, Phys. Rev. Lett. **18** (1967) 761;
T. Das, V.S. Mathur and S. Okubo, Phys. Rev. Lett. **19** (1967) 859.

[18] LEP Design Report, CERN-LEP/TH/83-29 (1983).

[19] G. Arnison *et. al.*, Phys. Lett. **B122** (1983) 103;
M. Banner *et. al.*, Phys. Lett. **B122** (1983) 476.

[20] G. Arnison *et. al.*, Phys. Lett. **B126** (1983) 398;
P. Bagnaia *et. al.*, Phys. Lett. **B129** (1983) 130.

[21] The OPAL Collaboration, Nucl. Inst. and Meth. **A305** (1991) 275.

[22] O. Biebel *et. al.*, Nucl. Inst. and Meth. **A323** (1992) 169.

[23] SF57 lead glass from Schott Glaswerke, Germany. Properties: 75% by weight PbO, density 5.5 g/cm^3, $X_0 = 1.50$ cm and refractive index 1.8467 at 586 nm.

[24] S. Kluth and D.R. Ward, *A Study of the Performance of the OPAL Electromagnetic Calorimeter using* $\mathrm{e}^+\mathrm{e}^-\gamma$ *Events*, OPAL **TN108** (1992).

[25] D.C. Imrie *et. al.*, Nucl. Inst. and Meth. **A283** (1989) 515.

[26] The OPAL Si-W Group, B.E. Anderson, *et. al.*, IEEE Trans. Nucl. Sci. **41** (1994) 845.

[27] M.S. Livingston and H.A. Bethe, Rev. Mod. Phys. **9** (1937) 285.

[28] B. Rossi, *High Energy Particles*, Prentice Hall (1964).

[29] A.H. Walenta, Phys. Scr. **23** (1981) 354.

[30] J.S. Milton and J.C. Arnold, *Introduction to Probability and Statistics, Second Edition*, McGraw-Hill Publishing Company (1990).

[31] U. Almaldi, Phys. Scr. **23** (1981) 409.

[32] T. Ferbel, Experimental Techniques in High Energy Physics, Addison-Wesley Publishing Company, (1987).

[33] R. Wigmans, Nucl. Inst. and Meth. **A259** (1987) 389;
R. Wigmans, Nucl. Inst. and Meth. **A265** (1988) 273.

[34] R. Fernow, *Introduction to Experimental Particle Physics*, Cambridge University Press (1986).

[35] D. Lellouch, S. Weisz, *ROPE User's Guide*, OPAL-Offline note 16/OFFL-0487.

[36] S. Jadach, B.F.L. Ward and Z. Was, Comp. Phys. Comm. **66** (1991) 276.

[37] S. Jadach, J.H. Kühn and Z. Was, Comp. Phys. Comm. **64** (1991) 275.

[38] J. Allison *et. al.*, Nucl. Inst. and Meth. **A317** (1992) 47.

[39] R. Brun, F. Bruyant, M. Maise, A.C. M^{c}Pherson and P. Zanorini, GEANT3, CERN-DD/EE/84-1 (1987).

[40] F.A. Berends, R. Kleiss and W. Hollik, Nucl. Phys. **B304** (1988) 712.

[41] S. Jadach, W. Placzek and B.F.L. Ward, Phys. Lett. **B390** (1997) 298.

[42] T. Sjostrand, Comp. Phys. Comm. **82** (1994) 74.

[43] R. Bhattacharya, J. Smith and G. Grammer, Phys. Rev. **D15** (1977) 3267;
J. Smith, J.A.M. Vermaseren and G. Grammer, Phys. Rev. **D15** (1977) 3280.

[44] OPAL Collaboration, G. Abbiendi *et al.*, *A Study of Three Prong Tau Decays With Charged Kaons*, CERN-EP/99-095.

[45] ALEPH Collaboration, R. Barate *et. al.*, *One Prong Tau Decays With Kaons*, CERN-EP/99-025.

[46] S. Towers, *Monte Carlo Generation of Tau Decay Final States with Charged and Neutral Kaons*, OPAL **TN613** (1999).

[47] OPAL Collaboration, G. Alexander *et. al.*, Phys. Lett. **B266** (1991) 201.

[48] OPAL Collaboration, P. Acton *et. al.*, Phys. Lett. **B288** (1992) 373.

[49] OPAL Collaboration, G. Alexander *et. al.*, Phys. Lett. **B369** (1996) 163;
OPAL Collaboration, K. Ackerstaff *et. al.*, Eur. Phys. J. **C4** (1998) 193.

[50] OPAL Collaboration, R. Akers *et. al.*, Phys. Lett. **B339** (1994) 278.

[51] C. Peterson, T. Rognvaldsson and L. Lonnblad, Comp. Phys. Comm. **81** (1994) 185.

[52] M.S. Srivastava and E.M. Carter, *Applied Multivariate Statistics*, Elsevier Science Publishing Company, (1983).

[53] OPAL Collaboration, K. Ackerstaff *et al.*, Eur. Phys. J. **C8** (1999) 3.

[54] ALEPH Collaboration, R. Barate *et al.*, Eur. Phys. J. **C11** (1999) 599.

[55] R. Sobie and I. Lawson, *Neutral kaon production in tau decays II. Decays involving* K^0_S *mesons*, OPAL **TN601** (1999).

[56] ALEPH collaboration, R. Barate *et al.*, Eur. Phys. J., **C4** (1998) 29.

[57] CLEO Collaboration, T.E. Coan *et al.*, Phys. Rev. **D53** (1996) 6037.

[58] OPAL Collaboration, G. Abbiendi *et al.*, *Tau Decays With Neutral Kaons*, CERN-EP/99-154.

[59] L3 Collaboration, M. Acciarri *et al.*, Phys. Lett. **B352** (1995) 487.

[60] M. Finkemeier, J.H. Kühn and E. Mirkes, Nucl. Phys. Proc. Sup. **C55** (1997) 169.

[61] S. Narison and A. Pich, Phys. Lett. **B304** (1993) 359.

[62] S.I. Eidelman and V.N. Ivanchenko Nucl. Phys. Proc. Sup. **B40** (1995) 131.

[63] OPAL Collaboration, R. Akers *et al.*, Phys. Lett. **B328** (1994) 207.

[64] J. Proriol, Nucl. Inst. Meth. **A361** (1995) 581;
B. Brandl *et al.*, Nucl. Inst. Meth. **A324** (1993) 307.

[65] M. Lefebvre, R.K. Keeler, R. Sobie and J. White, *Propagation of Errors for Matrix Inversion*, hep-ex/9909031.